

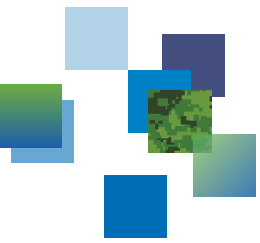


Defence Research and
Development Canada

Recherche et développement
pour la défense Canada

CAN UNCLASSIFIED

DRDC | RDDC
technology science technologie



Super Resolution Synthetic Aperture Radar

Design and Signal Processing of a Multi-Beam Multi-Channel Stripmap Mode

I.C. Sikaneta
International Atomic Energy Agency - Vienna
C.H. Gierull
DRDC – Ottawa Research Centre

Terms of Release: This document is approved for release to Defence departments and their contractors. Further distribution of this document or information contained herein is prohibited without the written approval of Defence Research and Development Canada (DRDC).

The body of this CAN UNCLASSIFIED document does not contain the required security banners according to DND security standards. However, it must be treated as CAN UNCLASSIFIED and protected appropriately based on the terms and conditions specified on the covering page.

Defence Research and Development Canada Scientific Report

DRDC-RDDC-2022-R—Will be inserted by Publication Officer
March 2022

CAN UNCLASSIFIED

Canada

CAN UNCLASSIFIED

IMPORTANT INFORMATIVE STATEMENTS

This document was reviewed for Controlled Goods by DRDC using the Schedule to the *Defence Production Act*.

Disclaimer: This publication was prepared by Defence Research and Development Canada an agency of the Department of National Defence. The information contained in this publication has been derived and determined through best practice and adherence to the highest standards of responsible conduct of scientific research. This information is intended for the use of the Department of National Defence, the Canadian Armed Forces ("Canada") and Public Safety partners and, as permitted, may be shared with academia, industry, Canada's allies, and the public ("Third Parties"). Any use by, or any reliance on or decisions made based on this publication by Third Parties, are done at their own risk and responsibility. Canada does not assume any liability for any damages or losses which may arise from any use of, or reliance on, the publication.

Endorsement statement: This publication has been peer-reviewed and published by the Editorial Office of Defence Research and Development Canada, an agency of the Department of National Defence of Canada. Inquiries can be sent to:
Publications.DRDC-RDDC@drdc-rddc.gc.ca.

© Her Majesty the Queen in Right of Canada, Department of National Defence, 2022
© Sa Majesté la Reine en droit du Canada, Ministère de la Défense nationale, 2022

CAN UNCLASSIFIED

Abstract

By presenting the design, configuration and required end-to-end signal processing, this report proposes a system for improved Synthetic Aperture Radar (SAR) imaging. Compared to conventional Spotlight SAR, the proposed system will generate imagery with equivalent or better resolution and significantly increased area coverage. The design and configuration are based upon a phased-array antenna in combination with the appropriate hardware to enable rapid electronic beam steering and to permit digitisation of multiple receive channels. The current state of technology is mature enough to construct all components of such a system. As a specific goal, the report proposes a system capable of imaging with 10 cm resolution (azimuth and slant-range) over a ground swath of 5 km. The proposed system is simulated at X-band, but could, in principle, be operated at any band with sufficiently available bandwidth. Importantly, this mode can collect with unlimited azimuth extent, something that no other proposed system can achieve.

As the considered resolutions push the limits of known theory, the report also introduces an augmented theory that is needed to derive the signal processing algorithms. The presented approach incorporates a physical model, based upon the spherical harmonic model of the Earth's gravitational potential, into the theory of differential geometry of curves in three dimensions. From the theory, a wavenumber-based SAR processing algorithm that extends current methods is developed and presented. The proposed algorithm relies only on accurate attitude data and a single accurate state vector. The approach is therefore suitable for on-board SAR processing if sensor instruments can measure these parameters while imaging.

Significance for defence and security

The material presented in this report provides the design and signal-processing framework for a SAR that can image with extremely high resolutions over wide areas. This capability does not exist for current systems, nor will it be possible with future systems, as currently planned. On the one hand, the novel proposed design offers improved SAR imaging without giving up any of the capabilities currently offered by national assets. On the other hand, the improvements meet or exceed current capability gaps in C4ISR requirements. The design (or some variant thereof) should be considered for future SAR missions.

Résumé

Ceci est le résumé en français.

Importance pour la défense et la sécurité

Ceci est l'importance pour la défense et la sécurité.

Table of contents

Abstract	i
Significance for defence and security	i
Résumé	ii
Importance pour la défense et la sécurité	ii
Table of contents	iii
List of figures	vi
List of tables	viii
Acknowledgements	ix
1 Proposal for very high resolution SAR	1
1.1 Positive aspects of the proposed approach	1
1.2 Negative aspects of the proposed approach	3
2 Notation	4
3 Multi-channel design and configuration	5
3.1 System design size	5
3.2 Traditional HRWS configuration and design	7
4 Transmit antenna	8
5 A closer look at SAR from an orbiting satellite	9
5.1 A closer examination of locally circular orbits	9
5.2 Non-linearity between arclength and time	13
5.3 Arclength parameterization approach	15
6 Differential geometry of curves in 3D	16
6.1 Calculation of differential geometry parameters from position, velocity and acceleration	18

6.2	Slow-time curve parameters, state vectors and the geoid model	19
6.2.1	State vectors	19
6.2.2	Geopotential model	19
6.3	Demonstration of accuracy of the model	20
7	Arclength-parameterized range function	29
7.1	Residual error in the range function	30
8	The SAR signal in arclength space	30
8.1	Scene measurement through multiple antenna patterns	31
8.2	Demodulation	33
8.3	Stationary phase approximation	34
9	Stationary phase	34
9.1	Relation between arclength and wavenumber	36
9.2	Antenna pattern angles	37
9.3	The 2-D wavenumber signal	38
9.4	Modified Stoltz interpolation	39
10	Multichannel signal processing for high resolution	40
11	Multi-channel SAR processing	41
11.1	Linear filtering to extract signal components	41
11.2	Matrix-vector model for the aliased signal	41
11.3	A cost function for HRWS processing	42
11.3.1	Amplified additive noise	43
11.3.2	Blended cost function	43
11.4	Section summary	43

12 Simulated multi-channel signal	44
12.1 Generation of the raw signals	44
12.2 Multi-channel processing	47
12.3 Azimuth compression	49
12.3.1 Residual phase correction	51
12.3.2 Signal-to-noise ratio	52
13 Conclusion	56
References	57
Annex A: Derivative of unit vectors	61
Annex B: ECEF acceleration	62
B.1 ECEF equations of motion	63
B.2 Rate of change of acceleration	64
Annex C: Derivation of the arclength-parameterized range function	66
Annex D: Iteration to the stationary point	68
Annex E: Numerical implementation of the Stolz interpolation	70
E.1 Simplification for iterative root-finding	70
Annex F: MIMO configuration	72
Annex G: Antenna pattern angles	75

List of figures

Figure 1:	Five channel schematic for design. Circles denote the phase-centre location while the angle denotes the direction of the transmit and receive beams.	6
Figure 2:	Antenna Lengths to achieve desired resolution for an example 11 channel system for a desired resolution of δ_0	7
Figure 3:	Equivalent HRWS system.	8
Figure 4:	Non-constant satellite radius in the ECEF coordinate system. Data extracted from Sentinel-1 Precise Orbit Ephemerides.	10
Figure 5:	Non-constant satellite velocity in the ECEF coordinate system. Data extracted from Sentinel-1 Precise Orbit Ephemerides.	12
Figure 6:	Deviation of arclength from uniform samples in meters as a function of slow-time: $s(N\Delta t) - Ns(\Delta t)$. Data extracted from Sentinel-1 Precise Orbit Ephemerides.	14
Figure 7:	Illustration of differential geometry vectors	16
Figure 8:	Comparison of numerical integration of the differential equation of satellite motion with recorded precise state vectors sourced from [1]	21
Figure 9:	Locations of Sentinel-1 and Terrasar-X satellites at the times that the geometric model is evaluated. The satellite positions were sourced from [1] and [2] for Sentinel and Terrasar-X respectivaelly. Image basemap © https://www.openstreetmap.org	22
Figure 10:	Terrasar-X 29: Argentina, descending	23
Figure 11:	Terrasar-X 706: Ukraine, ascending	23
Figure 12:	Terrasar-X 1266: Mid-Atlantic, ascending	24
Figure 13:	Terrasar-X 677: Tanzania, ascending	24
Figure 14:	Terrasar-X 1650: United States, ascending	25
Figure 15:	Sentinel-1 4591: Canada, descending	26
Figure 16:	Sentinel-1 1727: Zambia, descending	26
Figure 17:	Sentinel-1 4418: India, ascending	27

Figure 18: Sentinel-1 5650: Russia, ascending	27
Figure 19: Sentinel-1 3725: Australia, ascending	28
Figure 20: Simulation of the SURE signal.	45
Figure 21: Schematic of 5 subapertures for the 40 cm mode.	46
Figure 22: Reconstructed signals in azimuth wavenumber domain.	48
Figure 23: Processed signal Point Spread Response.	50
Figure 24: Azimuth cross-section of 10cm mode without residual phase correction.	51
Figure 25: Point Spread Function of 10cm mode after phase compensation.	52
Figure 26: Azimuth cross-section of 10cm mode after residual phase correction.	53
Figure 27: Azimuth cross-section of 10cm mode after residual phase correction.	54
Figure D.1: Simple iterative procedure showing convergence to the stationary point	68
Figure F.1: Configuration of transmit and receive. Each transmitted signal is received by all receivers	72

List of tables

Table 1:	Ground swath width, azimuth resolution and their ratio	1
Table 2:	Notation for the scalar signal in various domains. The subscript denotes the n^{th} channel.	4
Table 3:	System parameters for $\delta_0 = 0.1\text{m}$ and $v_s = 7500\text{m/s}$	8
Table 4:	Simulation parameters	44
Table 5:	Computed NESZ	55

Acknowledgements

The authors would like to thank the Technical University of Vienna for granting permission to use the Vienna Super Computing (VSC) cluster. Without this resource, the simulations could not have been pushed to the limit of 10 cm resolution.

1 Proposal for very high resolution SAR

This document proposes a system for improved space-based SAR imaging. It describes the design¹, which is based upon a phased-array and an appropriate switching network, the configuration², which imposes a rapid electronic beam switching capability upon the design, and the required signal processing algorithm to compute the high-resolution imagery.

As the authors do not have access to any operational systems to implement the approach, an end-to-end simulation, that uses a realistic collection scenario, is used to validate the system performance. The python-based simulation generates a 10cm resolution mode at X-band.

1.1 Positive aspects of the proposed approach

The proposed configuration permits measurement of very high resolution SAR in a stripmap-like mode, thereby offering, theoretically, unlimited azimuth extent.

The proposed approach significantly increases the area coverage (both in swath and azimuth extent) for the highest resolution imagery sensors on the commercial market while at the same time offering equivalent or better azimuth resolution. Table 1 highlights the added value of the approach by comparing the swath width to azimuth resolution ratio for several active commercial SAR missions [3, 4, 5, 6]. To summarise, the potential ratio of swath-width to azimuth resolution is, approximately, an order of magnitude better. In addition,

Table 1: Ground swath width, azimuth resolution and their ratio

	Azimuth resolution (m)	Swath width (km)	Ratio
RADARSAT-2	0.8	20	25
TerraSAR-X	0.25	4	16
COSMO SkyMed	0.3	7	23
ICEYE	0.25	5	20
Capella	0.5	5	10
Proposed	0.1	5	50

the strip-like nature of the proposed configuration allows imaging over an unlimited along-track (azimuth) extent. For most commercial SAR missions the Spotlight imagery footprint in ground-range and azimuth is approximately square [6].

In addition to describing the system and configuration for data collection, this document goes into the details of how to process the data to obtain a high resolution image. The signal

¹ Herein, the design is the phased array, including its dimension and element spacing, the required switching/routing circuits, the required digitizers, and the required hardware to permit changing the transmit and receive beam table on a pulse by pulse basis.

² The configuration is the way in which the system is operated and includes the pulse-repetition frequency and the transmit/receive beam tables at each pulse.

processing is split into two components that both depend on the system configuration and the imaging geometry. These components include the task of how to multi-channel process the data to obtain a single *as if collected by a traditional single channel SAR signal*, and the task of how to process this single channel signal to obtain a high resolution image. The challenge of processing high-resolution SAR imagery has been studied in the literature, [7, 8, 9, 10, 11, 12] where high-order polynomial approximations are implemented. In contrast to [12, 11, 10, 7], this document presents an arbitrarily precise method to compute the stationary point for a range history described by the square-root of a fourth-order polynomial (and shows why such a fourth-order polynomial is sufficient), and generalises the Stolt interpolation to use the approach accordingly. We also note that back-projection is a viable solution, [13], and further acknowledge the motion compensation approach of [14]. It is felt that although motion compensation is a viable approach for the high-resolution mode of TerraSAR-X, a more precise method may be needed for resolutions in the 10cm range.

Both multi-channel processing and SAR processing depend on both the system configuration and the geometry, and as one enters the realm of high-resolution, an accurate description of the geometry becomes critical, [7, 8, 9, 14, 10, 11]. It is well-known that the path of a satellite can be accurately propagated from a given state vector through numerical integration of the equations of motion. These equations depend upon an accurate model of the gravitational potential (such as from the EGM96 or EGM2008 spherical harmonic model). The numerically integrated satellite positions can be directly incorporated into back-projection SAR processing.

The algorithm presented in this document incorporates all physical effects that influence the satellite position into a wavenumber processing algorithm. We select a wavenumber processing algorithm not only to accommodate a wideband model, but also to improve processing speed when compared with back-projection. The only dynamic data required is a single accurate state-vector.

The state-vector is used to derive a satellite position model that is sufficiently accurate for an X-band SAR over a period of up to 20 seconds. By comparison, “vanilla” spaceborne SAR, i.e., the hypoerabolic model, supports an aperture time of 4.8 seconds while the fourth order model of [7] achieves an aperture time of 13.4 seconds. As far as the authors know, the presented approach is novel for space-based SAR imaging. In brief, the approach is based upon simple concepts from differential geometry which prove to be ideal, not only for computing the SAR signal model, but also for describing the multi-channel system. For instance, the differential geometry construct is used to show that, locally, multi-channel filters do not depend on the range. As a final note, we shall see that very high resolution spaceborne SAR demands consideration of not only the curvature and eccentricity of the orbit, but also the irregularities in trajectory caused by the uneven distribution of the planetary mass.

1.2 Negative aspects of the proposed approach

The promise of such a capability, no doubt, raises questions about what unfavourable aspects of the system are amplified. What trades need to be made to realise such a system, are they physically feasible, and are they worth the reward?

For a start, imaging a larger area while maintaining a useful Signal to Noise Ratio (SNR) requires a proportional increase in transmit/receive power. To avoid this problem, the azimuth length of the proposed antenna is on the order of 20m which is larger than most current missions (with the exception of RADARSAT-2). Also, as we shall see, the operating configuration benefits from the use of the entire receive aperture to maximise capture of scattered energy.

Second, to function as specified, the operating configuration calls for the ability to transmit different beams from pulse to pulse thus requiring a rapid electronic steering capability.

Third, the system needs a switching mechanism that distributes the receive sub-arrays to a multitude of distinct digitizers which, on the one hand increases hardware complexity and on the other hand, demands that more data is captured.

Fourth, as the desired resolution becomes smaller, the required azimuth beamwidth increases which also means the Doppler bandwidth increases. So, not only is the synthetic aperture physically longer (range times beamwidth), but it has to be sampled more frequently (higher bandwidth) to meet the Nyquist criteria; thus, as a rule of thumb, the required number of samples to cover the Synthetic Aperture in azimuth grows as $1/\delta_0^2$, where δ_0 is the desired azimuth resolution. As an example, while the synthetic aperture of a 3m mode on RADARSAT-2 might require 2,000 azimuth samples, equivalent 1m and 0.1m modes would require 18,000 and 1,800,000 samples respectively. To make this even more challenging, depending on the used pulse waveform and on-board processing, a similar constraint would also apply in the range direction. These data need to find a path to the ground either through a direct link with increased bandwidth if limited by the overpass time, or by a mechanism that transmits less data over a longer period of time (i.e. through a network of communications satellites).

Finally, the transformation of these more complex data into final image products requires the development and implementation of more complex signal-processing algorithms. As shall be explained, the demand for a precise geometrical description of the orbit over a long synthetic aperture, introduces several new complications to traditional SAR processing.

The next section introduces the operating configuration under ideal conditions to aid in conveying the operating concept. The combination of this operating configuration with a desired azimuth resolution dictates the design parameters and defines the minimum Pulse Repetition Frequency (PRF) through which the maximum swath is determined.

2 Notation

This document describes the SAR collection geometry with two primary variables: these are the range, r , which represents the across-track or fast-time dimension ($\tau = 2r/c$, where c is the speed of light) and s which defines arclength in the along-track dimension. The choice arclength, s , instead of the traditional slow-time variable, t will be explained in the section describing the satellite geometry model. Moreover a transformation from $s \rightarrow t$ will be derived. Even though the arclength has been adopted as the along-track parameter, in various places in the document, the PRF is still used to describe the measurement system, particularly when relating the amount of time in between pulses to the achievable swath width.

We adopt a two-symbol notation for the measured scalar signal, see Table 2; the first symbol corresponds to the domain of the r variable while the second indicates the domain of the s variable. For aesthetic reasons, we represent the measured vector and matrix signals using a single symbol; vectors, with lowercase bold, $\mathbf{s}(k_r, k_s)$, and matrices, with uppercase bold, $\mathbf{S}(k_r, k_s)$. Also note that the symbol \cdot^\dagger is used to denote the Hermitian transpose which, for a real-valued vector or matrix, reduces to the regular transpose operation. The magnitude of a vector is denoted with italicised text; for instance, $|\mathbf{r}(s, \mathbf{x})| = r(s)$. The summation without specifying limits, \sum_l , denotes summation over all l from $-\infty$ to ∞ . Similarly an integration without limits indicates integration over an infinite domain.

Without loss of generality, one may consider the measured signals in the 2-D spatial frequency domain. In this domain, if one has measurements from N (possibly different) antennas, the measured signal may be represented as a vector, $\mathbf{z}(k_r, k_s)$, with each element corresponding to the measurement from each of the different antennas in the presence of additive white Gaussian noise:

$$\begin{aligned} \mathbf{z}(k_r, k_s) &= \sum_l \begin{bmatrix} \mathcal{SS}_1(k_r, k_s + lk_{s_p}) \\ \mathcal{SS}_2(k_r, k_s + lk_{s_p}) \\ \vdots \\ \mathcal{SS}_N(k_r, k_s + lk_{s_p}) \end{bmatrix} + \mathbf{n}(k_r, k_s) \\ &= \sum_l \mathbf{s}(k_r, k_s + lk_{s_p}) + \mathbf{n}(k_r, k_s) \end{aligned} \quad (1)$$

	Range	Azimuth
$ss_n(\tau, s)$	fast-time (s)	arclength (m)
$Ss_n(\omega, s)$	angular-frequency (rad/s)	arclength (m)
$\mathcal{S}s_n(k_r, s)$	wavenumber (rad/m)	arclength (m)
$\mathcal{SS}_n(k_r, k_s)$	wavenumber (rad/m)	wavenumber (rad/m)

Table 2: Notation for the scalar signal in various domains. The subscript denotes the n^{th} channel.

where $\mathbf{n}(k_r, k_s)$ is additive white noise, and k_{sp} denotes the spatial sampling frequency (samples per meter).

In the above, k_r is a wavenumber that corresponds to the fast-time or range dimension related to the frequency of the signal via $k_r = 2\omega/c$ where ω is the radial frequency (in radians per second) of the signal. Correspondingly, k_s is a wavenumber corresponding to the slow-time-related arclength parameter.

3 Multi-channel design and configuration

Instead of beam spoiling or spotlighting to increase the synthetic aperture time, [15], we propose an operating configuration that time-multiplexes a sequence of beams using an $M + 1$ multichannel design, as illustrated in Figure 1 (with a five-channel system). This design can be realised with a phased-array that has the ability to change transmit and receive beam tables on a pulse by pulse basis [16, 17]. Additionally, $M + 1$ digitizers and a switching mechanism to route and combine the measurements from each phased-array element (i.e. form subarrays) are required to realise this multichannel system. Although we shall consider a general $M + 1$ ³ channel system, we shall occasionally choose specific values of M for illustrative purposes. The proposed system is also a uniform antenna array.

As can be seen from Figure 1, if viewed vertically, at each sampling point, the system is configured to make 5 measurements with 5 different antenna patterns. If each of these antenna patterns has a beamwidth given by $\Theta_0/(M + 1)$, then at each sampling point, the system scans over a total azimuth beamwidth of Θ_0 . The reduced beamwidth at each sampling instant corresponds to a reduced required PRF for each channel according to

$$f_p \geq B_a/(M + 1), \quad (2)$$

where B_a is the azimuth bandwidth required to achieve the desired azimuth resolution.

3.1 System design size

Consider the requirement for an azimuth resolution of δ_0 . From fundamental SAR theory, for a classical stripmap mode, this corresponds to an antenna length given by [18]

$$L_0 = 2\delta_0, \quad (3)$$

which, in turn, corresponds to a required azimuth beamwidth of

$$\Theta_0 = \frac{\lambda}{2\delta_0}, \quad (4)$$

³ The reason for choosing a convention of an $M + 1$ channel system instead of an M channel system is simply so that sums can be written as \sum_0^M rather than \sum_1^M or \sum_0^{M-1} .

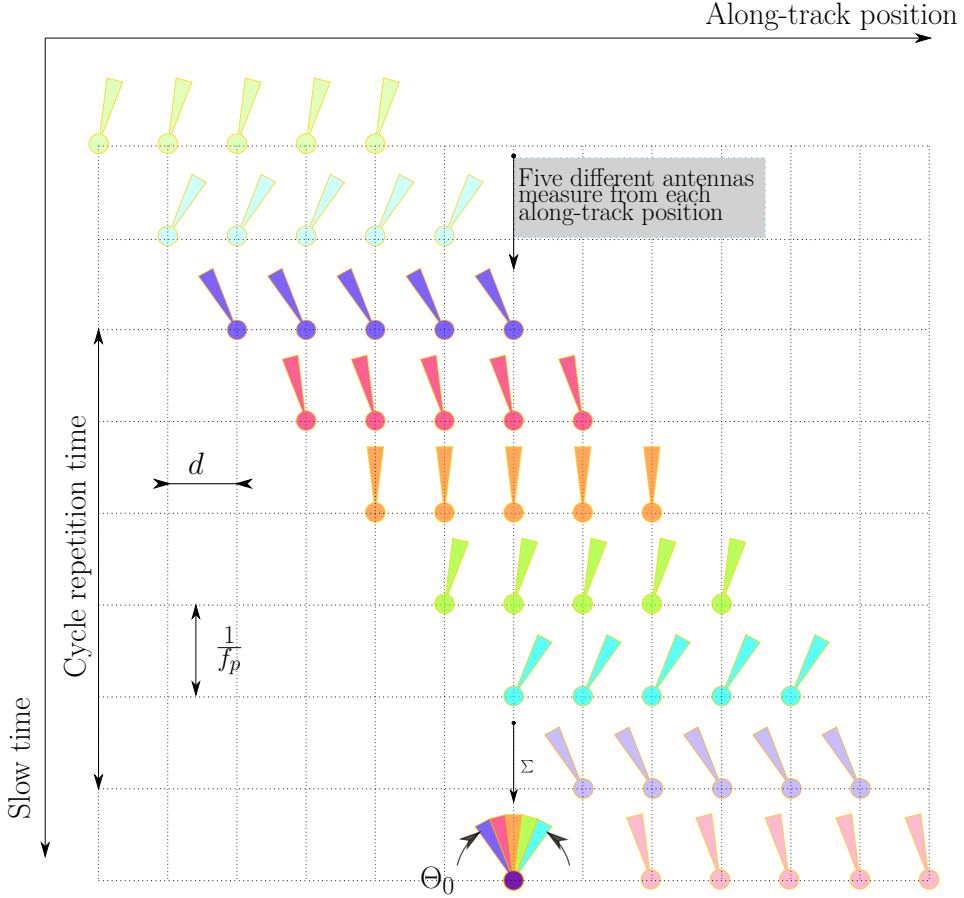


Figure 1: Five channel schematic for design. Circles denote the phase-centre location while the angle denotes the direction of the transmit and receive beams.

where λ is the narrowband carrier wavelength. If this desired beamwidth is divided into $M + 1$ parts of width

$$\Theta_M = \frac{\Theta_0}{M + 1} = \frac{\lambda}{2(M + 1)\delta_0}, \quad (5)$$

then each channel requires an antenna of length

$$L_M = 2(M + 1)\delta_0. \quad (6)$$

The required PRF is given by

$$f_p = \frac{2v_s}{\lambda} \Theta_M = \frac{2v_s}{L_M} = \frac{v_s}{(M + 1)\delta_0}, \quad (7)$$

where v_s denotes the magnitude of the satellite Earth-Centred, Earth-Fixed (ECEF) velocity. The above equates to a required two-way phase-centre separation of

$$d = (M + 1)\delta_0. \quad (8)$$

Now, with a transmit antenna of length $L_M = 2(M + 1)\delta_0$ and a receive antenna of the same length, the effective phase centre positions are given by multiples of $d = (M + 1)\delta_0$. The total antenna length, as illustrated in figure 2, will be given by

$$L = (M + 1)L_M = 2(M + 1)^2\delta_0. \quad (9)$$

Let us examine what this means for a specific case of $\delta_0 = 0.1\text{m}$. As listed in table

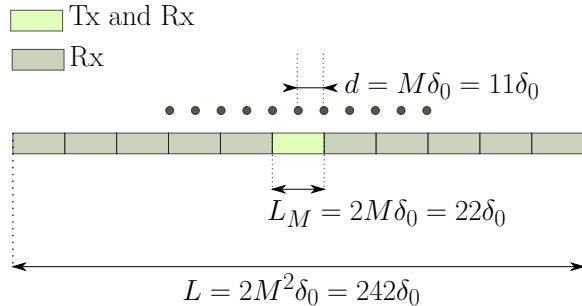


Figure 2: Antenna Lengths to achieve desired resolution for an example 11 channel system for a desired resolution of δ_0 .

3, a traditional stripmap SAR would have to be 0.2 m in azimuth length to achieve this resolution. Additionally the required PRF would be $f_p = 75\text{ KHz}$ for a satellite travelling at 7500 m/s which corresponds to a rather limited swath. On the other hand, with $M = 10$, the required PRF is $f_p = 6.818\text{ KHz}$ which corresponds to a range-swath width of approximately 22 Km (minus any time needed for chirp transmission) which would be even larger in ground range.

Please note that in this part of this document, we report the swath width as simply half the distance that light travels in the time between pulses. Section 12 provides a more realistic measure of the swath, where the pulse transmission and reception times, an azimuth oversampling factor and a 10% margin are incorporated. Specifically, for $M = 10$, for a pulse length of $50\mu\text{s}$ and an azimuth oversampling factor of 1.2 (which leads to a PRF of 8182 Hz), the slant-range swath width is reduced to 3 Km.

The choice of $\delta_0 = 0.1\text{m}$, $M = 10$ leads to an antenna of length 24.2 m with each subaperture having a length of 2.2 m. This antenna length of 24.2 m is only about 60% longer than RADARSAT-2.

3.2 Traditional HRWS configuration and design

It is a reasonable to inquire after the implication of utilising a traditional HRWS configuration that does not use a sequence of beams as proposed in this report. With this design, $M + 1$ channels transmit a wide beam that covers the desired range of angles corresponding to the desired resolution; see Figure 3. The spatial distribution of two-way phase-centres at each pulse again compensates for a lower PRF according to (7) [19].

Table 3: System parameters for $\delta_0 = 0.1\text{m}$ and $v_s = 7500\text{m/s}$.

<i>M</i>	<i>L_M</i> (m)	<i>L</i> (m)	<i>f_p</i> (Hz)	Slant Range Swath (Km)
0	0.20	0.20	75000	2.00
2	0.60	1.80	25000	6.00
4	1.00	5.00	15000	10.00
6	1.40	9.80	10710	14.00
8	1.80	16.20	8330	18.00
10	2.20	24.20	6810	22.00
12	2.60	33.80	5760	26.00
14	3.00	45.00	5000	30.00

To satisfy the spatial sampling requirement, the two-way phase-centre separation must be the same as with the proposed multi-beam design. This means that the receive antenna elements must be spaced by $2\delta_0$, giving a total receive antenna length of $2(M + 1)\delta_0$ which is $(M + 1)$ times shorter than the length proposed by the multi-beam design. This means that, on a pulse-by-pulse basis, the total receive area to capture reflected flux is reduced by a factor of $M + 1$ resulting in a corresponding loss in SNR. For this reason, the multi-beam design is recommended.

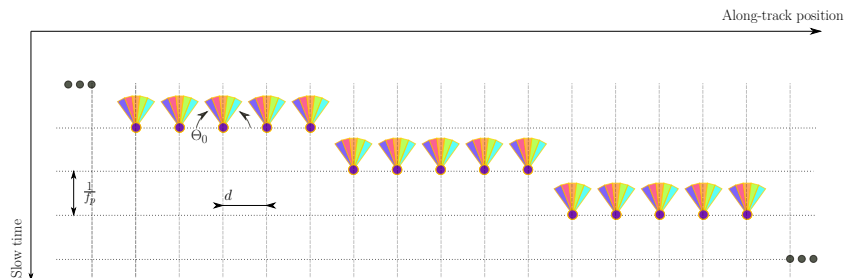


Figure 3: Equivalent HRWS system.

4 Transmit antenna

Although the proposed design consists of $M + 1$ subapertures, the requirements on the width of the transmit beam prevent transmission from the entire antenna. Transmission from the entire antenna would lead to a beam that is too narrow. Rather than route a finite power supply evenly across the entire antenna, one could instead supply the entirety of the available power only to the centre subaperture for transmission. Alternatively, one could transmit from the entire antenna, but with a spoiled pattern.

One advantage to the first approach is that only the centre subaperture requires the ability

to transmit (as illustrated in figure 2), while the other subapertures can simply be passive receivers. If the system is to be used for other purposes, then it may not be desirable to limit transmit capability only to the centre subaperture.

Note that one can easily narrow the two-way beam by transmitting from a larger number of T/R modules. This may be desirable if the user wishes for the data to be sampled above the Nyquist rate.

5 A closer look at SAR from an orbiting satellite

A review of data from currently orbiting systems shows that, when viewed from an ECEF coordinate system, Low-Earth Orbit (LEO) SAR satellites do neither travel with a constant velocity, nor do they orbit at a constant range. These satellites experience a constant or time varying jerk, not only because they follow elliptical orbits, but also because of variations in the Earth's gravitational field. As shall be demonstrated, this is true not only globally, but also locally and means that as one attempts to produce higher and higher resolution imagery, one runs into limitations in SAR signal processing algorithms based upon circular orbits. Depending on the orbit, uniform slow-time sampling does not equate to uniform spatial sampling. *This means that the actual synthetic aperture that forms a beam is derived from a set of points that are not uniformly spatially-spaced.*

Since the satellite position plays a critical role in SAR processing, compensation needs to be made for these orbital effects. Current SAR processing approaches, such as [7, 8, 9, 10, 11, 12] generate high-order (up to fourth and fifth order) polynomial approximations for the range history and use the satellite orbital history or the data themselves to estimate the coefficients of these polynomials. In contrast, reference [14] uses a motion compensation approach, based upon the satellite state vectors. This document seeks to incorporate all physical effects that influence the satellite position into a wavenumber processing algorithm. A wavenumber algorithm is adopted not only to accommodate a wideband model, but to improve processing speed when compared with back-projection.

5.1 A closer examination of locally circular orbits

Figures 4 and 5 illustrate real data extracted from precise orbit ephemerides computed for Sentinel-1, sourced from [1]. One sees that over a couple of seconds, the radius of the orbit has changed by several meters. As well, the velocity has changed by a tenth of a meter per second. These quantities are rather large when compared to the wavelength of (in this case for Sentinel-1) about 0.05 m.

For the synthetic aperture lengths employed by Sentinel-1 and most commercial systems (RADARSAT-2, RCM, Palsar), the deviations described are not critical to image formation. The non-constant nature of the target range, and of the ECEF velocity, can be hidden by algorithms that, instead of calculating from first principles, numerically estimate the required

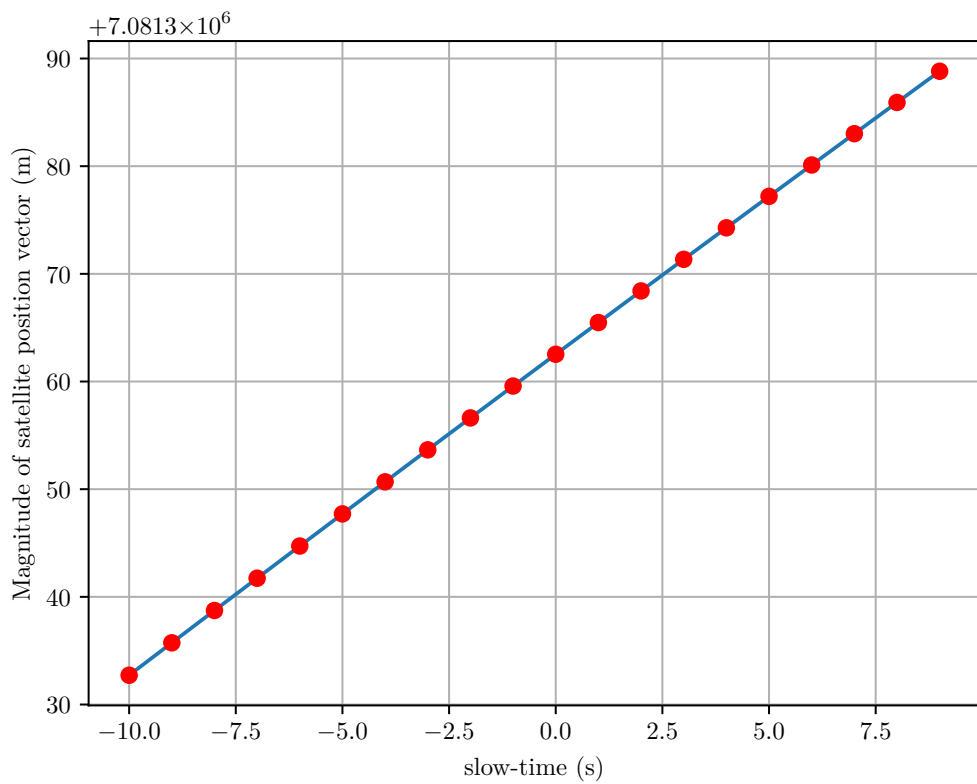


Figure 4: Non-constant satellite radius in the ECEF coordinate system. Data extracted from Sentinel-1 Precise Orbit Ephemerides.

SAR processing parameters.

This work seeks to provide first-principles-based accounting for how to compute the SAR processing parameters. Such information could help with on-board SAR processing schemes where the data required to numerically calculate the required parameters is more difficult to obtain.

The document uses the theory of the differential geometry of curves in three dimensions as a mathematical basis, and applies a physical model based upon the spherical harmonic model of the Earth's gravitational potential. Although a review of differential geometry is provided herein, a highly recommended reference can be found in [20]. Equally, a highly recommended reference for application of the spherical harmonic model to satellite motion can be found at [21].

As a final comment, note that calculations for the satellite positions have been made using the egm96 spherical harmonic expansions available at [22], through custom python code that implements the method outlined in [21].

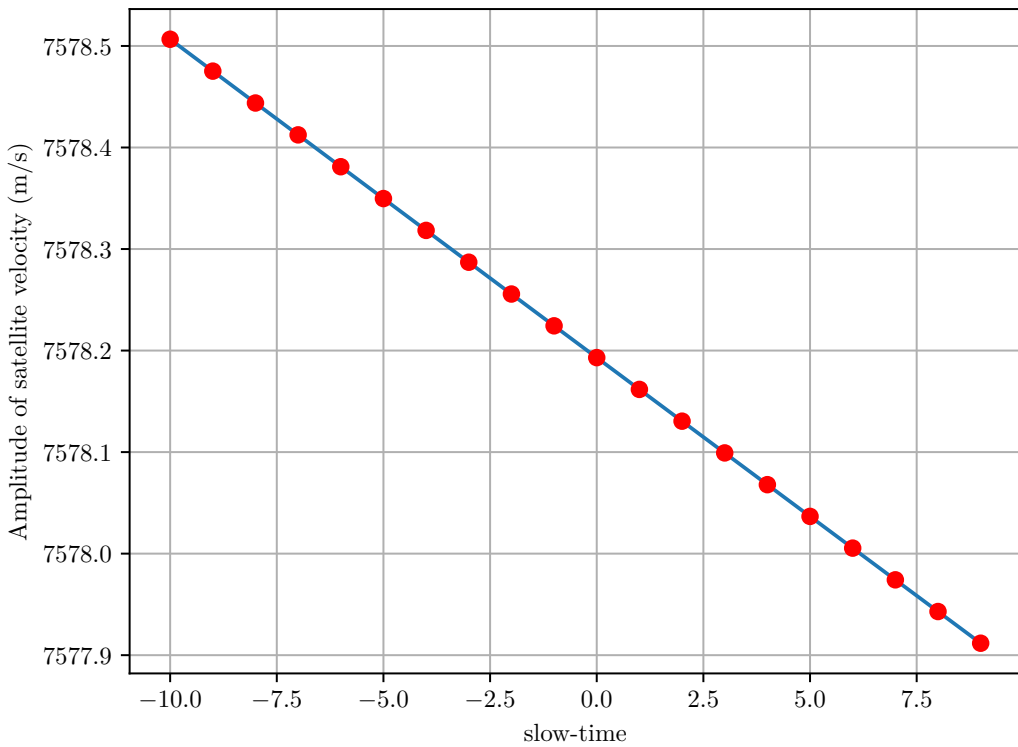


Figure 5: Non-constant satellite velocity in the ECEF coordinate system. Data extracted from Sentinel-1 Precise Orbit Ephemerides.

5.2 Non-linearity between arclength and time

The previous section presented real data showing that target range and satellite velocity do not remain constant over time. This section derives a relationship between arclength and slow-time for the purpose of demonstrating that they are, in general, not linearly related. The actual synthetic aperture that forms a beam is derived from a set of points that are not uniformly spatially-spaced.

To begin the derivation, denote the arc-length parameterized satellite position vector as $\mathbf{c}_s(s)$, where the parameter s denotes arc length. This position vector defines a curve in three dimensions. The relation between arclength and time t is defined as

$$s(t) = \int_0^t |\dot{\mathbf{c}}_t(\xi)| d\xi, \quad (10)$$

where $\mathbf{c}_t(\xi)$ denotes the slow-time parameterized satellite position vector and the dot notation, $\dot{\mathbf{c}}_t(\xi)$, indicates the derivative with respect to time. The above simply states that arc length is the integration of the amplitude of the instantaneous satellite velocity over time⁴. Rather than computing the exact integral, an expansion to third order suffices for most applications. By applying the vector calculus relations outlined in Appendix A, one finds that

$$\dot{s} = |\dot{\mathbf{c}}_t(t)| \quad (11)$$

$$\ddot{s} = \dot{\mathbf{c}}_t^\dagger(t) \dot{\mathbf{c}}_t(t) \quad (12)$$

$$\dddot{s} = \frac{\ddot{\mathbf{c}}_t^\dagger(t) \mathbf{P}_{\dot{\mathbf{c}}_t(t)} \ddot{\mathbf{c}}_t(t)}{|\dot{\mathbf{c}}_t(t)|} + \dot{\mathbf{c}}_t^\dagger(t) \ddot{\mathbf{c}}_t(t). \quad (13)$$

In the above, $\hat{\mathbf{x}}$ denotes the unit vector in the direction, \mathbf{x} and the projection operator \mathbf{P}_y applied on the vector \mathbf{x} extracts the component of \mathbf{x} that is perpendicular to the vector \mathbf{y} . The derivatives can be used to expand the expression for arclength around $t = 0$:

$$s(t) \approx \frac{t}{1!} |\dot{\mathbf{c}}_t(0)| + \frac{t^2}{2!} \dot{\mathbf{c}}_t^\dagger(0) \dot{\mathbf{c}}_t(0) + \frac{t^3}{3!} \left[\frac{\ddot{\mathbf{c}}_t^\dagger(0) \mathbf{P}_{\dot{\mathbf{c}}_t(0)} \ddot{\mathbf{c}}_t(0)}{|\dot{\mathbf{c}}_t(0)|} + \dot{\mathbf{c}}_t^\dagger(0) \ddot{\mathbf{c}}_t(0) \right]. \quad (14)$$

Disregarding the third order term in t , consideration of the above reveals that s and t are only proportional when the orbit is such that the velocity vector is perpendicular to the acceleration vector $\dot{\mathbf{c}}_t^\dagger(t) \dot{\mathbf{c}}_t(t) = 0$, which, in general, is not the case. And if time and position are not proportional, then any synthetic aperture processing algorithm derived from uniform time samples is only approximately correct because the spatial samples are non-uniform. This is akin to using a phased-array radar with non-uniformly distributed array phase-centres.

Figure 6 shows how arc length shrinks as a function of slow-time for real Sentinel-1 measurements. Specifically, for a time sampling period of Δt , the plot shows $s(N\Delta t) - Ns(\Delta t)$.

⁴ by definition, $\dot{\mathbf{c}}_t(t)$ is the satellite velocity vector, $\ddot{\mathbf{c}}_t(t)$ is the satellite acceleration vector, e.t.c.

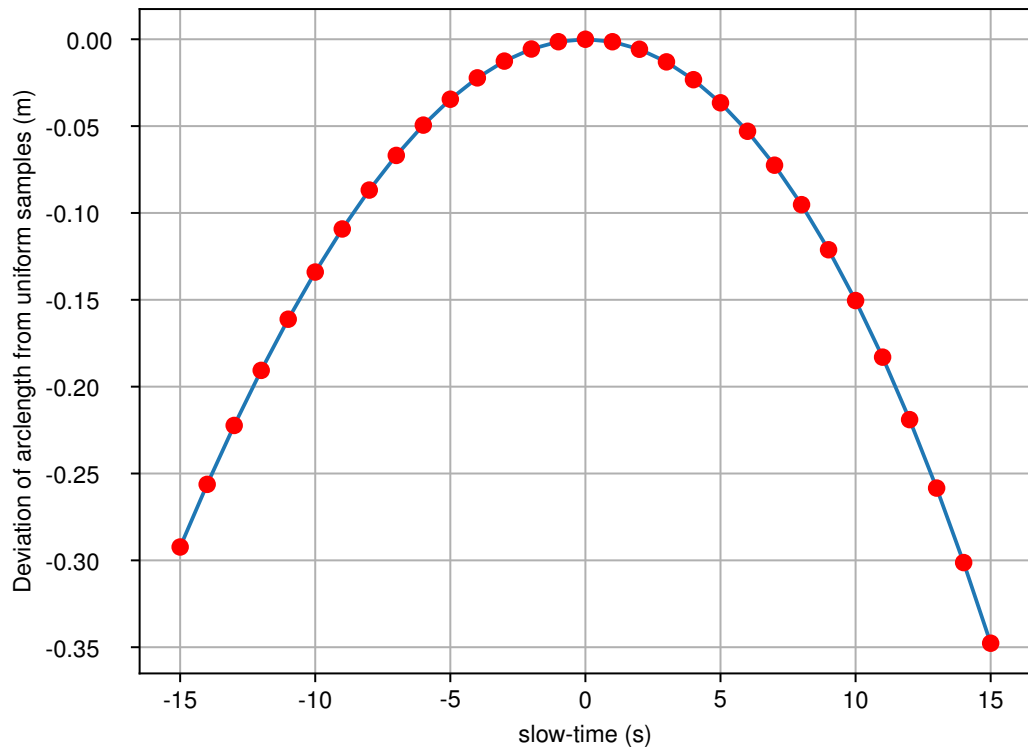


Figure 6: Deviation of arclength from uniform samples in meters as a function of slow-time: $s(N\Delta t) - Ns(\Delta t)$. Data extracted from Sentinel-1 Precise Orbit Ephemerides.

Only in the region of ± 1 second is the arclength difference small enough to be ignored (0.009 m). By the time one arrives at two seconds, the arclength is 0.03m shorter than expected from a linear realtionship between time and arclength, and in this region, one is already approaching the C- and X-band wavelengths.

From a physical point of view, this means that with a uniform PRF, spatial samples become increasingly non-uniform as the synthetic aperture length increases. This means that any definition of range as a function of slow-time needs to incorporate this non-linear effect in addition to the usual non-linear effect of the hyperbola (where a constant velocity is assumed). To achieve this, SAR processors typically fine-tune the effective velocity parameter through estimation from orbit measurements and raw data, [23, 24, 25].

5.3 Arclength parameterization approach

A potential solution, and the recommendation of this document, is to design satellite radar systems that vary their PRF in order to maintain uniform spatial sampling. This could possibly be achieved by triggering pulse transmission based upon a device that not only measures arclength through inertial measurements but also adjusts for non-inertial earth rotation effects.

Most space-based SAR literature develops the signal using fast-time, slow-time coordinates, but there are advantages to approaching the development using arclength instead of slow-time. These include a simplified (in the opinion of the authors) derivation, an approach that inherently assumes uniform spatial sampling and, perhaps most importantly, a means to apply a first-principles-based approach based upon the highly accurate gravitational model provided by the NGA/NIMA spherical harmonic libraries known as egm96 or egm2008, [22].

Section 6 provides a brief review of some elementary differential geometry concepts and shows how they relate to physical quantities associated with SAR imaging. This is followed by Section 7 which implements these concepts and derives the SAR signal as a function of range wavenumber and arclength wavenumber.

6 Differential geometry of curves in 3D

This section reviews material abundant in published literature; for instance, see [20] for a highly recommended introduction. While the material presented is complete for understanding the application to SAR imaging, it represents only a small tip of the theory and is by no means original - even common differential geometry notation has been maintained.

In this short section all the required tools to develop the SAR satellite signal model are presented.

For a curve in three dimensions given by $\mathbf{c}_s(s)$, the tangent vector is given by $\mathbf{T}(s) = \mathbf{c}'_s(s)$, where $'$ denotes derivative with respect to s . Because of the arclength parameterisation, $\mathbf{T}(s)$ is a unit vector and $\mathbf{T}(s) \cdot \mathbf{T}'(s) = 0$. The **curvature** is defined as $\kappa(s) = |\mathbf{T}'(s)|$. Define the unit vector

$$\mathbf{N}(s) = \mathbf{T}'(s)/\kappa(s). \quad (15)$$

The binormal vector $\mathbf{B}(s)$ is defined as $\mathbf{B}(s) = -\mathbf{T}(s) \times \mathbf{N}(s)$ (In order to form a right-handed coordinate system). The vectors $\mathbf{T}(s), \mathbf{N}(s), \mathbf{B}(s)$ form an orthonormal basis, see Figure 7

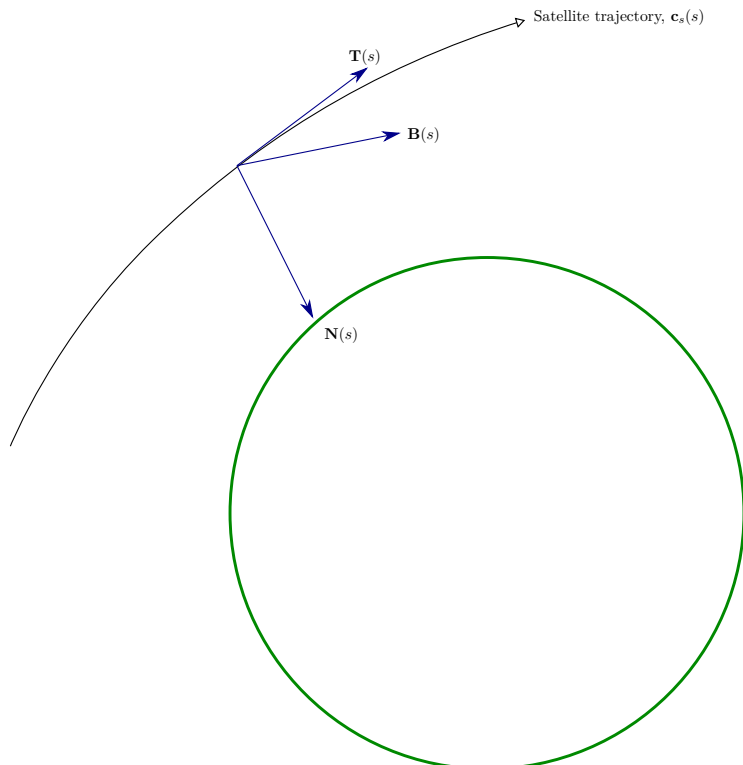


Figure 7: Illustration of differential geometry vectors

Since $\mathbf{T}(s) \cdot \mathbf{N}(s) = 0$,

$$\begin{aligned}\mathbf{T}(s) \cdot \mathbf{N}'(s) &= -\mathbf{T}'(s) \cdot \mathbf{N}(s) \\ &= -\kappa(s)\end{aligned}\tag{16}$$

Define the **torsion** as $\tau(s) = \mathbf{N}'(s) \cdot \mathbf{B}(s)$. Then, by multiplying $\mathbf{N}'(s) = a_T \mathbf{T}(s) + a_N \mathbf{N}(s) + a_B \mathbf{B}(s)$ ⁵ successively by $\mathbf{T}(s), \mathbf{N}(s), \mathbf{B}(s)$, one finds that

$$\mathbf{N}'(s) = -\kappa(s)\mathbf{T}(s) + \tau(s)\mathbf{B}(s)\tag{17}$$

Finally, one finds that

$$\begin{aligned}\mathbf{B}'(s) &= -\mathbf{T}'(s) \times \mathbf{N}(s) - \mathbf{T}(s) \times \mathbf{N}'(s) \\ &= -\kappa(s)\mathbf{N}(s) \times \mathbf{N}(s) - \mathbf{T}(s) \times [-\kappa(s)\mathbf{T}(s) + \tau(s)\mathbf{B}(s)] \\ &= -\tau(s)\mathbf{N}(s)\end{aligned}\tag{18}$$

The previous few expressions lead to the Frenet-Serret equation

$$\begin{bmatrix} \mathbf{T}'(s) \\ \mathbf{N}'(s) \\ \mathbf{B}'(s) \end{bmatrix} = \begin{bmatrix} 0 & \kappa(s) & 0 \\ -\kappa(s) & 0 & \tau(s) \\ 0 & -\tau(s) & 0 \end{bmatrix} \begin{bmatrix} \mathbf{T}(s) \\ \mathbf{N}(s) \\ \mathbf{B}(s) \end{bmatrix}.\tag{19}$$

The Frenet-Serret equation will be used in numerous places throughout this document to derive quantities related to the SAR signal model.

One observes that

$$\begin{aligned}\mathbf{c}'_s(s) &= \mathbf{T}(s) \\ \mathbf{c}''_s(s) &= \mathbf{T}'(s) = \kappa(s)\mathbf{N}(s) \\ \mathbf{c}'''_s(s) &= \kappa'(s)\mathbf{N}(s) + \kappa(s)\mathbf{N}'(s) \\ &= \kappa'(s)\mathbf{N}(s) - \kappa^2(s)\mathbf{T}(s) + \kappa(s)\tau(s)\mathbf{B}(s)\end{aligned}\tag{20}$$

Thus, a third order polynomial approximation to the satellite orbit around the point s_0 , which we denote as $\mathbf{c}_p(s)$, can be expressed as

$$\begin{aligned}\mathbf{c}_s(s) \approx \mathbf{c}_p(s) &= \mathbf{c}_s(s_0) + (s - s_0)\mathbf{T}(s_0) + \frac{(s - s_0)^2}{2!}\kappa(s_0)\mathbf{N}(s_0) \\ &\quad + \frac{(s - s_0)^3}{3!}[\kappa'(s_0)\mathbf{N}(s_0) - \kappa^2(s_0)\mathbf{T}(s_0) + \kappa(s_0)\tau(s_0)\mathbf{B}(s_0)]\end{aligned}\tag{21}$$

To make the notation more compact, we introduce $\mathbf{T}_0, \mathbf{N}_0, \mathbf{B}_0, \kappa_0, \kappa'_0, \tau_0$ as all the respective functions evaluated at some suitably chosen s_0 .

$$\begin{aligned}\mathbf{c}_p(s) &= \mathbf{c}_s(s_0) + (s - s_0)\mathbf{T}_0 + \frac{(s - s_0)^2}{2}\kappa_0\mathbf{N}_0 \\ &\quad + \frac{(s - s_0)^3}{6}[-\kappa_0^2\mathbf{T}_0 + \kappa'_0\mathbf{N}_0 + \kappa_0\tau_0\mathbf{B}_0]\end{aligned}\tag{22}$$

⁵ since $\mathbf{T}(s), \mathbf{N}(s), \mathbf{B}(s)$ form an orthonormal basis, we can write $\mathbf{N}'(s)$ as a linear combination with parameters a_T, a_N, a_B

6.1 Calculation of differential geometry parameters from position, velocity and acceleration

Computation of physical spacecraft parameters requires relating arclength to time. This section derives the relations between slow time and arclength using relations derived in Appendix A. In the text below, the satellite curve as a function of arclength, $\mathbf{c}_s(s)$, is related to the same curve as a function of slow time $\mathbf{c}_t(t)$. While $\mathbf{c}'_s(s)$ denotes the derivative of the curve with respect to arclength, $\dot{\mathbf{c}}_t(t)$ denotes the derivative of the curve with respect to slow time.

Since

$$\mathbf{T}(s) = \frac{d\mathbf{c}_s}{ds} = \frac{d\mathbf{c}_t(t)}{dt} \frac{dt}{ds} = \frac{1}{|\dot{\mathbf{c}}_t(t)|} \dot{\mathbf{c}}_t(t) = \hat{\mathbf{c}}_t(t). \quad (23)$$

In the above and in the expressions below, the equation on the left, a function of s is related to an expression on the right, a function of t , under the relation that t is a function of s , i.e. $t = t(s)$. The tangent vector, $\mathbf{T}(s)$, is just the unit velocity vector. With $k(s) = |\mathbf{T}'(s)|$, and with the aid of Appendix A, one computes

$$\frac{d\mathbf{T}(s)}{ds} = \frac{1}{|\dot{\mathbf{c}}_t(t)|} \frac{d\hat{\mathbf{c}}_t(t)}{dt} = \frac{\mathbf{P}_{\dot{\mathbf{c}}_t(t)} \ddot{\mathbf{c}}_t(t)}{|\dot{\mathbf{c}}_t(t)|^2}, \quad (24)$$

where the projection operator, which computes the component of a vector that is perpendicular to \mathbf{f} , is defined as

$$\mathbf{P}_\mathbf{f} = \mathbf{I} - \hat{\mathbf{f}}\hat{\mathbf{f}}^T. \quad (25)$$

One finds that

$$k(s) = \frac{|\mathbf{P}_{\dot{\mathbf{c}}_t(t)} \ddot{\mathbf{c}}_t(t)|}{|\dot{\mathbf{c}}_t(t)|^2}. \quad (26)$$

Recall that $\mathbf{N}(s)$ is defined as the unit vector in the direction of $\mathbf{T}'(s)$. With the previous expression, one finds that

$$\mathbf{N}(s) = \frac{\mathbf{P}_{\dot{\mathbf{c}}_t(t)} \ddot{\mathbf{c}}_t(t)}{|\mathbf{P}_{\dot{\mathbf{c}}_t(t)} \ddot{\mathbf{c}}_t(t)|} = \hat{\mathbf{w}}(t), \quad (27)$$

with $\mathbf{w}(t) = \mathbf{P}_{\dot{\mathbf{c}}_t(t)} \ddot{\mathbf{c}}_t(t)$. This means that

$$\mathbf{N}'(s) = \frac{1}{|\dot{\mathbf{c}}_t(t)|} \frac{d}{dt} \hat{\mathbf{w}}(t) = \frac{1}{|\dot{\mathbf{c}}_t(t)|} \frac{\mathbf{P}_\mathbf{w}(t) \dot{\mathbf{w}}(t)}{|\mathbf{w}(t)|}. \quad (28)$$

It is also possible to compute that

$$\begin{aligned} \dot{\mathbf{w}}(t) &= \frac{d\mathbf{P}_{\dot{\mathbf{c}}_t(t)} \ddot{\mathbf{c}}_t(t)}{dt} \\ &= -\frac{1}{|\dot{\mathbf{c}}_t(t)|} \left[\mathbf{P}_{\dot{\mathbf{c}}_t(t)} \ddot{\mathbf{c}}_t(t) \tilde{\mathbf{c}}_t^T(t) + \hat{\mathbf{c}}_t(t) \ddot{\mathbf{c}}_t^T(t) \mathbf{P}_{\dot{\mathbf{c}}_t(t)} \right] \dot{\mathbf{c}}_t(t) + \mathbf{P}_{\dot{\mathbf{c}}_t(t)} \ddot{\mathbf{c}}_t(t). \end{aligned} \quad (29)$$

Thus

$$\begin{aligned}\mathbf{N}'(s) = \frac{1}{|\dot{\mathbf{c}}_t(t)|} \frac{\mathbf{P}_{\mathbf{w}(t)}}{|\mathbf{w}(t)|} & \left[-\frac{1}{|\dot{\mathbf{c}}_t(t)|} \left[\mathbf{P}_{\dot{\mathbf{c}}_t(t)} \ddot{\mathbf{c}}_t(t) \dot{\mathbf{c}}_t^T(t) + \hat{\mathbf{c}}_t(t) \ddot{\mathbf{c}}_t^T(t) \mathbf{P}_{\dot{\mathbf{c}}_t(t)} \right] \ddot{\mathbf{c}}_t(t) \right. \\ & \left. + \mathbf{P}_{\dot{\mathbf{c}}_t(t)} \ddot{\mathbf{c}}_t(t) \right]\end{aligned}\quad (30)$$

These expressions permit calculation of the tangent, normal and binormal vectors, the curvature and the torsion.

6.2 Slow-time curve parameters, state vectors and the geoid model

Section 6.1 produced expressions that depend upon $\mathbf{c}_t(t)$, $\dot{\mathbf{c}}_t(t)$, $\ddot{\mathbf{c}}_t(t)$ and $\ddot{\mathbf{c}}_t(t)$. This section demonstrates how these quantities can be computed from state vectors and the NASA published geoid model (EGM96 or EGM2008), [22].

6.2.1 State vectors

State vectors provided by vendors often reference the ECEF coordinate system; that is, they are given in an Earth-Centred, Earth Fixed (ECEF) coordinate system. We define the position component of the state vector as $\mathbf{c}_t(t)$ while the velocity component provides $\dot{\mathbf{c}}_t(t)$.

6.2.2 Geopotential model

Calculation of $\ddot{\mathbf{c}}_t(t)$ and $\ddot{\mathbf{c}}_t(t)$ requires application of a geoid model as the acceleration at any given point depends primarily on the mass distribution of the earth. Secondary factors including drag, lunar and solar gravitation effects and tidal effects are not considered here. It is felt that these effects do not significantly perturb the satellite trajectory over the time periods of even the highest resolution synthetic apertures.

The EGM96 geopotential model provides a set of parameters to be used in a spherical harmonic expansion that approximates the earth gravitational potential, [22]. The prescription yields the gravitational potential as a function of radius, latitude, longitude, respectively, $U(r, \phi_s, \lambda_s)$.

$$\begin{aligned}U(r, \phi_s, \lambda_s) &= \frac{GM}{r} \left(1 + \sum_{n=2}^{n_{\max}} \left(\frac{a}{r} \right)^n \sum_{m=0}^n \bar{P}_{nm}(\sin \phi_s) \left[\bar{C}_{nm} \cos m\lambda_s + \bar{S}_{nm} \sin m\lambda_s \right] \right)\end{aligned}\quad (31)$$

where a is the major axis of the Earth (m), $\bar{P}_{nm}(\cdot)$ are the fully normalized associated Legendre polynomials of degree n and order m , \bar{C}_{nm} and \bar{S}_{nm} are the model coefficients (e.g. egm96, egm2008 from NIMA/NGA). Note that ϕ_s , λ_s are given in a spherical polar coordinates not the common ellipsoidal latitude and longitude as in geography.

The gravitational potential and its derivatives, given in spherical polar coordinates, are transformed into Cartesian coordinates in order to calculate the acceleration and rate of change of acceleration. Appendix B.2 outlines how this can be accomplished. A clearly written explanation on how to apply the spehircal harmonics to calculation of satellite trajectories can be found in [21]. This document calculates the satellite acceleration in the ECEF coordinate system; further, the material in Appendix B.2 also considers the rate of change of acceleration as this becomes important in the derivation of the satellite motion over long synthetic apertures.

Note that the gravitational potential is given in an inertial coordinate system. Thus, calculated accelerations must be transformed into an ECEF coordinate system. Appendix B and [21] show how this transformation can be accomplished.

Figure 8 demonstrates the accuracy of the physical geoid model using precision state vector data obtained from [1]. The plot has been generated by taking a single state vector at slow-time value zero (arbitrarily chosen to be 2018-08-05 16:08:22) and numerically integrating the position of the satellite forty seconds forwards and backwards in time. This numerical result has been computed by using the `scipy integrate.solve_ivp` method in Python3 to integrate the differential equation listed in [21]; in this case with the egm96 geoid model, but without any lunar solar or drag effects. Either side of slow-time zero, the recoded precise state vectors are compared with the numerically integrated result. One sees that, over the course of eighty seconds, the satellite position is within 5 millimeters of the reference position.

6.3 Demonstration of accuracy of the model

With the above relations, figures 10 to 19 plot satellite positions using (22) over a range of different locations for exemplary data from Sentinel-1 and Terrasar-X. Restituted orbit files from Sentinel-1, sourced from [1], and rapid science orbit files for Terrasar-X, sourced from [2] are used to generate the analysis. Each of the data files obtained from the aforementioned URLs containes several hundred satellite state vectors for the corresponding sensor and, in order to test numerical integration, as outlined in Section 6.2, a few randomly selected state vectors are examined from each file. The indices of these few state vectors are the numbers associated with each of the points illustrated in Figure 9, where the physical location of the satellite at the times of propagation are presented geographically. Satellite orbits are propagated around these selected points, both forward and backwards in time and the results are compared with neighbouring state vectors also recorded in the file. As is clearly evident in figures 10 to 19, numerical integration of the differential equations yields highly accurate, sub-millimeter, values over the period of 40 seconds⁶. The satellite position derived through numerical integration thus provides a highly accurate reference against which to test (22).

⁶ Similar propagation accuracies are obtained with the rapid science orbit files for TSX. These are not plotted because the temporal spacing between sample points is 30 seconds; thus, only the trivial source vector for propagation, which was read from the file, would be available for comparison.

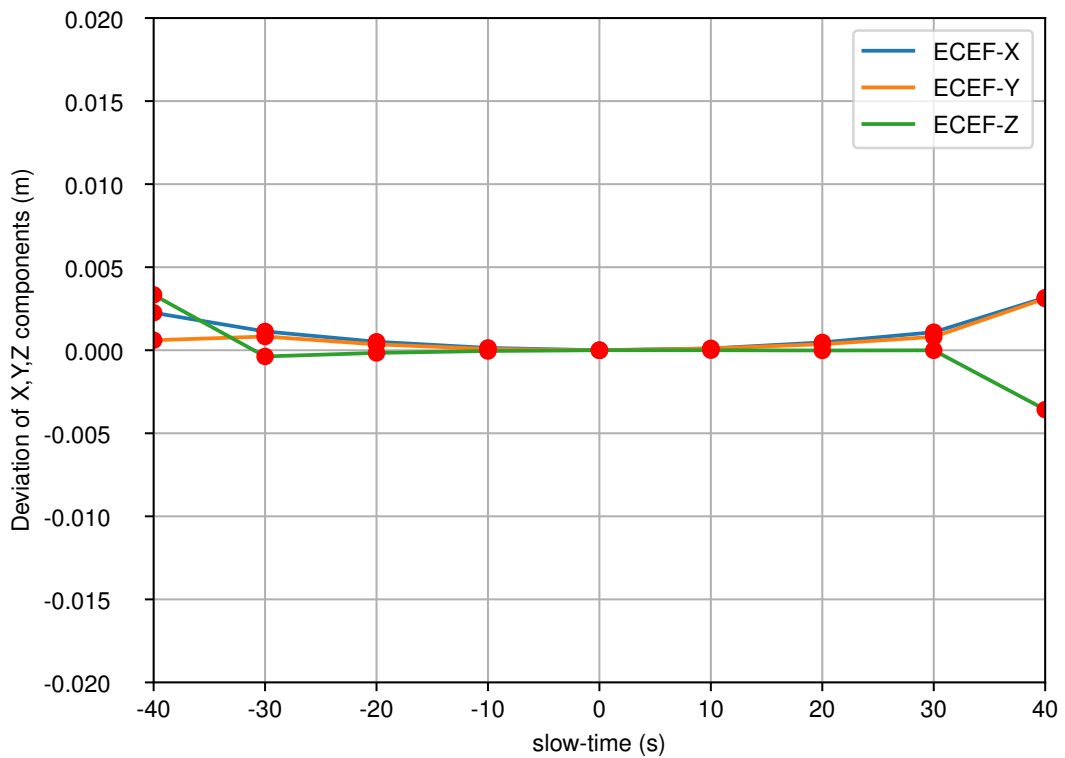


Figure 8: Comparison of numerical integration of the differential equation of satellite motion with recorded precise state vectors sourced from [1]



Figure 9: Locations of Sentinel-1 and Terrasar-X satellites at the times that the geometric model is evaluated. The satellite positions were sourced from [1] and [2] for Sentinel and Terrasar-X respectively. Image basemap
 ©<https://www.openstreetmap.org>.

The figures show that the error in using (22) depends on the spatial location of the satellite. This is a result of the uneven distribution of the mass of the earth. On average, over a period of plus/minus ten seconds, the approximation yields an accurate range history, maximum error of 5-10 mm, for a target that is in the center of a beam with a depression angle of 45 degrees.

Note that although these errors are small, they are computable and can be eliminated with appropriate processing. Given the scale of the error (for an X-band system), corrections can be made to the phase of the measured data without regard to the time delay. Section 12 illustrates the effect of these errors and shows how they can be mitigated.

Equation (22) thus provides a highly accurate and readily computable mathematical function to express the satellite position during a period of twenty seconds. Compared to the Sentinel-1 orbit, which occupies a higher altitude, the expansion for the Terrasar-X orbit maintains its accuracy for a shorter period of time.

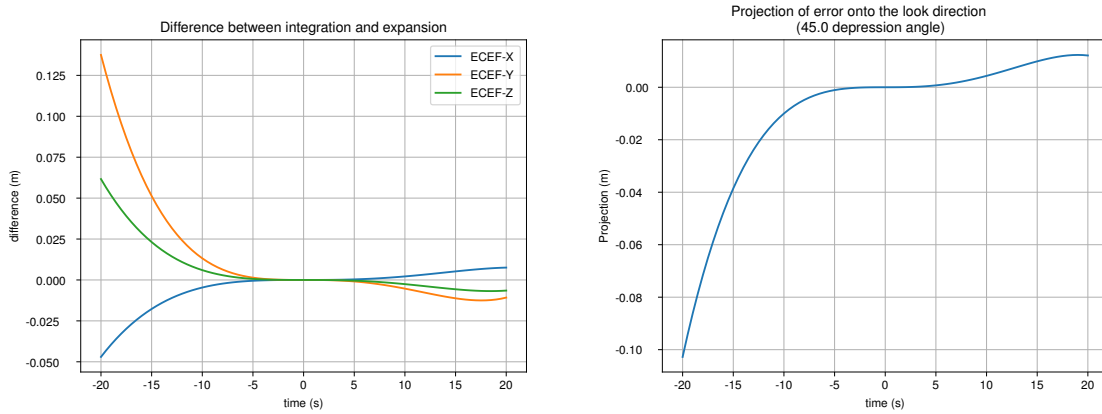


Figure 10: Terrasar-X 29: Argentina, descending

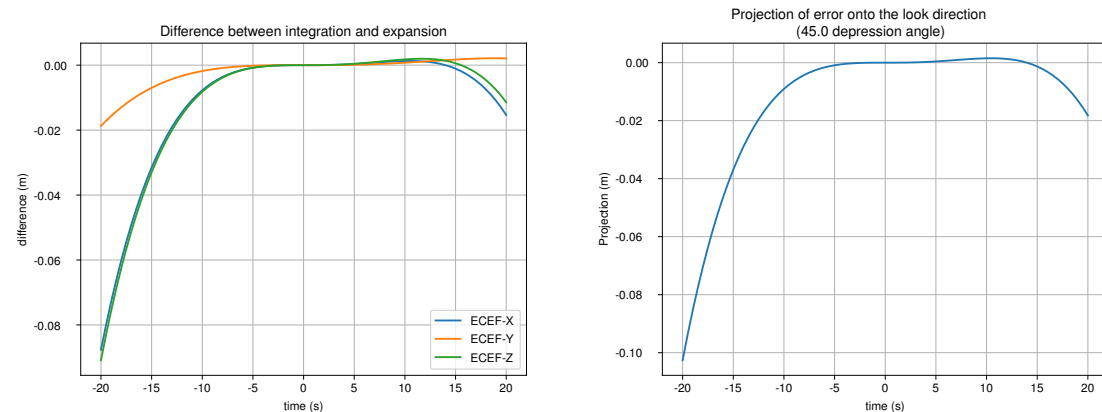


Figure 11: Terrasar-X 706: Ukraine, ascending

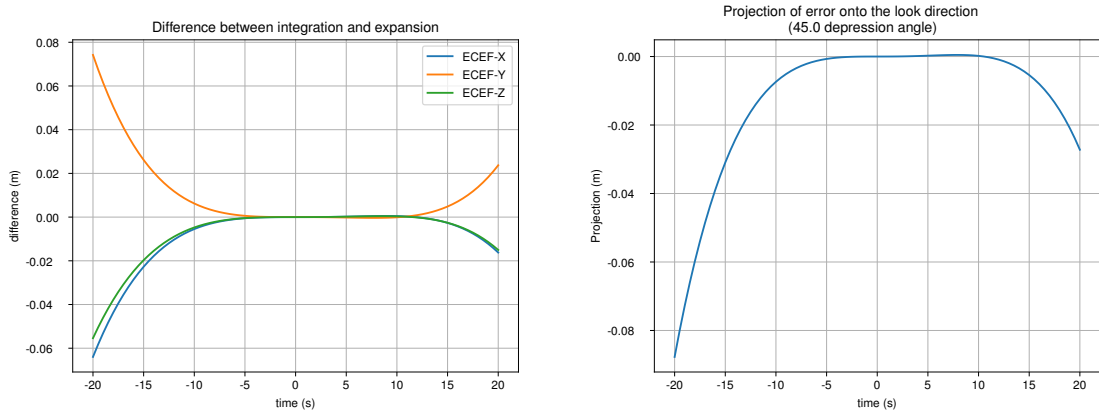


Figure 12: Terrasar-X 1266: Mid-Atlantic, ascending

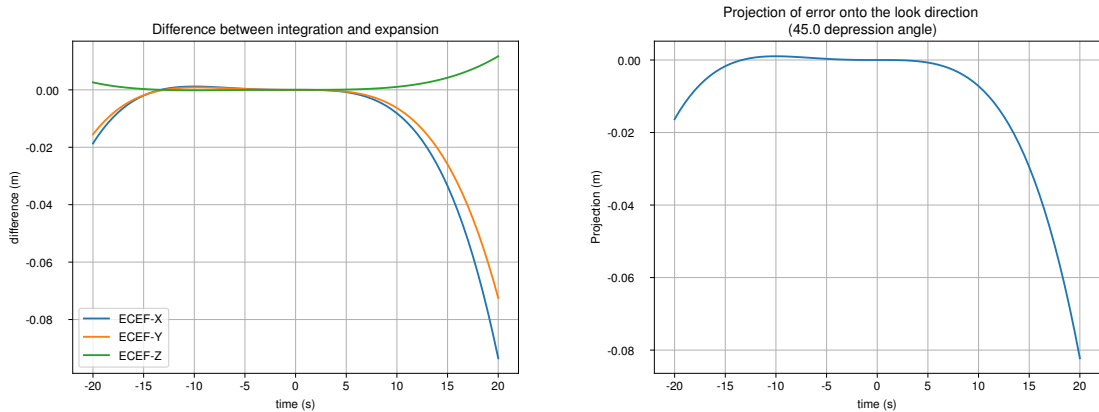


Figure 13: Terrasar-X 677: Tanzania, ascending

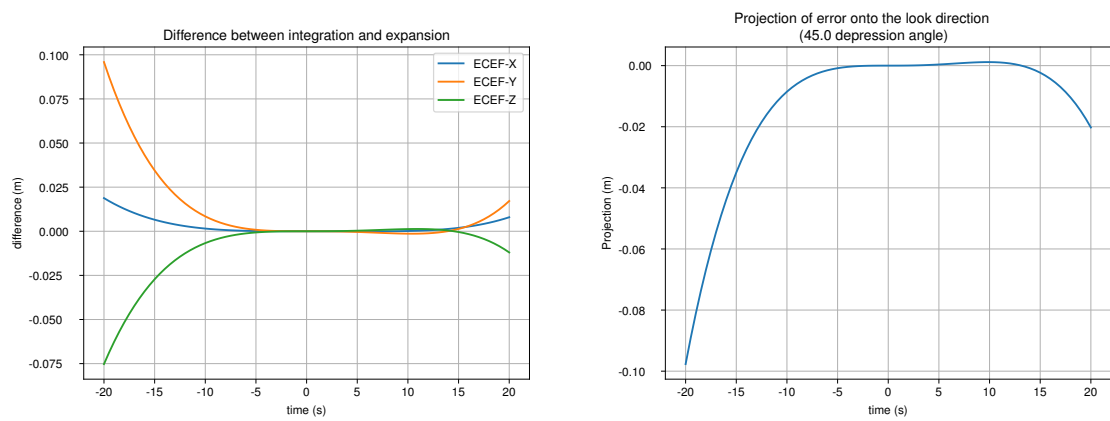


Figure 14: Terrasar-X 1650: United States, ascending

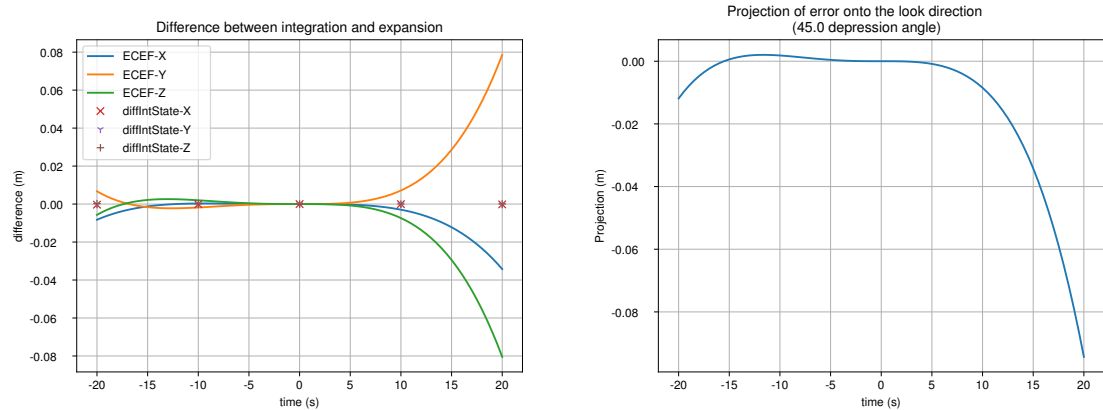


Figure 15: Sentinel-1 4591: Canada, descending

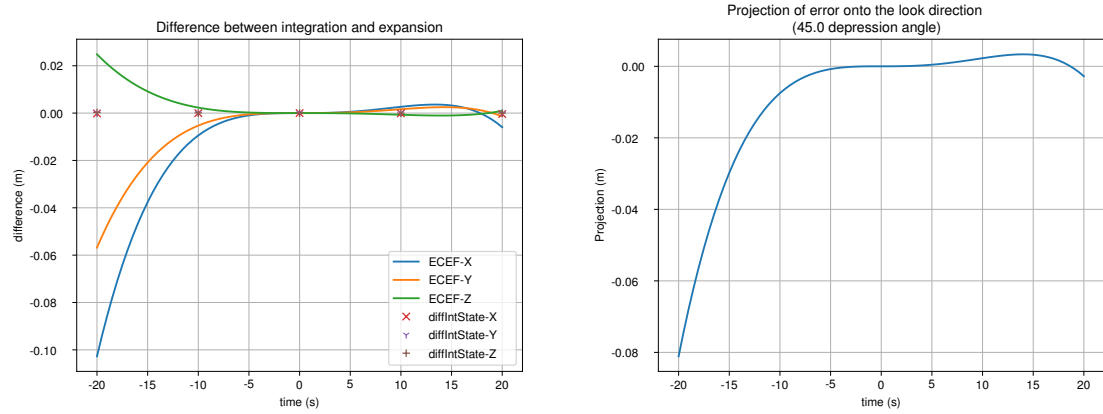


Figure 16: Sentinel-1 1727: Zambia, descending

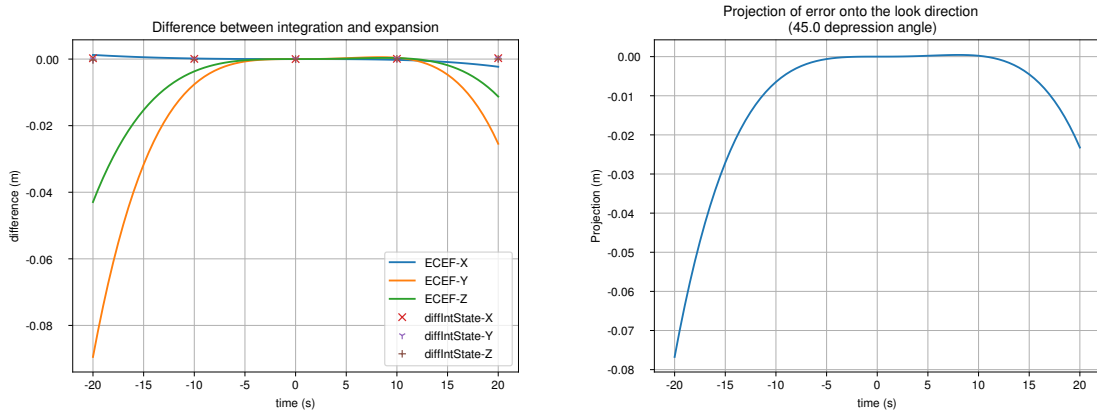


Figure 17: Sentinel-1 4418: India, ascending

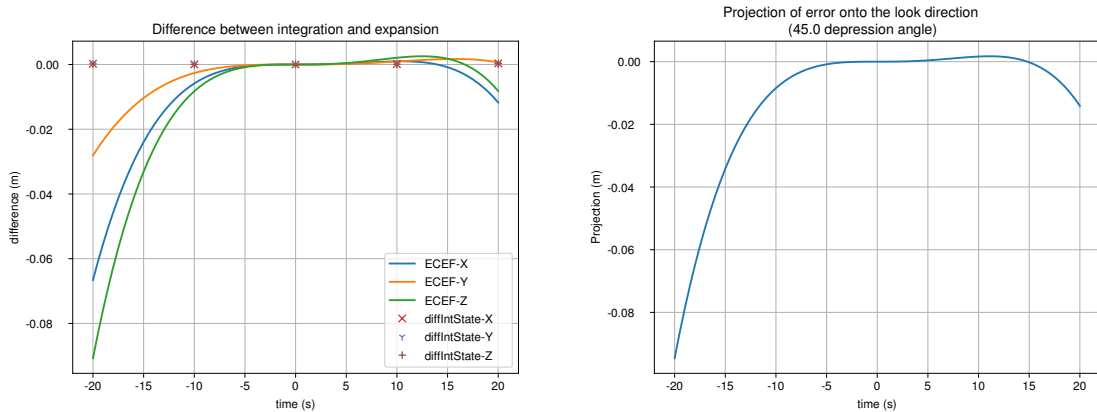


Figure 18: Sentinel-1 5650: Russia, ascending

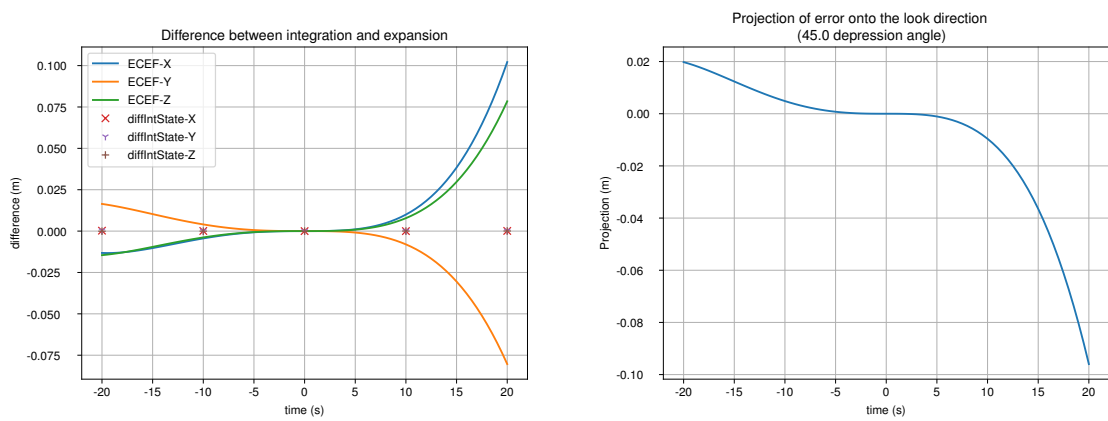


Figure 19: Sentinel-1 3725: Australia, ascending

7 Arclength-parameterized range function

As the range history plays a critical role in the development of the SAR signal model, this section relates the previously developed arclength parameterized satellite curve to the range history of a scatterer. The range history defined in this section assumes that the satellite trajectory follows $\mathbf{c}_p(s)$.

For a scatterer at point \mathbf{x} , define the range vector as $\mathbf{r}(s, \mathbf{x}) = \mathbf{c}_p(s) - \mathbf{x}$. There is a value, $s_{\mathbf{x}}$, such that $\mathbf{c}_p(s_{\mathbf{x}}) - \mathbf{x}$ is perpendicular to $\mathbf{c}'_p(s_{\mathbf{x}})$. That is, there exists a broadside arclength parameter⁷. Further, \mathbf{x} can be completely determined by

$$\mathbf{x} = \mathbf{c}_p(s_{\mathbf{x}}) + r \cos \phi \mathbf{N}(s_{\mathbf{x}}) + r \sin \phi \mathbf{B}(s_{\mathbf{x}}), \quad (32)$$

where $r = |\mathbf{c}_p(s_{\mathbf{x}}) - \mathbf{x}|$ (in meters) and $r \cos \phi = [\mathbf{x} - \mathbf{c}_p(s_{\mathbf{x}})] \cdot \mathbf{N}(s_{\mathbf{x}})$. One notes that ϕ relates to the off-nadir angle of observation.

One can define the “nearest”-range vector associated to the point \mathbf{x} as

$$\mathbf{r}(s_{\mathbf{x}}, \mathbf{x}) = r \cos \phi \mathbf{N}(s_{\mathbf{x}}) + r \sin \phi \mathbf{B}(s_{\mathbf{x}}). \quad (33)$$

Appendix C uses (22) and the above coordinate transformation $\mathbf{x} \rightarrow (r, s_{\mathbf{x}}, \phi)$ to produce the highly-accurate approximation that

$$r^2(s, \mathbf{x}) = |\mathbf{c}_p(s) - \mathbf{x}|^2 = \sum_{k=0}^6 a_k (s - s_{\mathbf{x}})^k \quad (34)$$

with the following coefficients valid in the neighbourhood of some chosen point of expansion, s_0 (with $\kappa_0, \tau_0, \kappa'_0$ evaluated at s_0)

$$a_0 = r^2 \quad (35)$$

$$a_1 = 0 \quad (36)$$

$$a_2 = 1 - \kappa_0 r \cos \phi \quad (37)$$

$$a_3 = -\frac{r}{3}(\kappa_0 \tau_0 \sin \phi + \kappa'_0 \cos \phi) \quad (38)$$

$$a_4 = -\frac{\kappa_0^2}{12} \quad (39)$$

$$a_5 = 0 \quad (40)$$

$$a_6 = 0, \quad (41)$$

The third and fourth order terms a_3, a_4 become non-negligible for very high azimuth resolution modes such as the TerraSAR-X staring spotlight mode. These effects are handled numerically in [26].

Note that the expression for \mathbf{x} has been defined by the point $s_{\mathbf{x}}$ where the satellite tangent vector makes a right angle to the range vector. The expression can be modified to any other angle if one desires to incorporate a squint angle.

⁷ at broadside, the tangent vector (aligned with the satellite velocity vector) is perpendicular to the vector connecting the satellite position vector with the target vector

7.1 Residual error in the range function

Note that because, as figures 10 to 19 demonstrate, there is a slight deviation from the path assumed in this section, the true range function should include an error term. Because this error is small, it can be approximated by

$$\delta_r(s, \mathbf{x}) = [\mathbf{c}_s(s) - \mathbf{c}_p(s)] \cdot \hat{\mathbf{r}}(s, \mathbf{x}) \quad (42)$$

In the case of very long synthetic apertures, this residual range error term will have to be compensated for. If it is assumed that the set of look vectors for the synthetic aperture and for the entire scene do not vary too much, the above may be simplified to

$$\delta_r(s, \mathbf{x}) \approx \delta_{r_0}(s) = [\mathbf{c}_s(s) - \mathbf{c}_p(s)] \cdot \hat{\mathbf{r}}_0 \quad (43)$$

where $\hat{\mathbf{r}}_0$ is some representative look vector for the scene (the average look vector, for instance).

8 The SAR signal in arclength space

This section derives the signal model for a single channel in the wavenumber domain. The term channel refers to a transmit and receive pair and each channel, considered here in isolation, is assumed to be a component of a multi-channel system. The signal derived in this section applies to wideband systems. Special care is taken to ensure that the antenna pattern gain functions are accurately represented as they play an important role in multi-channel signal processing algorithms. The material in this section reviews some concepts already published in the SAR literature, [27, 18, 28, 29, 30], but with greater care given to the antenna patterns and with, in some cases, simplified derivations.

As introduced in [31], let the parameterized satellite position be given by $\mathbf{c}_s(s)$, while the point scatterer position is given by \mathbf{x} . In the chosen coordinate system, the point scatterer is not moving, only the satellite.

At the front-end of the sequence of operations, electronic components mix a desired baseband waveform, $p(\tau)$, up to the carrier frequency, ω_0 , to yield the signal to be transmitted⁸. This signal is represented as the real part of

$$z(\tau) = p(\tau)e^{i\omega_0\tau} \quad (44)$$

The signal travels down to the surface and a delayed version returns to the radar after reflection from the terrain. For any given s , the distance that the signal must travel is given by

$$2|\mathbf{c}_s(s) - \mathbf{x}| = 2r(s, \mathbf{x}) + 2\delta_{r_0}(s) \quad (45)$$

⁸ Waveforms can also be generated directly at the carrier.

From here onward, we shall omit the small range error term, $2\delta_{r_0}(s)$, in places where it has no impact. For instance it is omitted from the inverse range-squared term and from the look direction in the antenna patterns.

If the wave propagates with speed c , then the measured return signal is proportional to

$$z \left(\tau - \frac{2r(s, \mathbf{x}) + 2\delta_{r_0}(s)}{c} \right) \quad (46)$$

8.1 Scene measurement through multiple antenna patterns

The following considers a single element of a multi-aperture antenna system. This single element is composed of a transmit and a receive antenna where the transmit and receive antennas are described by their gain patterns and phase characteristics. As a specific example, such an element could be realized by utilizing subapertures on a phased-array as described in Section F.

Each antenna pattern in the system plays a critical role in multi-channel signal processing. Simple antennas, such as the dipole antenna, and simple antenna models, such as a uniformly-excited aperture or the uniformly-spaced phased-array factor, yield directivity patterns that depend on the wavelength and have beamwidths and gain patterns which depend on the dimensions of the antenna in a given coordinate system.

For an antenna in the far-field, the effective antenna pattern may be represented as

$$A_n[\hat{\mathbf{r}}(s, \mathbf{x}), \mathbf{p}_n(s)] = e^{-2\frac{2\pi i}{\lambda} \hat{\mathbf{r}}(s, \mathbf{x}) \cdot \mathbf{p}_n(s)} D_n[\lambda, \hat{\mathbf{r}}(s, \mathbf{x})] \quad (47)$$

where λ is the narrowband wavelength, $\mathbf{p}_n(s)$ represents the coordinate of the phase-centre of antenna n in a reference frame centered on the radar platform, $D_n(\cdot)$ is the two-way antenna pattern amplitude (the product of the transmit antenna pattern and the receive antenna pattern), and $\hat{\mathbf{r}}(s, \mathbf{x})$ is the look vector defined as $\hat{\mathbf{r}}(s, \mathbf{x}) = \mathbf{r}(s, \mathbf{x})/r(s, \mathbf{x})$. If the two-way antenna pattern depends on two different phase-centres, located at $\mathbf{p}_{n_{Tx}}(s)$ and $\mathbf{p}_{n_{Rx}}(s)$, then we define

$$\mathbf{p}_n(s) = \frac{1}{2} [\mathbf{p}_{n_{Tx}}(s) + \mathbf{p}_{n_{Rx}}(s)] \quad (48)$$

The wideband generalization sees different values for the carrier wavelength in (47) so that as λ increases, the antenna can measure over a larger range of angles. Conversely, as λ decreases, the antenna beamwidth narrows.

By defining $2\pi/\lambda = (\omega + \omega_0)/c = k_r/2$, one can write the argument to the antenna pattern as

$$A_n[k_r, \hat{\mathbf{r}}(s, \mathbf{x})] = e^{-ik_r \hat{\mathbf{r}}(s, \mathbf{x}) \cdot \mathbf{p}_n(s)} D_n[k_r, \hat{\mathbf{r}}(s, \mathbf{x})] \quad (49)$$

where, now, k_r is not constant, but free to wander over a range of values to accommodate a wideband model.

We assume from here onwards that the antennas are “steered” so that they maintain a constant orientation relative to the satellite track in a coordinate system where the scene is stationary. That is, for regular non moving targets on the Earth’s surface, the antennas are fixed relative to the ECEF coordinate track (this is the reason that this document develops the satellite curve in the ECEF coordinate system). By using the basis vectors developed in the previous section, this means that the antenna pattern phase-centres can be described as

$$\mathbf{p}_n(s) = \alpha_n \mathbf{T}(s) + \beta_n \mathbf{N}(s) + \gamma_n \mathbf{B}(s), \quad (50)$$

where $\alpha_n, \beta_n, \gamma_n$ are constant with s . It is advantageous to rewrite the above symbolically as

$$\mathbf{p}_n(s) = \alpha_{\parallel n} \mathbf{T}(s) + \boldsymbol{\alpha}_{\perp n} \cdot \begin{bmatrix} \mathbf{N}(s) \\ \mathbf{B}(s) \end{bmatrix}, \quad (51)$$

where $\alpha_{\parallel n}$ is the projection of $\mathbf{p}_n(s)$ onto the direction of travel, $\mathbf{T}(s)$, while $\boldsymbol{\alpha}_{\perp n}$ is the vector component of $\mathbf{p}_n(s)$ that is perpendicular to $\mathbf{T}(s)$.

Accompanying the phase component of the antenna pattern, the gain can be described as

$$D_n[k_r, \hat{\mathbf{r}}(s, \mathbf{x})] = D_n[k_r, \hat{\mathbf{r}}(s, \mathbf{x}) \cdot \mathbf{T}(s), \hat{\mathbf{r}}(s, \mathbf{x}) \cdot \mathbf{N}(s), \hat{\mathbf{r}}(s, \mathbf{x}) \cdot \mathbf{B}(s)] \quad (52)$$

We assume that the gain-pattern model consists of an azimuth component (aligned with the direction of satellite motion) and an elevation component (oriented perpendicular to the direction of motion). This assumption holds for a rectangular array with one dimension of the array aligned along the satellite direction of motion. More specifically, we model the gain-pattern as

$$\begin{aligned} & D_n[k_r, \hat{\mathbf{r}}(s, \mathbf{x}) \cdot \mathbf{T}(s), \hat{\mathbf{r}}(s, \mathbf{x}) \cdot \mathbf{N}(s), \hat{\mathbf{r}}(s, \mathbf{x}) \cdot \mathbf{B}(s)] \\ &= D_{az_n}[k_r, \hat{\mathbf{r}}(s, \mathbf{x}) \cdot \mathbf{T}(s)] D_{el_n}[k_r, \hat{\mathbf{r}}(s, \mathbf{x}) \cdot \mathbf{N}(s), \hat{\mathbf{r}}(s, \mathbf{x}) \cdot \mathbf{B}(s)] \end{aligned} \quad (53)$$

The measured return signal consists of the superposition of the reflected signal from various locations over the terrain; thus, for some s , the overall return signal is given by

$$ss_n(\tau, s) = \int A_n[k_r, \hat{\mathbf{r}}(s, \mathbf{x}), \mathbf{p}_n(s)] \frac{g(\mathbf{x})}{r^2(s, \mathbf{x})} z \left(\tau - \frac{2r(s, \mathbf{x}) + 2\delta_{r_0}(s)}{c} \right) d\mathbf{x} \quad (54)$$

where $g(\mathbf{x}) \in \mathcal{C}$ denotes a stochastic process which represents the scattering response of the point scatterer at \mathbf{x} , and the term $r^2(s, \mathbf{x})$ in the denominator accounts for the fact that in the far-field, electric fields decay at a rate given by the inverse of the range, and the expression accounts for a two-way propagation of an electric field. Without loss of generality, other constant factors from the radar equation have been omitted. In any practical calculation that requires computation of the SNR, an account can be made for these factors.

8.2 Demodulation

If the return signal is mixed with $e^{-i\omega_0\tau}$, and if filters are applied to remove unwanted frequency bands, one obtains the demodulated signal

$$ss_n(\tau, s) \rightarrow ss_n(\tau, s) = \int A_n[k_r, \hat{\mathbf{r}}(s, \mathbf{x}), \mathbf{p}_n(s)] \frac{g(\mathbf{x})}{r^2(s, \mathbf{x})} \cdot p\left(\tau - 2\frac{r(s, \mathbf{x}) + \delta_{r_0}(s)}{c}\right) e^{-2i\omega_0 \frac{r(s, \mathbf{x}) + \delta_{r_0}(s)}{c}} d\mathbf{x} \quad (55)$$

The fast-time Fourier Transform (FT) of $ss_n(\tau, s)$ may be computed as

$$Ss_n(\omega, s) = P(\omega) \int e^{-i\frac{2[\omega+\omega_0]}{c}[r(s, \mathbf{x}) + \delta_{r_0}(s)]} A_n[k_r, \hat{\mathbf{r}}(s, \mathbf{x}), \mathbf{p}_n(s)] \frac{g(\mathbf{x})}{r^2(s, \mathbf{x})} d\mathbf{x} \quad (56)$$

Recall that $k_r = \frac{2(\omega+\omega_0)}{c}$, and define $k_{r'} = \frac{2\omega}{c}$ and $k_{r_0} = \frac{2\omega_0}{c}$, to yield the processed fast-time frequency signal

$$Ss_n(k_r, s) = \mathcal{P}(k_{r'}) e^{-ik_r \delta_{r_0}(s)} \int e^{-ik_r r(s, \mathbf{x})} A_n[k_r, \hat{\mathbf{r}}(s, \mathbf{x}), \mathbf{p}_n(s)] \frac{g(\mathbf{x})}{r^2(s, \mathbf{x})} d\mathbf{x} \quad (57)$$

where $\mathcal{P}(k_{r'}) = |P(ck_{r'}/2)|$ and the absolute value has been computed by multiplying by the known conjugate phase of $P(\cdot)$. Indeed, range or pulse compression is achieved through multiplication by the conjugate phase. For instance, if the pulse is a chirp, then it is at this point that the chirp phase is removed.

Range error compensation

One can compensate for the range error term through multiplication by $e^{ik_r \delta_{r_0}(s)}$. This operation simply accounts for the time delay between the ideal path and the real path of the satellite.

A simplification is possible in the case of small range errors. In this case, assume that (57) is multiplied by $e^{ik_{r_0} \delta_{r_0}(s)}$. This leads to a leading term given by $\mathcal{P}(k_{r'}) e^{-ik_{r'} \delta_{r_0}(s)}$ which can be interpreted as a shift of the pulse compressed signal by $\delta_{r_0}(s)$ at each point s .

If the signal is sampled at a spatial sampling rate proportional to the range resolution, δ_r , then the baseband pulse will be shifted by $\delta_{r_0}(s)/\delta_r$ samples in the range direction. This suggests that a phase compensation is valid so long as range error is small compared to the range resolution. One could take, as a rule of thumb, that

$$|\delta_{r_0}(s)| \leq \frac{\delta_r}{8} \quad (58)$$

In the case of 10cm range resolution, this means the the range errors over the synthetic aperture should be less than approximately 1cm. Note that all data plotted in figures 10 to 19 satisfy the condition of (58) over the period of ± 10 seconds.

8.3 Stationary phase approximation

The Fourier transform over s is given by

$$\begin{aligned} \mathcal{SS}_n(k_r, k_s) &= \int \mathcal{S}s_n(k_r, s) \exp\left(-ik_s s\right) ds \\ &= \mathcal{P}(k_{r'}) \iint A_n[k_r, \hat{\mathbf{r}}(s, \mathbf{x}), \mathbf{p}_n(s)] \frac{g(\mathbf{x}) e^{-ik_r \delta_{r_0}(s)}}{r^2(s, \mathbf{x})} e^{-ik_r r(s, \mathbf{x}) - ik_s s} d\mathbf{x} ds. \end{aligned} \quad (59)$$

The stationary phase procedure is an asymptotic approximation procedure that can be used to accurately approximate the above integral. The approximation is given by

$$\int f(s) e^{i\Phi(s)} ds = e^{i\Phi(s_p)} f(s_p) \sqrt{\frac{2\pi i}{\ddot{\Phi}(s_p)}}, \quad (60)$$

where s_p is the value of s such that $\dot{\Phi}(s_p) = 0$ and $f(s)$ is some slowly varying smooth function. The approximation becomes ever more accurate for increasing values of the second derivative, $\ddot{\Phi}(s_p)$, [32]. We shall assume, and demonstrate through results in Section 12, that the stationary phase approximation introduces no significant error.

We shall apply the above approximation to compute the Fourier transform in (59) by setting

$$f(s) = A_n[k_r, \hat{\mathbf{r}}(s, \mathbf{x}), \mathbf{p}_n(s)] \frac{g(\mathbf{x}) e^{-ik_r \delta_{r_0}(s)}}{r^2(s, \mathbf{x})} \quad (61)$$

and

$$\Phi(s) = -k_r r(s, \mathbf{x}) - k_s s \quad (62)$$

By taking the derivative of $\Phi(s)$ and equating the result to zero, one finds that s_p is the solution to the following equation

$$k_s = -k_r \frac{dr(s, \mathbf{x})}{ds} = -k_r \hat{\mathbf{r}}(s, \mathbf{x}) \cdot \frac{d\{\mathbf{c}_s(s) - \mathbf{x}\}}{ds} = -k_r \hat{\mathbf{r}}(s, \mathbf{x}) \cdot \mathbf{T}(s) \quad (63)$$

One notes that the above expression is found in the first part of (51).

9 Stationary phase

This section presents the results of applying the stationary phase approximation to the fast-time, arclength parameterized signal model. The final result is seen to be a generalization of the classical hyperbolic model with additional terms of the higher order a_3 and a_4 appearing in the range equation and the Stolz interpolation.

We shall find at the end of the section that the presence of the higher order terms results in a Stolz interpolation scheme where there is no closed form for the interpolation points.

Instead, interpolation points are given as the roots of a mathematical expression and are assumed (and demonstrated) to be numerically computable.

Recall from (34) that

$$\begin{aligned} r(s, \mathbf{x}) &= \sqrt{|\mathbf{c}_p(s) - \mathbf{x}|^2} = \sqrt{\sum_{k=0}^4 a_k (s - s_{\mathbf{x}})^k} \\ &= \sqrt{r^2 + a_2(s - s_{\mathbf{x}})^2 + a_3(s - s_{\mathbf{x}})^3 + a_4(s - s_{\mathbf{x}})^4} \end{aligned} \quad (64)$$

The phase of the function in (59) is then given by

$$\Phi(s) = -k_r \sqrt{r^2 + a_2(s - s_{\mathbf{x}})^2 + a_3(s - s_{\mathbf{x}})^3 + a_4(s - s_{\mathbf{x}})^4} - k_s s \quad (65)$$

In order to simplify the calculation, let

$$\begin{aligned} -r \tan \theta_s(s) &= \sqrt{a_2 s^2 + a_3 s^3 + a_4 s^4} \\ &= s \sqrt{a_2 + a_3 s + a_4 s^2} \\ &= sg(s) \end{aligned} \quad (66)$$

The above relation is really only a mathematical convenience; however, in the simple linear trajectory case (i.e. airborne SAR), the angle $\theta_s(s)$ corresponds to the look angle. By substituting this relation in (65), one finds that

$$\begin{aligned} \Phi(s) &= -rk_r \sec \theta_s(s - s_{\mathbf{x}}) - k_s s \\ &= -rk_r \sec \theta_s(s - s_{\mathbf{x}}) - k_s(s - s_{\mathbf{x}}) - k_s s_{\mathbf{x}} \end{aligned} \quad (67)$$

Now

$$\begin{aligned} \frac{d\Phi(s)}{ds} &= \frac{d\Phi(s)}{d(s - s_{\mathbf{x}})} \frac{d(s - s_{\mathbf{x}})}{ds} \\ &= -rk_r \tan \theta_s(s - s_{\mathbf{x}}) \sec \theta_s(s - s_{\mathbf{x}}) \frac{d\theta_s(s - s_{\mathbf{x}})}{d(s - s_{\mathbf{x}})} - k_s, \end{aligned} \quad (68)$$

and the stationary phase prescription instructs that this should be equated to zero, thus

$$-rk_r \tan \theta_s(s - s_{\mathbf{x}}) \sec \theta_s(s - s_{\mathbf{x}}) \frac{d\theta_s(s - s_{\mathbf{x}})}{d(s - s_{\mathbf{x}})} = k_s. \quad (69)$$

On the other hand, by taking the derivative of (66), one calculates that

$$-r \sec^2 \theta_s(s - s_{\mathbf{x}}) \frac{d\theta_s(s - s_{\mathbf{x}})}{d(s - s_{\mathbf{x}})} = g(s - s_{\mathbf{x}}) + (s - s_{\mathbf{x}}) \frac{dg(s - s_{\mathbf{x}})}{d(s - s_{\mathbf{x}})}, \quad (70)$$

which means that the stationary phase value s_p is the value which satisfies

$$k_r \sin \theta_s(s_p - s_{\mathbf{x}}) \left[g(s_p - s_{\mathbf{x}}) + (s_p - s_{\mathbf{x}}) \frac{dg(s_p - s_{\mathbf{x}})}{d(s_p - s_{\mathbf{x}})} \right] = k_s. \quad (71)$$

By letting $s^* = s_p - s_{\mathbf{x}}$, the preceding becomes

$$k_r \sin \theta_s(s^*) \left[g(s^*) + s^* \frac{dg(s^*)}{ds^*} \right] = k_s. \quad (72)$$

9.1 Relation between arclength and wavenumber

The remainder of this section seeks to present a means to invert (72), that is, to compute some form of s_p or θ_s given wavenumbers k_s and k_r .

This subsection develops one of the key approximations used to derive the Stolz interpolation points. We begin by recalling from (66) that

$$-r \tan \theta_s(s) = sg(s) \quad (73)$$

Let $x = -r \tan \theta_s(s)$ so that

$$x = sg(s) \quad (74)$$

To invert the above, we note that

$$\begin{aligned} s &= \frac{x}{g(s)} = \frac{x}{g\left(\frac{x}{g(s)}\right)} = \frac{x}{g\left(\frac{x}{g\left(\frac{x}{g(s)}\right)}\right)} = \dots \\ g(s) &= g\left(\frac{x}{g(s)}\right) = g\left(\frac{x}{g\left(\frac{x}{g(s)}\right)}\right) = \dots \end{aligned} \quad (75)$$

where the two expressions above are terminated after some number of compositions with $s = 0$. The above two equations are the key expressions used in the approximation. Section D provides a mathematical argument explaining why the above iterative approach converges.

From the definition of $g(s)$, one computes that

$$g(s) + s \frac{dg(s)}{ds} = g(s) + \frac{a_3 s + 2a_4 s^2}{2g(s)}. \quad (76)$$

Thus,

$$g(s) + s \frac{dg(s)}{ds} = g(s) + \frac{a_3 x}{2g^2(s)} + \frac{a_4 x^2}{g^3(s)} \quad (77)$$

The above can be inserted into (72) to yield an expression that relates, on the left, a function that depends on $\sin \theta_s(s^*)$ (which is written as $\sin \theta_s$, with $\tan \theta_s = \sin \theta_s / \sqrt{1 - \sin^2 \theta_s}$) to, on the right, a function of k_r, k_s .

$$-\frac{x}{\sqrt{r^2 + x^2}} \left[g[s^*(x)] + \frac{a_3 x}{2g^2[s^*(x)]} + \frac{a_4 x^2}{g^3[s^*(x)]} \right] = \frac{k_s}{k_r}. \quad (78)$$

To be specific, with $g[s^*(x)]$ evaluated with (75), the above can be considered as

$$f(x; r) = \frac{k_s}{k_r} \quad (79)$$

and one observes that only in the case that $a_3 = a_4 = 0$ is the above independent of r .

Equation (75) permits us to write the stationary phase expression, (67), as

$$\begin{aligned}
 \Phi(s_p) &= -rk_r \sec \theta_s - s^* k_s - k_s s_x \\
 &= -rk_r \sec \theta_s - k_s \frac{x}{g[s^*(x)]} - k_s s_x \\
 &= -r \left[k_r \sec \theta_s - k_s \frac{\tan \theta_s}{g[s^*(x)]} \right] - k_s s_x.
 \end{aligned} \tag{80}$$

By inverting (79), one can compute x as a function of k_r, k_s . From $x = -r \tan \theta_s(s)$, the value of $\tan \theta_s(s)$ can be computed and this can be substituted into the above to yield a phase function dependent only upon the spatial wavenumbers (and the range). The first term (the term multiplied by r) in the last line of (80) thus represents a modified Stoltz interpolation function which can easily be computed numerically. Appendix E outlines the particular implementation of the numerical approach adopted in this work.

Note that in the case $a_3 = a_4 = 0$, the above reduces to

$$\Phi(s_p) = -r \sqrt{k_r^2 - \frac{k_s^2}{a_2}} - k_s s_x. \tag{81}$$

9.2 Antenna pattern angles

In this section, we examine the implications of the stationary phase approximation on the antenna pattern. While the Stoltz interpolation and the range equation are critical for single-channel SAR signal processing, multi-channel signal processing further demands an accurate description of the antenna pattern, in this case, in the wavenumber domain. The material presented in this section relies heavily upon both the Frenet-Serret equations and the vector calculus expansions referenced in Appendix A.

Before switching to the main content of this section, it is worth discussing some of the physical implications of the results presented at the end. One of the primary results shows that in the neighbourhood of some ground point, chosen for SAR processing, the multi-channel signal reconstruction algorithms can be considered independent of the range wavenumber, k_r ⁹. Signals from the multiple channels can be combined into a single response, equivalent to what one would have expected from a single adequately-sampled SAR, without regard to a varying k_r . This simplifies the multi-channel signal processing. Note that after multi-channel signal processing, the produced signal still needs to be SAR processed, and this SAR processing does depend on k_r .

Assume that the point around which we wish to SAR process the signals is given by r_0, s_{t_0}, ϕ_0 . Our objective is to expand the signals around this point with the demonstrated assumption that over a neighbourhood of significant size, the expansion is accurate enough for SAR processing.

⁹ This independence does not include potential implementation of a frequency domain implementation of a fast-time delay

The quantities $\hat{\mathbf{r}}(s, \mathbf{x}) \cdot \mathbf{T}(s)$, $\hat{\mathbf{r}}(s, \mathbf{x}) \cdot \mathbf{N}(s)$ and $\hat{\mathbf{r}}(s, \mathbf{x}) \cdot \mathbf{B}(s)$ all appear in the antenna pattern arguments, both in the phase component through

$$e^{-ik_r \hat{\mathbf{r}}(s, \mathbf{x}) \cdot \mathbf{p}_n(s)} \quad (82)$$

since

$$\hat{\mathbf{r}}(s, \mathbf{x}) \cdot \mathbf{p}_n(s) = \alpha_{\parallel n} \hat{\mathbf{r}}(s, \mathbf{x}) \cdot \mathbf{T}(s) + \boldsymbol{\alpha}_{\perp n} \cdot \begin{bmatrix} \hat{\mathbf{r}}(s, \mathbf{x}) \cdot \mathbf{N}(s) \\ \hat{\mathbf{r}}(s, \mathbf{x}) \cdot \mathbf{B}(s) \end{bmatrix}, \quad (83)$$

and in the antenna gain component through

$$\begin{aligned} D_n[k_r, \hat{\mathbf{r}}(s, \mathbf{x})] &= \\ D_{azn}[k_r, \hat{\mathbf{r}}(s, \mathbf{x}) \cdot \mathbf{T}(s)] D_{eln}[k_r, \hat{\mathbf{r}}(s, \mathbf{x}) \cdot \mathbf{N}(s), \hat{\mathbf{r}}(s, \mathbf{x}) \cdot \mathbf{B}(s)]. \end{aligned} \quad (84)$$

According to (60), these all need to be evaluated at the stationary point s_p . We have already seen from equation (63) that

$$\hat{\mathbf{r}}(s_p) \cdot \mathbf{T}(s_p) = -k_s/k_r \quad (85)$$

Appendix G further calculates that

$$\hat{\mathbf{r}}(s_p) \cdot \mathbf{N}(s_p) \approx \cos \phi_0 + \frac{r}{r_0} \sin \phi_0 \sin(\phi - \phi_0) \quad (86)$$

$$\hat{\mathbf{r}}(s_p) \cdot \mathbf{B}(s_p) \approx \sin \phi_0 - \frac{r}{r_0} \cos \phi_0 \sin(\phi - \phi_0) \quad (87)$$

Which leads the following

$$\begin{aligned} \alpha_{\parallel n} k_r \hat{\mathbf{r}}(s_p) \cdot \mathbf{T}(s_p) + k_r \boldsymbol{\alpha}_{\perp n} \cdot \begin{bmatrix} \hat{\mathbf{r}}(s_p) \cdot \mathbf{N}(s_p) \\ \hat{\mathbf{r}}(s_p) \cdot \mathbf{B}(s_p) \end{bmatrix} \\ = -\alpha_{\parallel n} k_s + k_r \boldsymbol{\alpha}_{\perp n} \cdot \hat{\mathbf{r}}_0 + k_r r \frac{\boldsymbol{\alpha}_{\perp n} \cdot \hat{\mathbf{r}}_0}{r_0} \sin(\phi - \phi_0) \end{aligned} \quad (88)$$

The above shows that even in the case of an across-track baseline, it is the component of this baseline in the look direction (the second term, $k_r \boldsymbol{\alpha}_{\perp n} \cdot \hat{\mathbf{r}}_0$) that has most effect on the multi-channel phase. This physically makes sense as the ranges to the targets on the ground do not change significantly with across-track baselines in the cross-look-direction. The expression further shows that a compensation for the look-direction component of the across-track baseline can be computed and applied in the neighbourhood of the selected expansion point. This correction should be applied before any azimuth processing so as to eliminate the majority of effects stemming from an across-track baseline.

9.3 The 2-D wavenumber signal

Assuming that the across-track compensation has been applied, i.e. that the signal has been multiplied by

$$H_{al} = e^{ik_r \boldsymbol{\alpha}_{\perp n} \cdot \hat{\mathbf{r}}_0}, \quad (89)$$

and that the component in the cross-look direction,

$$H_{cl} = e^{-ik_r r \frac{\alpha_{\perp n} \cdot \hat{r}_{0\perp}}{r_0} \sin(\phi - \phi_0)} \rightarrow 1, \quad (90)$$

the expression for the signal in k -space is given by

$$\mathcal{SS}_n(k_r, k_s) = e^{-ik_r \delta_{r_0}(s_p[k_r, k_s])} e^{i\alpha_{\parallel n} k_s} D_{az_n}[k_r, -k_s/k_r] \Phi_n(k_r, k_s) \quad (91)$$

where

$$\Phi_n(k_r, k_s) = \sqrt{2\pi i} \mathcal{P}(k_{r'}) \int \frac{g(\mathbf{x}) D_{el_n}[k_r, \cos \phi, \sin \phi]}{\sqrt{\ddot{\Phi}(s_p)}} e^{i\Phi(s_p[k_r, k_s])} d\mathbf{x} \quad (92)$$

and $\Phi(s_p[k_r, k_s])$ is as given in (80).

In the case that the elevation component of the gain pattern is constant across all channels, the above simplifies to

$$\mathcal{SS}_n(k_r, k_s) = e^{-ik_r \delta_{r_0}(s_p[k_r, k_s])} e^{i\alpha_{\parallel n} k_s} D_{az_n}[k_r, -k_s/k_r] \Phi(k_r, k_s) \quad (93)$$

where

$$\Phi(k_r, k_s) = \mathcal{P}(k_{r'}) \int \frac{D_{el}[k_r, \cos \phi, \sin \phi]}{r^2} g(\mathbf{x}) e^{i\Phi(s_p[k_r, k_s])} d\mathbf{x} \quad (94)$$

In the above, $\sqrt{\ddot{\Phi}(s_p)}$ and $\sqrt{2\pi i}$ have been omitted because the first only varies slowly over the parameters while the second is a constant. Also $r^2(s_p[k_r, k_s])$ is approximated with r^2 because it is assumed that this weighting of the spectrum with range does not vary significantly. With the signal as written, one sees that the elevation gain pattern and the inverse range relationship simply modulate the reflectivity (through the radar equation) according to the geometry.

9.4 Modified Stoltz interpolation

If the signal has been sampled adequately and is evaluated at a set of different points given by

$$k_{rs} = k_r \sec \theta_s - k_s \frac{\tan \theta_s}{g[s^*(x)]} = \psi(k_r, k_s), \quad (95)$$

then

$$e^{i\Phi(s_p[k_{rs} = \psi(k_r, k_s), k_s])} = e^{-irk_{rs}} e^{-is_x k_s} \quad (96)$$

and

$$\begin{aligned} \Phi[k_{r_s} = \psi(k_r; k_s), k_s] = \\ \mathcal{P}(k_{r'}) \int \frac{\text{Del}[\psi^{-1}(k_{r_s}; k_s), \cos \phi, \sin \phi]}{r^2} g(\mathbf{x}) e^{-irk_{r_s}} e^{-is_{\mathbf{x}} k_s} d\mathbf{x} \end{aligned} \quad (97)$$

This formulation illustrates that the measured 2-D wavenumber representation, evaluated at the transformed points, is a modulated Fourier Transform of the reflectivity. Although the reflectivity is expressed in terms of \mathbf{x} , it can be transformed into reflectivity as a function of $r, s_{\mathbf{x}}$ and ϕ . The integration means that two points with common r and $s_{\mathbf{x}}$ but different values for ϕ end up superimposed.

An adequately-sampled SAR signal, with the modified Stoltz interpolation scheme outlined in this section, can be processed with the well-known Wavenumber processing algorithms of, for instance, [30, 27, 33].

The proposed numerical Stoltz interpolation can be challenging to implement. For this reason, Appendix E outlines the particular implementation of the numerical approach adopted in this work.

We have repeatedly stated that the above approach only works if the signal has been adequately sampled. In the case of a multichannel configuration where the channels are deliberately undersampled, because of a desire to implement a High-Resolution, Wide-Swath (HRWS) configuration, an unambiguous signal must first be reconstructed; only then can the Wavenumber processing algorithm be implemented. Reconstruction of such a signal from undersampled channels is the task of Section 11.

10 Multichannel signal processing for high resolution

The material in Section 3 depends on a strict timing regime. A practical system may only operate with near-ideal timing conditions and this raises the questions of impact and how best to process the data under these conditions.

Even if timing conditions are perfect, i.e. the Displaced Phase Centre Antenna (DPCA) condition has been met, [34], the best approach to data processing needs further investigation. A simple approach first concatenates the measurements from each beam into a uniformly-sampled time series and then transforms the data from the fast-time, slow-time domain into the fast-time Doppler domain. Given that, for each beam direction, the data correspond to different Doppler centroids, one could assign each response to different portions of the Doppler spectrum (or to different Doppler frequency bands). The union of these Doppler frequency bands corresponds to a wider Doppler spectrum and thereby to higher overall azimuth resolution. If the Doppler bands are non-overlapping, the concept of the union of the frequency bands is straight-forward. Optimal processing of Doppler bands that do overlap, however, requires a more rigorous approach. Optimal processing of data collected under non-ideal timing further calls for a flexible yet robust processing approach.

Given that processing should apply to very high-resolution systems, it is best that the approach be suitable for a wide-band system.

11 Multi-channel SAR processing

With the signal represented in the 2-D frequency domain we are finally ready to derive the multi-channel processing filters.

This section derives signal processing methods to reconstruct an optimal scalar spectrum for wideband SAR imaging. It is assumed that the antennas are fixed relative to track - *i.e.*, that one can model the signal according to (93). Further, it is assumed that the antenna positions relative to track are known. The relative motion parameters are also known and the objective is to reproduce a high-resolution image from the multi-channel signal which is aliased according to the PRF.

11.1 Linear filtering to extract signal components

The linear filtering approach applies a multi-dimensional filter in the wavenumber domain so that a scalar reconstructed signal, denoted by $\mathcal{Z}\mathcal{Z}_R(k_r, k_s)$, is created via

$$\mathcal{Z}\mathcal{Z}_R(k_r, k_s + lk_{s_p}) = \mathbf{b}_l^\dagger(k_r, k_s) \mathbf{z}(k_r, k_s) \quad (98)$$

The challenge is to find the vectors $\mathbf{b}_l(k_r, k_s)$ that yield the desired quality of signal. The goal of this section is to determine appropriate choices for $\mathbf{b}_l(k_r, k_s)$ such that the reconstructed, scalar signal,

$$\mathcal{Z}\mathcal{Z}_R(k_r, k_s + lk_{s_p}) = \mathbf{b}_l^\dagger(k_r, k_s) \mathbf{z}(k_r, k_s) \quad (99)$$

is as free from azimuth ambiguities as possible and that it does not suffer catastrophic losses in SNR.

11.2 Matrix-vector model for the aliased signal

The derivation of the filters is aided by rewriting the multi-channel signal in matrix-vector notation, [34].

Recall that an N -channel system measurement can be represented as

$$\begin{aligned} \mathbf{z}(k_r, k_s) &= \sum_{l \in \mathcal{L}} \mathbf{s}(k_r, k_s + lk_{s_p}) + \mathbf{n}(k_r, k_s) \\ &= \sum_{l \in \mathcal{L}} \mathbf{a}(k_r, k_s) \Phi(k_r, k_s + lk_{s_p}) + \mathbf{n}(k_r, k_s) \end{aligned} \quad (100)$$

where

$$\mathbf{a}(k_r, k_s) = \begin{bmatrix} e^{i\alpha_{\parallel 1} k_s} D_{az_1}[k_r, -k_s/k_r] \\ e^{i\alpha_{\parallel 2} k_s} D_{az_2}[k_r, -k_s/k_r] \\ \dots \\ e^{i\alpha_{\parallel N} k_s} D_{az_N}[k_r, -k_s/k_r] \end{bmatrix} \quad (101)$$

and $\Phi(k_r, k_s)$ is defined in (94).

The summation can be incorporated into a matrix multiplication to yield

$$\mathbf{z}(k_r, k_s) = \mathbf{H}(k_r, k_s)\Phi(k_r, k_s) + \mathbf{n}(k_r, k_s) \quad (102)$$

where the matrix \mathbf{H} is composed of the vectors \mathbf{a} according to

$$\mathbf{H}(k_r, k_s) = [\dots \mathbf{a}(k_r, k_s - k_{sp}) \mathbf{a}(k_r, k_s) \dots] \quad (103)$$

and

$$\Phi(k_r, k_s) = \begin{bmatrix} \vdots \\ \Phi(k_r, k_s - k_{sp}) \\ \Phi(k_r, k_s) \\ \vdots \end{bmatrix} \quad (104)$$

The matrix \mathbf{H} may be fat, skinny or square¹⁰ according to the number of channels and the degree of aliasing of a band-limited signal.

11.3 A cost function for HRWS processing

Our wish is to multiply the measured signal in (102) by some matrix, $\mathbf{B}(k_r, k_s)$, such that $\mathbf{B}(k_r, k_s)\mathbf{H}(k_r, k_s) = \mathbf{D}(k_r, k_s)$ where $\mathbf{D}(k_r, k_s)$ is some desired diagonal matrix. This desired matrix, resulting from the product, should ideally be one that provides good radiometric resolution. A practical choice is, for instance, the average antenna pattern. Note that if $\mathbf{D}(k_r, k_s)$ is diagonal, then it is straight-forward to read the individual aliased components of the signal as they will just correspond to the diagonal element of $\mathbf{D}(k_r, k_s)$ multiplied by the corresponding row of $\Phi(k_r, k_s)$.

In particular, because, heuristically, we are interested in the signal measured by the *average* antenna pattern, let the diagonal elements of $\mathbf{D}(k_r, k_s)$ be given by

$$D_{ll}(k_r, k_s) = \sqrt{\sum_n |\mathbf{D}_{az_n}[\hat{\mathbf{r}}_l(k_r, k_s)]|^2} \quad (105)$$

where

$$\hat{\mathbf{r}}_l(k_r, k_s) = \hat{\mathbf{r}}(k_r, k_s + lk_{sp}) \quad (106)$$

¹⁰ A matrix of size $m \times n$ is square if $m = n$, skinny if $m > n$, and fat if $m < n$.

For different values of l , the range look vector points in different directions. Our choice of $\mathbf{D}(k_r, k_s)$ contains elements corresponding to the signal returned from the different directions corresponding to l (weighted by the average antenna pattern). This provides a mechanism to extract the unambiguous signal.

The minimum square error approach to computing $\mathbf{B}(k_r, k_s)$ seeks to minimise the following cost function

$$J_0 = |\mathbf{B}(k_r, k_s)\mathbf{H}(k_r, k_s) - \mathbf{D}(k_r, k_s)|^2 \quad (107)$$

where $|\cdot|^2$ denotes the Frobenius norm.

11.3.1 Amplified additive noise

Before attempting to find minimum values for J_0 , one should recognise that if we pre-multiply $\mathbf{z}(k_r, k_s)$ by $\mathbf{B}(k_r, k_s)$, then the additive noise term is also pre-multiplied by $\mathbf{B}(k_r, k_s)$ and this might reduce the SNR. Thus, one should simultaneously try to minimise the following cost function

$$J_1 = \mathcal{E}\{|\mathbf{B}(k_r, k_s)\boldsymbol{\nu}(k_r, k_s)|^2\} \quad (108)$$

11.3.2 Blended cost function

In the event that the solution to minimising each cost-function is different, a fair trade would see the construction of a tuneable hybrid cost-function given by

$$J_2 = \varrho J_0 + (1 - \varrho)J_1 \quad (109)$$

where $\varrho \in (0, 1]$. The solution to this problem is computed in [35] yielding the Minimum Mean Square Error (MMSE) filters given by

$$\begin{aligned} \mathbf{B}(k_r, k_s) &= \mathbf{D}(k_r, k_s)\mathbf{H}^\dagger(k_r, k_s) \\ &\left[\mathbf{H}(k_r, k_s)\mathbf{H}^\dagger(k_r, k_s) + \frac{1 - \varrho}{\varrho}\mathbf{R}_n(k_r, k_s) \right]^{-1} \end{aligned} \quad (110)$$

11.4 Section summary

This section developed the HRWS signal processing methods to construct a scalar signal with reduced or eliminated azimuth ambiguities and acceptable SNR from a vector of aliased signals. The section derived set of filters that depends on a variable parameter ϱ which controls the level of azimuth ambiguity (or residual aliasing) and the SNR. The choice of $\varrho = 1$ leads to the projection filters of [36, 37, 19]. In the general wideband case, the HRWS processing filters are k_r and k_s dependant, but for systems with no across-track baseline or narrowband systems, the processing filters depend only on k_s .

12 Simulated multi-channel signal

To demonstrate the signal processing approach, this section generates simulated signals at resolutions ranging from 40cm down to 10cm. As already mentioned, the more the resolution decreases (i.e. improves) the greater the data capture, storage and signal processing requirements. The 12cm and 10cm modes required a significant amount of processing power, time and Random Access Memory (RAM). These modes were simulated by using the Vienna Super computing Cluster (VSC) for which the authors are deeply grateful.

The simulations, with parameters listed in Table 4, were developed using the Python libraries Numba, Numpy, Scipy and Matplotlib. In the table, the swath width has been

Table 4: Simulation parameters

mode	f_p Hz	L m	L_M m	$M + 1$	Swath km	f_0 GHz	B MHz
40 cm	4500.00	20.0	4.0	5	16.5	9.65	374.74
30 cm	5000.00	21.4	3.6	6	13.5	9.65	499.65
25 cm	5142.86	24.4	3.5	7	12.7	9.65	599.58
20 cm	6428.57	19.6	2.8	7	7.5	9.65	749.48
12 cm	7500.00	24.0	2.4	10	4.5	9.65	1249.14
10 cm	8181.82	24.2	2.2	11	3.0	9.65	1498.96

computed in the slant-range. The projection onto the ground yields, as a function of the incidence angle, a longer ground swath. The estimate for the slant-range swath is computed as

$$\text{Swath}(f_p; \tau_p) = (1/f_p - 2 * \tau_p) * \frac{c}{2} \times 90\% \quad (111)$$

where τ_p is the pulse duration which was, for the table, selected as $\tau_p = 50 \times 10^{-6}$ s. A 10% margin has also been incorporated.

The satellite velocity chosen for the simulation is 7500 m/s. This means that the DPCA condition is not met for any of the simulations. All Pulse Repetition Frequency (PRF)s have been increased by a factor of 1.2 relative to the one that matches the DPCA condition.

As outlined in Figure 20, the simulator computes the back-folded signal for each of the desired channels of data, computes the processing filters, applies the filters to the back-folded data and presents the amplitude of the reconstructed signal in the Doppler domain.

12.1 Generation of the raw signals

All simulations for this paper utilize a phased array with elements of width 0.04m which are ideally spaced 0.04m apart, see Figure 21. For instance, the phased array used for the 40cm mode is described by the XML snippet shown in Listing 1.

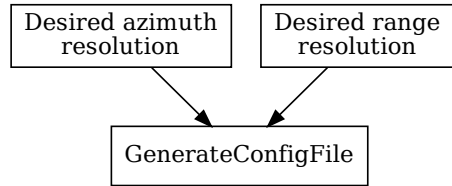


Figure 20: Simulation of the SURE signal.

```

1 <instrument>
2   <antennaArray>
3     <carrierFrequency unit="Hz">9.650e9</carrierFrequency>
4     <azimuthPositions unit="m">-9.980000 -9.940000 -9.900000 ...
5     ... 9.900000 9.940000 9.980000</azimuthPositions>
6     <azimuthElementLengths unit="m">0.040000 0.040000 0.040000 ...
7     ... 0.040000 0.040000 0.040000</azimuthElementLengths>
8     <transmitPowers unit="dB">10.0 10.0 10.0 ...
9     ... 10.0 10.0 10.0</transmitPowers>
10    <systemTemperature unit="degrees" system="Kelvin">297</systemTemperature>
11    <systemLosses unit="dB">-5.3</systemLosses>
12  </antennaArray>
13 </instrument>

```

Listing 1: Phased Array configuration

The azimuthPositions XML field defines the position of each T/R module in the azimuth direction while the azimuthElementLength defines the width of each element.

The various azimuth look directions are defined according to the angular width of each beam (which depends upon the length of the subaperture) and the span of angles required to achieve a particular azimuth resolution. In this simulation all beams are created with the same angular width. As well, the subaperture phase-centre positions are generated to be evenly spaced in the azimuth direction.

As illustrated in Figure 21, the simulation generates a data array for each subaperture/beam combination. The parameters for each subaperture/beam combination are also read from the configuration file as illustrated in Listing 2. For each of these combinations, the configuration file defines an XML element called radarConfiguration which has a channel attribute given by “channel $m-n$ ”, where m corresponds to the subaperture while n corresponds to the beam. The subaperture is defined using magnitude weights for each phased-array element on both transmit and receive. The set of wieghts used on transmit may be different from those used on receive.

The beam directions are controlled by using true time-delays on both transmit and receive

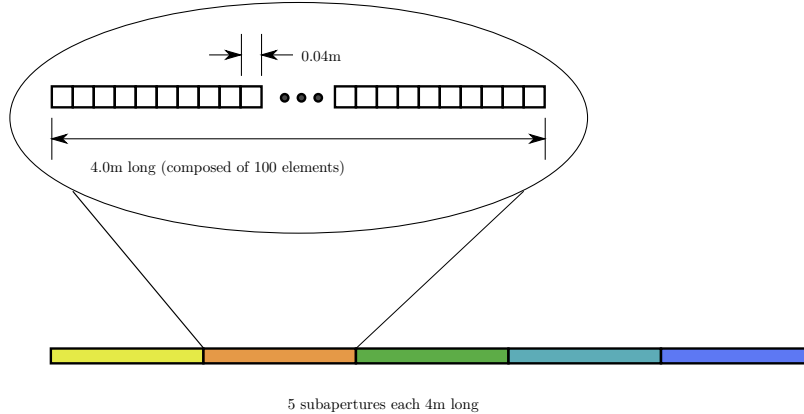


Figure 21: Schematic of 5 subapertures for the 40 cm mode.

(although they are set to the same values in this simulation so that the transmit and receive beams are pointing in the same direction). Of course, a true time-delay approach rather than a phase-steered approach is required as we are considering a wideband system rather than a narrowband system.

```

1 <radarConfiguration channel="channel0-0">
2   <transmitConfiguration>
3     <polarization>H</polarization>
4     <u0 unit="radians">1.553329e-02</u0>
5     <magnitude unit="natural">0 0 0 ... 1 1 1 ... 0 0 0</magnitude>
6     <truedelay unit="ns">0.517098 0.515026 0.512953 ...</truedelay>
7   </transmitConfiguration>
8   <receiveConfiguration>
9     <polarization>H</polarization>
10    <u0 unit="radians">1.553329e-02</u0>
11    <magnitude unit="natural">1 1 1 ... 0 0 0 ... 0 0 0</magnitude>
12    <truedelay unit="ns">0.517098 0.515026 0.512953 ...</truedelay>
13  </receiveConfiguration>
14 </radarConfiguration>
```

Listing 2: Channel/Beam configuration

A data file for each subaperture/beam combination is created with the data stored in the undersampled azimuth-wavenumber, range-time domain. The number of samples in each of the subaperture/beam combinations is sufficient in the range direction to cover all range-cell migration and sufficient in the azimuth direction to capture all angles covered by every beam. Since the number of beams equals the number of channels, the total number of channels created is $N_c = (M + 1)^2$.

Note that in this simulation, the computed signals have no across-track baseline.

12.2 Multi-channel processing

Multi-channel processing for this simulation occurs in the azimuth-wavenumber, range-time domain. This step computes a processing filter that attempts to create a signal over an azimuth frequency range given by $k_{sp} * (N_c + 4)$; that is, when the average antenna pattern of (105) is applied, there should some wavenumber domain zero-padding applied to the computed signal.

Since the theory shows that the multi-channel processing filter is range independent, only a single processing filter is computed and applied across all ranges. Figure 22 illustrates the multi-channel processed signal. In the figure, one sees that the response in the Doppler domain shows the desired response as a function of k_s , with each local maximum in this region highlighting the response from each sub-beam.

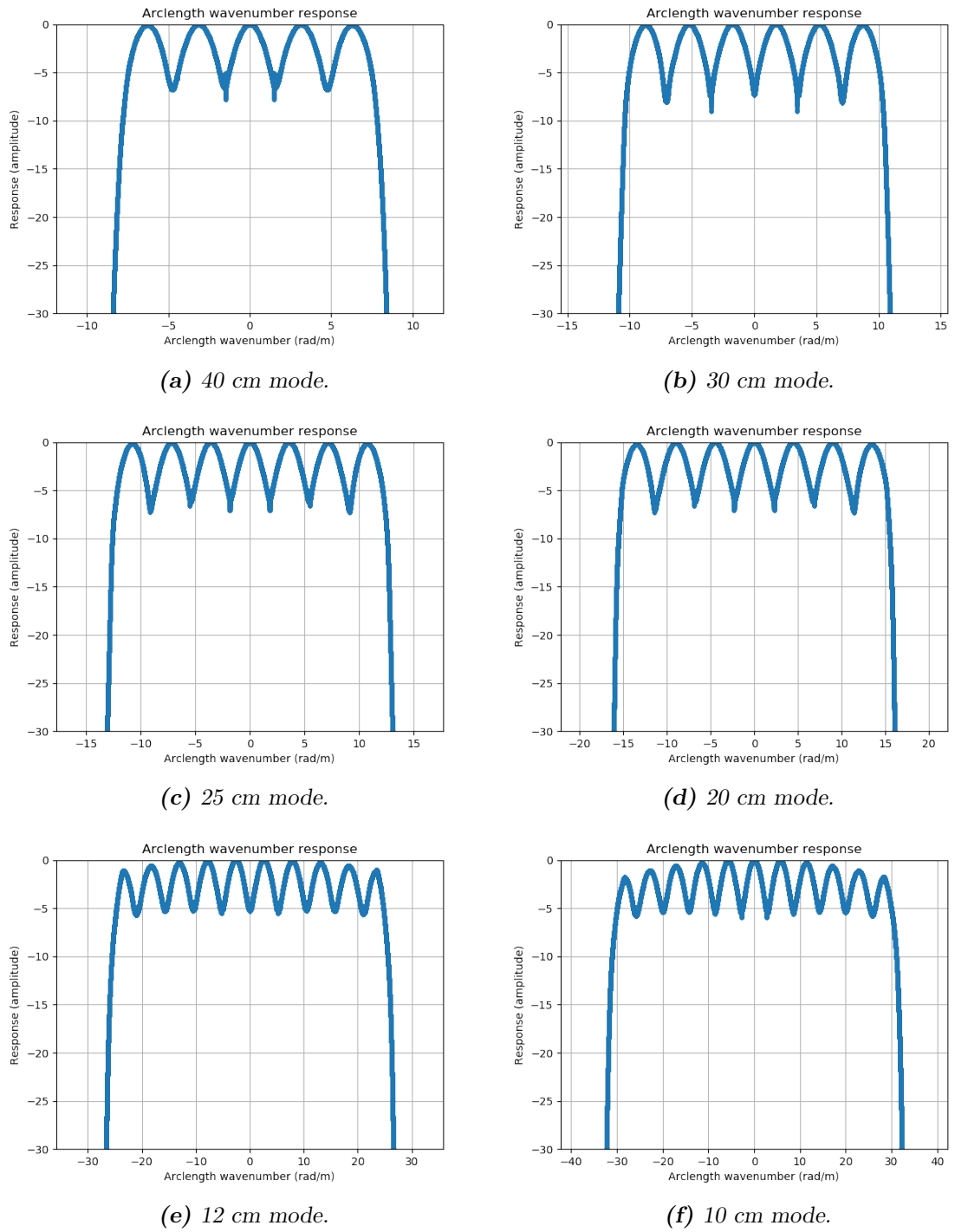


Figure 22: Reconstructed signals in azimuth wavenumber domain.

12.3 Azimuth compression

The simulator then azimuth compresses multi-channel reconstructed signal with the generalized Stoltz interpolation algorithm outlined in Section 9.4. Figure 23 illustrates the produced Point Spread Functions (PSF) for all modes. In these plots, the residual phase correction of Section 8.2 has not been applied.

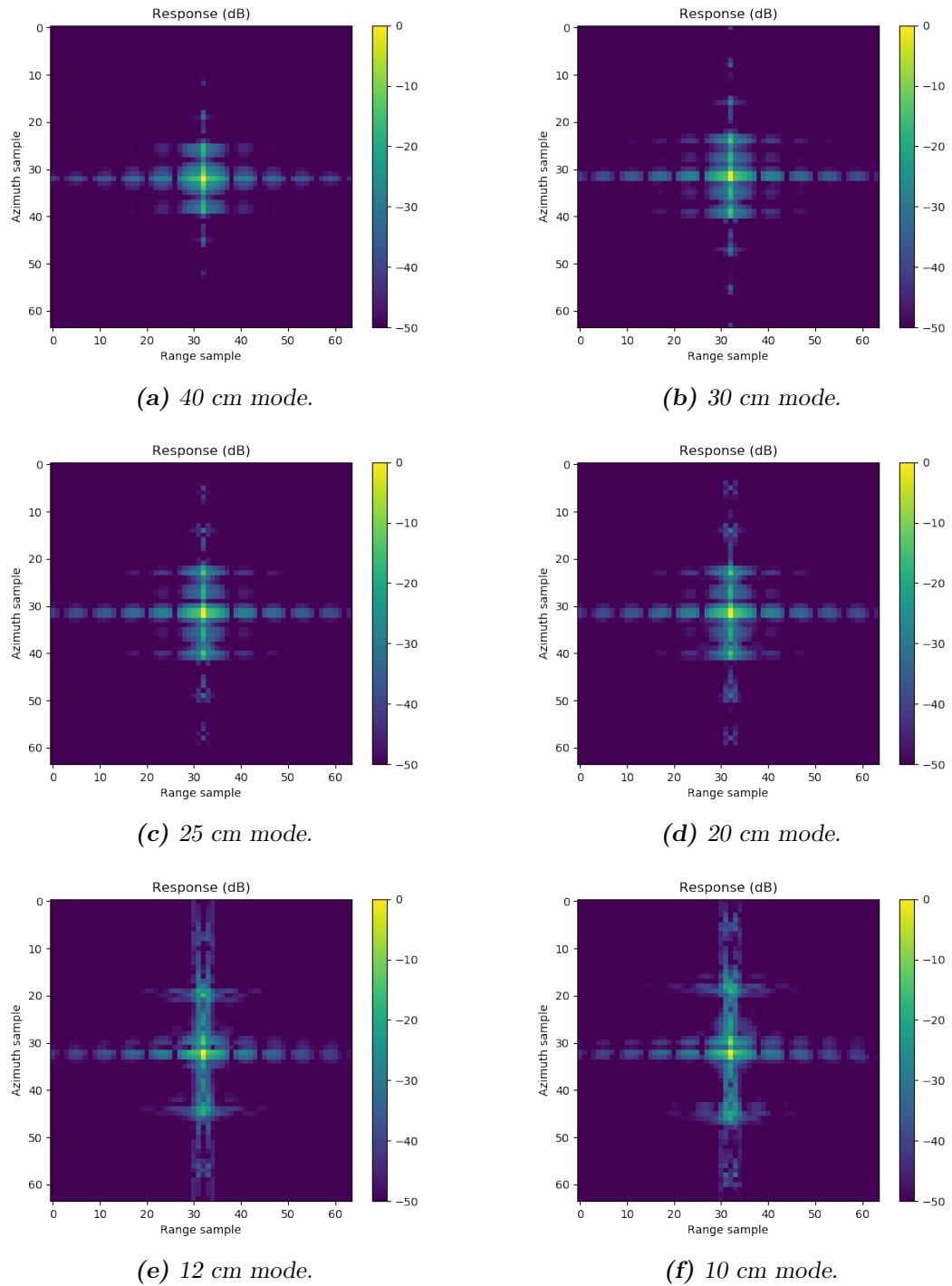


Figure 23: Processed signal Point Spread Response.

12.3.1 Residual phase correction

As the resolution increases, it becomes more important to compensate for the residual phase difference that arises from the discrepancy between the differential geometry approximation to the orbit and the true satellite orbit. If examined closely, Figure 23f shows an azimuth imbalance in the PSF for the 10cm mode (this can also be seen in the 12cm mode and in the 20 cm mode). This imbalance is made clearer in the cross-section plot of Figure 24. After

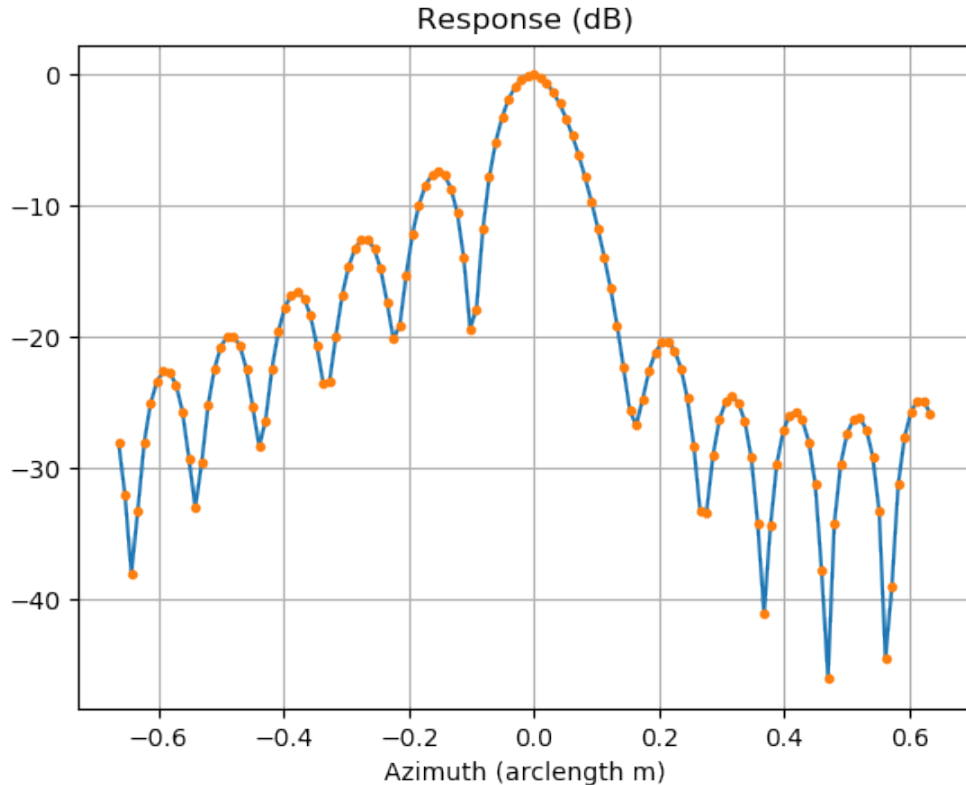


Figure 24: Azimuth cross-section of 10cm mode without residual phase correction.

compensating for the residual phase using the computed phase compensation described in Section 8.2, one obtains the more desirable point spread function illustrated in Figure 25 along with its azimuth cross-section illustrated in Figure 26. The plot clearly illustrates a 3dB resolution of better than 10cm. Further, in the generation of sidelobes at this zoom level, the peak sidelobe level is at around -14.5dB from the peak.

Over the wider range of azimuth values illustrated in Figure 27, one observes a different generation of sidelobes. The peak of these second-level sidelobes manifests at around -18dB. A suitable weighting on the Doppler response of Figure 23f can suppress these second-level

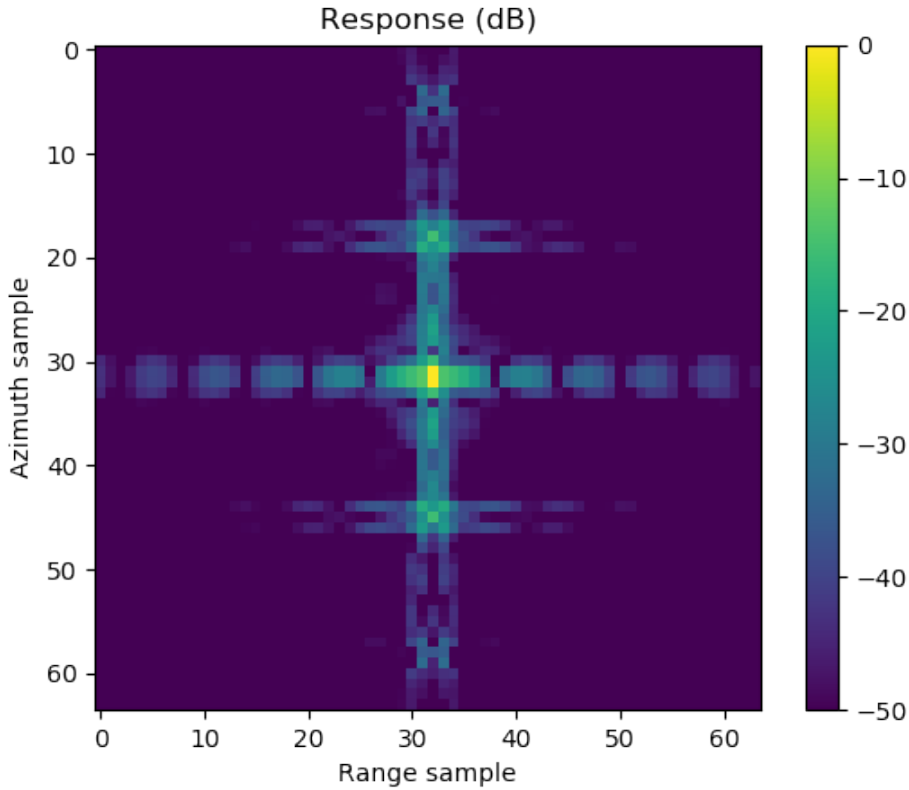


Figure 25: Point Spread Function of 10cm mode after phase compensation.

sidelobes at the expense of resolution.

12.3.2 Signal-to-noise ratio

The PRFs selected for all simulations differ from the “ideal” DPCA PRF thus potentially adversely affecting the SNR. As a measure of the radiometrical resolution, the Noise Equivalent Sigma Zero (NESZ) is computed for all modes. Based upon parameters in the simulation configuration file, the radar equation, [38], is used to generate a estimate of the simulated SNR.

Assuming ideal antenna elements, each with area $D_a D_e$, where D_a and D_e are the azimuth and elevation lengths of the antenna, then the gain of each element as a function of directional cosine u in the azimuth direction and v in the elevation direction may be represented as

$$G_{T_x}(u, v) = G_{R_x}(u, v) = \frac{4\pi D_a D_e}{\lambda_0^2} \text{sinc}^2\left(\frac{uD_a}{\lambda_0}\right) \text{sinc}^2\left(\frac{vD_e}{\lambda_0}\right). \quad (112)$$

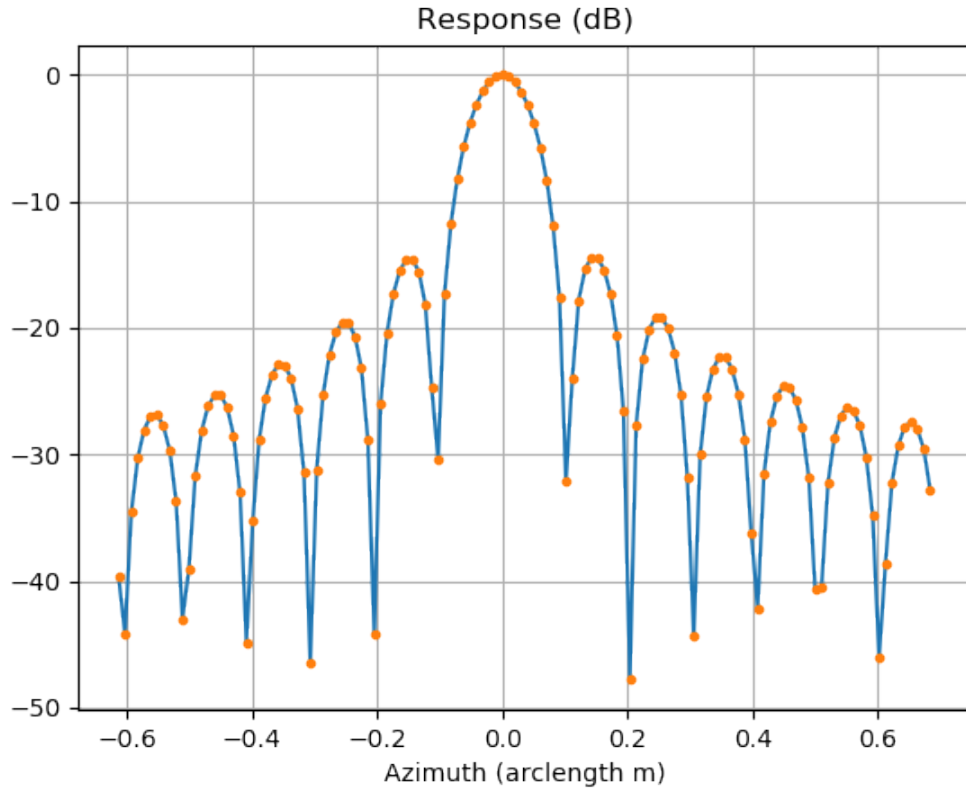


Figure 26: Azimuth cross-section of 10cm mode after residual phase correction.

This expression is such that

$$\int_{-1}^1 G_{T_x}(u, v) du dv = 4\pi, \quad (113)$$

which simply means that power is preserved; however, rather than the power being evenly distributed around a sphere, it is directed, preferentially, in the direction $u = v = 0$.

If P_{T_x} is the transmit power of each transmit element, then the true-time-delay beamforming operation (consisting of N_{T_x} elements) delivers a total of power of $P_{\text{total}} = P_{T_x} N_{T_x}$, and the received SNR can be expressed as

$$\frac{P_{\text{total}} G_{T_x}(u, v) A_{R_x}}{(4\pi R^2)^2 L k_B T B} \sigma_0 \quad (114)$$

where $A_{R_x} = N_{R_x} A_e$ is the effective receive area and $A_e = D_a D_e \alpha$. Also, k_B is Boltzmann's constant. Here, $\alpha < 1$ accounts for the "effective" antenna area of each T/R module. Finally, σ_0 is the backscatter cross-section. If one considers only the maximum gain (i.e.

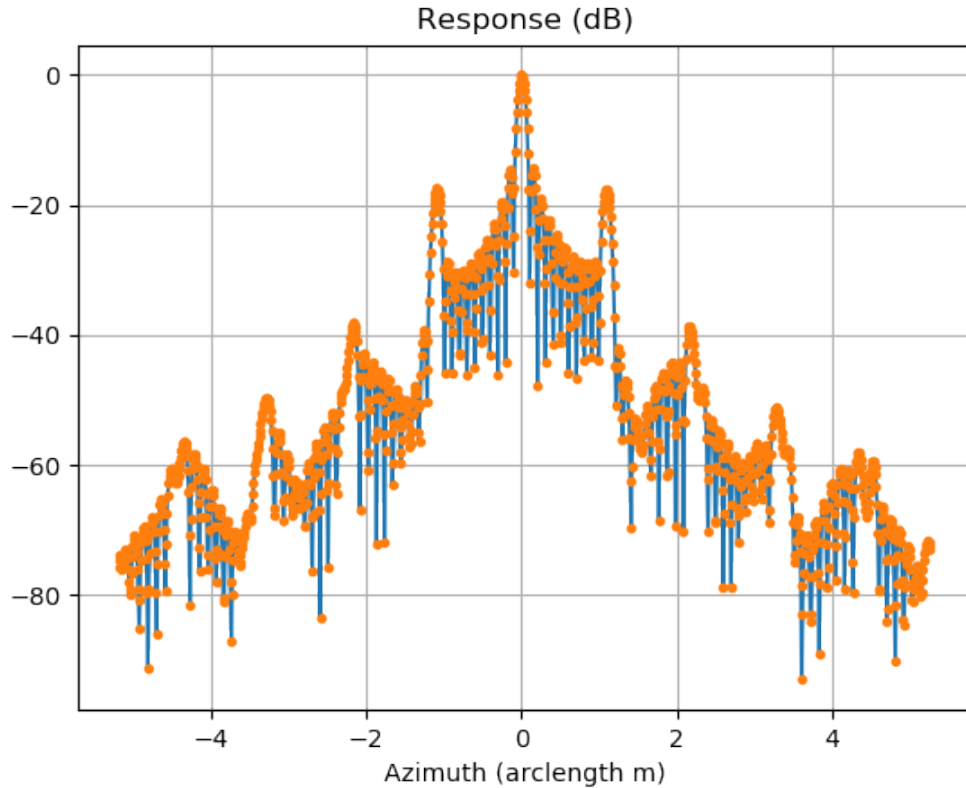


Figure 27: Azimuth cross-section of 10cm mode after residual phase correction.

the maximum of (112)), the above becomes

$$\frac{P_{\text{total}} N_{R_x} A_e}{(4\pi R^2)^2 L k_B T B} \frac{4\pi N_{T_x} A_e}{\lambda_0^2} \sigma_0 \quad (115)$$

where $A_{T_x} = N_{T_x} A_e$ is the effective area of the transmit antenna. The pulse compression gain is approximately $\tau_p B$ (where τ_p is the pulse duration), so, after pulse compression, one computes an SNR of

$$\text{SNR}_s = \frac{P_{\text{total}} N_{R_x} N_{T_x} A_e^2 \tau_p}{4\pi R^4 L k_B T \lambda_0^2} \sigma_0 \quad (116)$$

This is the SNR of each channel before multi-channel and SAR processing. The simulation sets the amplitude of return signal to $\sqrt{\text{SNR}_s}$ with $\sigma_0 = 1$ and generates an additive zero-mean complex circular Gaussian noise signal with unit variance. This noise signal is passed through the multi-channel and SAR processing steps with the same parameters used as for the signal thus simulating the processed noise. The NESZ is computed as the variance of this noise signal divided by the target signal (the maximum of the squared absolute value)

yielding the results in Table 5. For all the modes simulated, the worst-case NESZ is -25 dB while the NESZ for the 10 cm mode is around -30 dB.

Table 5: Computed NESZ

Mode	f_p (Hz)	NESZ (dB)
40 cm	4500.00	-30.9
30 cm	5000.00	-29.8
25 cm	5142.86	-29.7
20 cm	6428.57	-29.2
12 cm	7500.00	-25.5
10 cm	8181.82	-30.2

In summary, the simulation confirms the suitability of the proposed signal processing algorithm and also shows how the generated PSF contains extra sidelobes that most likely result from the different shape of the signal response in the Doppler domain. If these sidelobes are intolerable, they can possibly be removed by modifying the phased-array beam tables; however, this is a topic for further research. The simulation further shows that this approach to SAR imaging generates responses of very high resolution not only geometrically, but also with favourable NESZ characteristics.

13 Conclusion

We propose a system for improved space-based SAR imaging, describing the design, which is based upon a phased-array and an appropriate switching network to allow digitisation of multiple receive channels, the configuration, which imposes a rapid electronic beam switching capability upon the design, and a suitable signal processing algorithm to compute the high resolution imagery. The proposed configuration permits measurement of a relatively large swath in a Stripmap-like mode, thereby offering, theoretically, unlimited azimuth extent. As demonstrated through a simulation of several modes, the geometric resolution of the imagery can be better than the highest resolution spotlight imagery available from current commercial systems while the NESZ is less than -25dB.

Because the approach pushes the limits of space-based SAR resolution, a new wavenumber domain processing approach is developed and presented. The theoretical foundation of this processing method is a major contribution of this document.

Importantly, the state of current technology is sufficiently advanced to construct such a SAR system.

As a final important consideration, we note that the design does not preclude the use of other traditional measurement modes such as Spotlight, TOPS or ScanSAR. Further, it provides the flexibility to implement other advanced modes such as HRWS and Ground Moving Target Indication, [34, 17, 39, 40, 41, 42].

References

- [1] European Space Agency, Copernicus Sentinels POD Data Hub. <https://scihub.copernicus.eu/gnss/#/home>.
- [2] Helmholtz Centre Potsdam, Information System and Data Center for geoscientific data. <http://isdc-old.gfz-potsdam.de/>.
- [3] Bräutigam, B., Rizzoli, P., Gonzalez, C., Weigt, M., Schrank, D., Schulze, D., and Schwerdt, M. (2010), SAR performance monitoring for TerraSAR-X mission, In *Geoscience and Remote Sensing Symposium (IGARSS), 2010 IEEE International*, pp. 3454–3457.
- [4] Fox, P. A., Luscombe, A. P., and Thompson, A. A. (2004), RADARSAT-2 SAR modes development and utilization, *Canadian journal of remote sensing*, 30(3), 258–264.
- [5] Porfilio, M., Serva, S., Fiorentino, C. A. M., and Calabrese, D. (2016), The acquisition modes of COSMO-Skymed di Seconda Generazione: A new combined approach based on SAR and platform agility, In *2016 IEEE International Geoscience and Remote Sensing Symposium (IGARSS)*, pp. 2082–2085.
- [6] Mittermayer, J., Wollstadt, S., Prats-Iraola, P., and Scheiber, R. (2014), The TerraSAR-X Staring Spotlight Mode Concept, *IEEE Transactions on Geoscience and Remote Sensing*, 52(6), 3695–3706.
- [7] Luo, Y., Zhao, B., Han, X., Wang, R., Song, H., and Deng, Y. (2014), A Novel High-Order Range Model and Imaging Approach for High-Resolution LEO SAR, *IEEE Transactions on Geoscience and Remote Sensing*, 52(6), 3473–3485.
- [8] Meng, D., Ding, C., Hu, D., Qiu, X., Huang, L., Han, B., Liu, J., and Xu, N. (2018), On the Processing of Very High Resolution Spaceborne SAR Data: A Chirp-Modulated Back Projection Approach, *IEEE Transactions on Geoscience and Remote Sensing*, 56(1), 191–201.
- [9] Eldhuset, K. (2017), High-Resolution Spaceborne SAR Processing Using the Decomposed Transfer Function, *IEEE Transactions on Aerospace and Electronic Systems*, 53(5), 2187–2198.
- [10] Zhao, B., Qi, X., Song, H., Wang, R., Mo, Y., and Zheng, S. (2014), An Accurate Range Model Based on the Fourth-Order Doppler Parameters for Geosynchronous SAR, *IEEE Geoscience and Remote Sensing Letters*, 11(1), 205–209.
- [11] Wu, Y., Sun, G., Yang, C., Yang, J., Xing, M., and Bao, Z. (2016), Processing of Very High Resolution Spaceborne Sliding Spotlight SAR Data Using Velocity Scaling, *IEEE Transactions on Geoscience and Remote Sensing*, 54(3), 1505–1518.

- [12] Wang, P., Liu, W., Chen, J., Niu, M., and Yang, W. (2015), A High-Order Imaging Algorithm for High-Resolution Spaceborne SAR Based on a Modified Equivalent Squint Range Model, *IEEE Transactions on Geoscience and Remote Sensing*, 53(3), 1225–1235.
- [13] Rodriguez-Cassola, M., Prats-Iraola, P., Krieger, G., and Moreira, A. (2019), On the use of Time-Domain SAR Focusing in Spaceborne SAR Missions, In *IGARSS 2019 - 2019 IEEE International Geoscience and Remote Sensing Symposium*, pp. 755–758.
- [14] Prats-Iraola, P., Scheiber, R., Rodriguez-Cassola, M., Mittermayer, J., Wollstadt, S., De Zan, F., Bräutigam, B., Schwerdt, M., Reigber, A., and Moreira, A. (2014), On the Processing of Very High Resolution Spaceborne SAR Data, *IEEE Transactions on Geoscience and Remote Sensing*, 52(10), 6003–6016.
- [15] Jakowatz, C. V., Wahl, D. E., Eichel, P. H., Ghiglia, D. C., and Thompson, P. A. (1996), Spotlight-Mode Synthetic Aperture Radar: A Signal Processing Approach, Boston: Kluwer Academis Publishers.
- [16] Calabrese, D. (2014), DIscete Stepped Strip (DI2S), In *EUSAR 2014; 10th European Conference on Synthetic Aperture Radar; Proceedings of*, pp. 1–4.
- [17] Sikaneta, I. and Gierull, C. (2015), Phased-Array Beam-Diversity With Multiple Channels for Improved SAR Imaging, *IEEE Journal of Selected Topics in Applied Earth Observations and Remote Sensing*, 8(11), 5106–5115.
- [18] Cumming, I. G. and Wong, F. H. (2005), Digital Processing of Synthetic Aperture Radar Data: Algorithms and Implementation, Norwood, MA: Artech House Remote Sensing Library.
- [19] Gebert, N. (2009), Multi-Channel Azimuth Processing for High-Resolution Wide-Swath SAR Imaging, Ph.D. thesis, University of Karlsruhe.
- [20] Wood, J., Notes on the geometry of curves.
<http://homepages.math.uic.edu/~jwood/analysis/Curvegeomrev.pdf>.
- [21] Shou, H.-N. (2014), Orbit Propagation and Determination of Low Earth Orbit Satellites, *International Journal of Antennas and Propagation*, 2014, 1–12.
- [22] NASA, EGM96, The NASA GSFC and NIMA Joint Geopotential Model.
<https://cddis.nasa.gov/926/egm96/>.
- [23] S., X., Z., Y., and Z., W. (2007), Effective velocity estimation for space-borne SAR based on chirp scaling algorithm, In *2007 1st Asian and Pacific Conference on Synthetic Aperture Radar*, pp. 427–430.
- [24] Wong, F., Tan, N. L., and Yeo, T. S. (2000), Effective velocity estimation for space-borne SAR, In *IGARSS 2000. IEEE 2000 International Geoscience and Remote Sensing Symposium. Taking the Pulse of the Planet: The Role of Remote*

Sensing in Managing the Environment. Proceedings (Cat. No.00CH37120), Vol. 1, pp. 90–92 vol.1.

- [25] Liang, C., Fielding, E. J., and Huang, M.-H. (2017), Estimating Azimuth Offset With Double-Difference Interferometric Phase: The Effect of Azimuth FM Rate Error in Focusing, *IEEE Transactions on Geoscience and Remote Sensing*, 55(12), 7018–7031.
- [26] Prats-Iraola, P., Scheiber, R., Rodriguez-Cassola, M., Mittermayer, J., Wollstadt, S., De Zan, F., Bräutigam, B., Schwerdt, M., Reigber, A., and Moreira, A. (2014), On the Processing of Very High Resolution Spaceborne SAR Data, *IEEE Transactions on Geoscience and Remote Sensing*, 52(10), 6003–6016.
- [27] Cumming, I., Neo, Y., and Wong, F. (2003), Interpretations of the omega-K algorithm and comparisons with other algorithms, In *Geoscience and Remote Sensing Symposium, 2003. IGARSS '03. Proceedings. 2003 IEEE International*, Vol. 3, pp. 1455–1458, Toulouse, France.
- [28] Franceschetti, G. and Lanari, R. (1999), Synthetic Aperture Radar Processing, Washington: CRC Press.
- [29] Raney, R. K. (1992), A New And Fundamental Fourier Transform Pair, In *Geoscience and Remote Sensing Symposium, 1992. IGARSS '92. International*, Vol. 1, pp. 106–107, Houston, TX, USA.
- [30] Bamler, R. (1992), A comparison of range-Doppler and wavenumber domain SAR focusing algorithms, *Geoscience and Remote Sensing, IEEE Transactions on*, 30(4), 706–713.
- [31] Ender, J. H. G. (2003), Signal theoretical aspects of bistatic SAR, In *Geoscience and Remote Sensing Symposium, 2003. IGARSS '03. Proceedings. 2003 IEEE International*, Vol. 3, pp. 1438–1441, Toulouse, France.
- [32] Spiegel, M. R. (1964), Theory and Problems of Complex Variables, New York: Schaums.
- [33] Cafforio, C., Prati, C., and Rocca, F. (1991), SAR data focusing using seismic migration techniques, *Aerospace and Electronic Systems, IEEE Transactions on*, 27(2), 194–207.
- [34] Sikaneta, I., Gierull, C., and Cerutti-Maori, D. (2014), Optimum Signal Processing for Multichannel SAR: With Application to High-Resolution Wide-Swath Imaging, *Geoscience and Remote Sensing, IEEE Transactions on*, 52(10), 6095–6109.
- [35] Sikaneta, I. C. and Cerutti-Maori, D. (2017), Novel Radar Techniques and Applications, Ch. High-resolution wide-swath SAR, Raleigh: SciTech Publishing.
- [36] Krieger, G., Gebert, N., and Moreira, A. (2004), Unambiguous SAR signal reconstruction from nonuniform displaced phase center sampling, *Geoscience and Remote Sensing Letters, IEEE*, 1(4), 260–264.

- [37] Gebert, N. and Krieger, G. (2009), Azimuth Phase Center Adaptation on Transmit for High-Resolution Wide-Swath SAR Imaging, *Geoscience and Remote Sensing Letters, IEEE*, 6(4), 782–786.
- [38] Skolnik, M. (1990), Radar Handbook, McGraw-Hill Professional.
- [39] Sikaneta, I., Cerutti-Maori, D., Klare, J., and Gierull, C. (2014), Comparison of multi-channel high-resolution wide-swath SAR processing methods, In *2014 IEEE Geoscience and Remote Sensing Symposium*, pp. 3834–3837.
- [40] Cerutti-Maori, D., Gierull, C., and Ender, J. (2010), Experimental Verification of SAR-GMTI Improvement Through Antenna Switching, *Geoscience and Remote Sensing, IEEE Transactions on*, 48(4), 2066–2075.
- [41] Gierull, C. H., Sikaneta, I., and Cerutti-Maori, D. (2012), Two-Step Detector for RADARSAT-2's Experimental GMTI Mode, *Geoscience and Remote Sensing, IEEE Transactions on*, PP(99), 1–19.
- [42] Chiu, S. and Sikaneta, I. C. (2004), Applying fractional Fourier transfrom to two-aperture SAR-GMTI, *Proc. 2004 EuSAR conf.*

Annex A Derivative of unit vectors

This section provides a summary of well-known vector derivative relations. These relations can be used to tie together many of the mathematical derivations scattered throughout the document.

Specifically, we present the derivatives of three forms of a parameterized vector with respect to the parameter. These forms include the derivative of the amplitude of the parameterized vector, the derivative of the parameterized unit vector and the derivative of the projection of a given parameterized vector in the direction perpendicular to another vector with the same parameterization. In the following, $\hat{\cdot}$ denotes a unit vector and the dot notation denotes a derivative with respect to t

Consider some vector \mathbf{f}

$$\frac{d|\mathbf{f}|}{dt} = \hat{\mathbf{f}}^T \dot{\mathbf{f}} \quad (\text{A.1})$$

from which one derives

$$\frac{d\hat{\mathbf{f}}}{dt} = \frac{d}{dt} \frac{\mathbf{f}}{|\mathbf{f}|} = \frac{\dot{\mathbf{f}} - \hat{\mathbf{f}}^T \dot{\mathbf{f}} \hat{\mathbf{f}}}{|\mathbf{f}|} = \frac{\dot{\mathbf{f}} - \hat{\mathbf{f}} \hat{\mathbf{f}}^T \dot{\mathbf{f}}}{|\mathbf{f}|} = \frac{\mathbf{P}_f \dot{\mathbf{f}}}{|\mathbf{f}|} \quad (\text{A.2})$$

where

$$\mathbf{P}_f = \mathbf{I} - \hat{\mathbf{f}} \hat{\mathbf{f}}^T \quad (\text{A.3})$$

where \mathbf{I} is the identity matrix. By inspection, one notes that pre-multiplication of a vector by the matrix \mathbf{P}_f always yields the component of that vector that is perpendicular to \mathbf{f} .

By using the above relations, one calculates, for vectors \mathbf{f} and \mathbf{g} , the final relation that

$$\frac{d}{dt} \mathbf{P}_f \mathbf{g} = -\frac{1}{|\mathbf{f}|} [\mathbf{P}_f \dot{\mathbf{f}} \hat{\mathbf{f}}^T + \hat{\mathbf{f}} \hat{\mathbf{f}}^T \mathbf{P}_f] \mathbf{g} + \mathbf{P}_f \dot{\mathbf{g}} \quad (\text{A.4})$$

Annex B ECEF acceleration

This section relates the equations of motion of a satellite in an Earth-Centered, Earth-Fixed (ECEF) coordinate system to those in an Earth-Centered Inertial (ECI) coordinate system. These relations play a role in propagating the orbit of a satellite since the acceleration of the satellite (derived from the egm96 gravitational potential in this document) has nothing to do with the rotation of the planet. On the other hand, SAR imaging of the ground, which rotates underneath the satellite, is most readily described in a coordinate system common both to the ground and the satellite (an ECEF system). This means that we prefer satellite position, velocity, acceleration, and the rate of change of acceleration in an ECEF coordinate system. In essence, the inertial gravitational acceleration needs to be properly interpreted in an ECEF coordinate system. We then propagate the satellite orbit in an ECEF coordinate system.

Define the relation between ECEF space and inertial space as

$$\mathbf{x}_e(t) = \mathbf{M}(t)\mathbf{x}_i(t), \quad (\text{B.1})$$

and

$$\mathbf{x}_i(t) = \mathbf{M}^T(t)\mathbf{x}_e(t), \quad (\text{B.2})$$

where

$$\mathbf{M}(t) = \begin{bmatrix} \cos \omega_e t & -\sin \omega_e t & 0 \\ \sin \omega_e t & \cos \omega_e t & 0 \\ 0 & 0 & 1 \end{bmatrix}, \quad (\text{B.3})$$

where ω_e is the rotation rate of the earth. Calculation of derivatives, up to third order as required to compute the satellite jerk, yields

$$\dot{\mathbf{M}}(t) = \omega_e \begin{bmatrix} -\sin \omega_e t & -\cos \omega_e t & 0 \\ \cos \omega_e t & -\sin \omega_e t & 0 \\ 0 & 0 & 0 \end{bmatrix}, \quad (\text{B.4})$$

$$\ddot{\mathbf{M}}(t) = -\omega_e^2 \begin{bmatrix} \cos \omega_e t & -\sin \omega_e t & 0 \\ \sin \omega_e t & \cos \omega_e t & 0 \\ 0 & 0 & 0 \end{bmatrix}, \quad (\text{B.5})$$

and

$$\dddot{\mathbf{M}}(t) = -\omega_e^3 \begin{bmatrix} -\sin \omega_e t & -\cos \omega_e t & 0 \\ \cos \omega_e t & -\sin \omega_e t & 0 \\ 0 & 0 & 0 \end{bmatrix}. \quad (\text{B.6})$$

To simplify notation, let

$$\mathbf{I}_2 = \begin{bmatrix} 1 & 0 & 0 \\ 0 & 1 & 0 \\ 0 & 0 & 0 \end{bmatrix} \quad (\text{B.7})$$

and

$$\mathbf{Q}_2 = \begin{bmatrix} 0 & -1 & 0 \\ 1 & 0 & 0 \\ 0 & 0 & 0 \end{bmatrix}. \quad (\text{B.8})$$

By direct calculation

$$\mathbf{Q}_2 \mathbf{Q}_2 = -\mathbf{I}_2 \quad (\text{B.9})$$

For use later, we compute the following

$$\dot{\mathbf{M}}(t) \mathbf{M}^T(t) = \omega_e \mathbf{Q}_2 \quad (\text{B.10})$$

$$\ddot{\mathbf{M}}(t) \mathbf{M}^T(t) = -\omega_e^2 \mathbf{I}_2 \quad (\text{B.11})$$

$$\dddot{\mathbf{M}}(t) \mathbf{M}^T(t) = -\omega_e^3 \mathbf{Q}_2 \quad (\text{B.12})$$

$$(\text{B.13})$$

B.1 ECEF equations of motion

With the previous material, one computes

$$\dot{\mathbf{x}}_e(t) = \dot{\mathbf{M}}(t) \mathbf{x}_i(t) + \mathbf{M}(t) \dot{\mathbf{x}}_i(t) \quad (\text{B.14})$$

$$\ddot{\mathbf{x}}_e(t) = \ddot{\mathbf{M}}(t) \mathbf{x}_i(t) + 2\dot{\mathbf{M}}(t) \dot{\mathbf{x}}_i(t) + \mathbf{M}(t) \ddot{\mathbf{x}}_i(t) \quad (\text{B.15})$$

$$\ddot{\mathbf{x}}_e(t) = \ddot{\mathbf{M}}(t) \mathbf{x}_i(t) + 3\dot{\mathbf{M}}(t) \dot{\mathbf{x}}_i(t) + 3\dot{\mathbf{M}}(t) \ddot{\mathbf{x}}_i(t) + \mathbf{M}(t) \ddot{\mathbf{x}}_i(t) \quad (\text{B.16})$$

From the first expression

$$\begin{aligned} \mathbf{M}^T(t) \dot{\mathbf{x}}_e(t) &= \mathbf{M}^T(t) \dot{\mathbf{M}}(t) \mathbf{M}^T(t) \mathbf{x}_e(t) + \dot{\mathbf{x}}_i(t) \\ &= \omega_e \mathbf{M}^T(t) \mathbf{Q}_2 \mathbf{x}_e(t) + \dot{\mathbf{x}}_i(t) \end{aligned} \quad (\text{B.17})$$

so that

$$\dot{\mathbf{x}}_i(t) = \mathbf{M}^T(t) [\dot{\mathbf{x}}_e(t) - \omega_e \mathbf{Q}_2 \mathbf{x}_e(t)] \quad (\text{B.18})$$

Substitution of this equivalence into the second expression above yields

$$\begin{aligned} \ddot{\mathbf{x}}_e(t) &= \ddot{\mathbf{M}}(t) \mathbf{M}^T(t) \mathbf{x}_e(t) + 2\dot{\mathbf{M}}(t) \mathbf{M}^T(t) [\dot{\mathbf{x}}_e(t) - \omega_e \mathbf{Q}_2 \mathbf{x}_e(t)] + \mathbf{M}(t) \ddot{\mathbf{x}}_i(t) \\ &= -\omega_e^2 \mathbf{I}_2 \mathbf{x}_e(t) + 2\omega_e \mathbf{Q}_2 [\dot{\mathbf{x}}_e(t) - \omega_e \mathbf{Q}_2 \mathbf{x}_e(t)] + \mathbf{M}(t) \ddot{\mathbf{x}}_i(t) \\ &= -\omega_e^2 \mathbf{I}_2 \mathbf{x}_e(t) + 2\omega_e \mathbf{Q}_2 \dot{\mathbf{x}}_e(t) + 2\omega_e^2 \mathbf{I}_2 \mathbf{x}_e(t) + \mathbf{M}(t) \ddot{\mathbf{x}}_i(t) \\ &= \omega_e^2 \mathbf{I}_2 \mathbf{x}_e(t) + 2\omega_e \mathbf{Q}_2 \dot{\mathbf{x}}_e(t) + \mathbf{M}(t) \ddot{\mathbf{x}}_i(t) \end{aligned} \quad (\text{B.19})$$

and substitution into the third expression yields

$$\begin{aligned} \ddot{\mathbf{x}}_e(t) &= \ddot{\mathbf{M}}(t) \mathbf{M}^T(t) \mathbf{x}_e(t) + 3\dot{\mathbf{M}}(t) \mathbf{M}^T(t) [\dot{\mathbf{x}}_e(t) - \omega_e \mathbf{Q}_2 \mathbf{x}_e(t)] \\ &\quad + 3\dot{\mathbf{M}}(t) \ddot{\mathbf{x}}_i(t) + \mathbf{M}(t) \ddot{\mathbf{x}}_i(t) \\ &= -\omega_e^3 \mathbf{Q}_2 \mathbf{x}_e(t) - 3\omega_e^2 \mathbf{I}_2 [\dot{\mathbf{x}}_e(t) - \omega_e \mathbf{Q}_2 \mathbf{x}_e(t)] + 3\dot{\mathbf{M}}(t) \ddot{\mathbf{x}}_i(t) + \mathbf{M}(t) \ddot{\mathbf{x}}_i(t) \\ &= 2\omega_e^3 \mathbf{Q}_2 \mathbf{x}_e(t) - 3\omega_e^2 \mathbf{I}_2 \dot{\mathbf{x}}_e(t) + 3\dot{\mathbf{M}}(t) \ddot{\mathbf{x}}_i(t) + \mathbf{M}(t) \ddot{\mathbf{x}}_i(t) \end{aligned} \quad (\text{B.20})$$

B.2 Rate of change of acceleration

This subsection computes the rate of change of acceleration of a satellite in an inertial Earth-Centered coordinate system. Further, because the egm96 gravitational potential, (31), is defined using spherical-polar coordinates, this subsection also demonstrates how to convert the gradient of this potential into a Cartesian representation. The ECEF rate of change of acceleration is then given by the derivative of this acceleration with respect to time and one then acquires the ECEF equations of motion by substituting the two computed quantities into (B.19) and (B.20).

The gravitational potential, $U(r, \phi, \lambda)$, is defined in (31), and the gradient of this quantity defines the gravitational acceleration. We convert the gradient in spherical-polar coordinates to a gradient in Cartesian coordinates, x, y, z , through

$$\ddot{\mathbf{x}}_i(t) = \vec{\nabla}_{x,y,z} U = \begin{bmatrix} \frac{\partial r}{\partial x} & \frac{\partial \phi}{\partial x} & \frac{\partial \lambda}{\partial x} \\ \frac{\partial r}{\partial y} & \frac{\partial \phi}{\partial y} & \frac{\partial \lambda}{\partial y} \\ \frac{\partial r}{\partial z} & \frac{\partial \phi}{\partial z} & \frac{\partial \lambda}{\partial z} \end{bmatrix} \begin{bmatrix} \frac{\partial U}{\partial r} \\ \frac{\partial U}{\partial \phi} \\ \frac{\partial U}{\partial \lambda} \end{bmatrix} = \left[\frac{\partial(r, \phi, \lambda)}{\partial(x, y, z)} \right]^T \vec{\nabla}_{r, \phi, \lambda} U. \quad (\text{B.21})$$

Note that, although the above equation does explicitly show a time dependence on the left side, the time variable has been suppressed on the right to allow for more compact notation. In actual fact, the position coordinates do depend on time. More explicitly, the position of a body is given by $x(t), y(t), z(t)$. Thus, to compute the derivative of the acceleration, one must compute

$$\ddot{\mathbf{x}}_i(t) = \frac{d\vec{\nabla}_{x,y,z} U}{dt} = \begin{bmatrix} \frac{\partial^2 U}{\partial x^2} & \frac{\partial^2 U}{\partial y \partial x} & \frac{\partial^2 U}{\partial z \partial x} \\ \frac{\partial^2 U}{\partial x \partial y} & \frac{\partial^2 U}{\partial y^2} & \frac{\partial^2 U}{\partial z \partial y} \\ \frac{\partial^2 U}{\partial x \partial z} & \frac{\partial^2 U}{\partial y \partial z} & \frac{\partial^2 U}{\partial z^2} \end{bmatrix} \begin{bmatrix} \frac{dx}{dt} \\ \frac{dy}{dt} \\ \frac{dz}{dt} \end{bmatrix} \quad (\text{B.22})$$

A representative component of the matrix in the above may be written as

$$\begin{aligned} \frac{\partial^2 U}{\partial x_i \partial x_j} &= \frac{\partial \frac{\partial U}{\partial x_j}}{\partial x_i} \\ &= \frac{\partial}{\partial x_i} \left[\frac{\partial r}{\partial x_j} \quad \frac{\partial \phi}{\partial x_j} \quad \frac{\partial \lambda}{\partial x_j} \right] \begin{bmatrix} \frac{\partial U}{\partial r} \\ \frac{\partial U}{\partial \phi} \\ \frac{\partial U}{\partial \lambda} \end{bmatrix} \\ &= \left[\frac{\partial^2 r}{\partial x_i \partial x_j} \quad \frac{\partial^2 \phi}{\partial x_i \partial x_j} \quad \frac{\partial^2 \lambda}{\partial x_i \partial x_j} \right] \begin{bmatrix} \frac{\partial U}{\partial r} \\ \frac{\partial U}{\partial \phi} \\ \frac{\partial U}{\partial \lambda} \end{bmatrix} + \left[\frac{\partial r}{\partial x_j} \quad \frac{\partial \phi}{\partial x_j} \quad \frac{\partial \lambda}{\partial x_j} \right] \begin{bmatrix} \frac{\partial^2 U}{\partial x_i \partial r} \\ \frac{\partial^2 U}{\partial x_i \partial \phi} \\ \frac{\partial^2 U}{\partial x_i \partial \lambda} \end{bmatrix} \\ &= \left[\frac{\partial U}{\partial r} \quad \frac{\partial U}{\partial \phi} \quad \frac{\partial U}{\partial \lambda} \right] \begin{bmatrix} \frac{\partial^2 r}{\partial x_i \partial x_j} \\ \frac{\partial^2 \phi}{\partial x_i \partial x_j} \\ \frac{\partial^2 \lambda}{\partial x_i \partial x_j} \end{bmatrix} + \left[\frac{\partial r}{\partial x_j} \quad \frac{\partial \phi}{\partial x_j} \quad \frac{\partial \lambda}{\partial x_j} \right] \begin{bmatrix} \frac{\partial^2 U}{\partial r^2} & \frac{\partial^2 U}{\partial \phi \partial r} & \frac{\partial^2 U}{\partial \lambda \partial r} \\ \frac{\partial^2 U}{\partial r \partial \phi} & \frac{\partial^2 U}{\partial \phi^2} & \frac{\partial^2 U}{\partial \lambda \partial \phi} \\ \frac{\partial^2 U}{\partial r \partial \lambda} & \frac{\partial^2 U}{\partial \phi \partial \lambda} & \frac{\partial^2 U}{\partial \lambda^2} \end{bmatrix} \begin{bmatrix} \frac{\partial r}{\partial x_i} \\ \frac{\partial \phi}{\partial x_i} \\ \frac{\partial \lambda}{\partial x_i} \end{bmatrix} \end{aligned} \quad (\text{B.23})$$

One can consolidate all the terms into matrix form via

$$\ddot{\mathbf{x}}_i(t) = \frac{d\vec{\nabla}_{x,y,z} U}{dt} =$$

$$\begin{bmatrix} \frac{\partial U}{\partial r} & \frac{\partial U}{\partial \phi} & \frac{\partial U}{\partial \lambda} & 0 & 0 & 0 & 0 & 0 & 0 \\ 0 & 0 & 0 & \frac{\partial U}{\partial r} & \frac{\partial U}{\partial \phi} & \frac{\partial U}{\partial \lambda} & 0 & 0 & 0 \\ 0 & 0 & 0 & 0 & 0 & 0 & \frac{\partial U}{\partial r} & \frac{\partial U}{\partial \phi} & \frac{\partial U}{\partial \lambda} \end{bmatrix} \begin{bmatrix} \frac{\partial^2 r}{\partial x \partial x} & \frac{\partial^2 r}{\partial x \partial y} & \frac{\partial^2 r}{\partial x \partial z} \\ \frac{\partial^2 \phi}{\partial x \partial x} & \frac{\partial^2 \phi}{\partial x \partial y} & \frac{\partial^2 \phi}{\partial x \partial z} \\ \frac{\partial^2 \lambda}{\partial x \partial x} & \frac{\partial^2 \lambda}{\partial x \partial y} & \frac{\partial^2 \lambda}{\partial x \partial z} \\ \frac{\partial^2 r}{\partial y \partial x} & \frac{\partial^2 r}{\partial y \partial y} & \frac{\partial^2 r}{\partial y \partial z} \\ \frac{\partial^2 \phi}{\partial y \partial x} & \frac{\partial^2 \phi}{\partial y \partial y} & \frac{\partial^2 \phi}{\partial y \partial z} \\ \frac{\partial^2 \lambda}{\partial y \partial x} & \frac{\partial^2 \lambda}{\partial y \partial y} & \frac{\partial^2 \lambda}{\partial y \partial z} \\ \frac{\partial^2 r}{\partial z \partial x} & \frac{\partial^2 r}{\partial z \partial y} & \frac{\partial^2 r}{\partial z \partial z} \\ \frac{\partial^2 \phi}{\partial z \partial x} & \frac{\partial^2 \phi}{\partial z \partial y} & \frac{\partial^2 \phi}{\partial z \partial z} \\ \frac{\partial^2 \lambda}{\partial z \partial x} & \frac{\partial^2 \lambda}{\partial z \partial y} & \frac{\partial^2 \lambda}{\partial z \partial z} \end{bmatrix} \begin{bmatrix} \frac{dx}{dt} \\ \frac{dy}{dt} \\ \frac{dz}{dt} \end{bmatrix} \quad (B.24)$$

$$+ \begin{bmatrix} \frac{\partial r}{\partial x} & \frac{\partial \phi}{\partial x} & \frac{\partial \lambda}{\partial x} \\ \frac{\partial r}{\partial y} & \frac{\partial \phi}{\partial y} & \frac{\partial \lambda}{\partial y} \\ \frac{\partial r}{\partial z} & \frac{\partial \phi}{\partial z} & \frac{\partial \lambda}{\partial z} \end{bmatrix} \begin{bmatrix} \frac{\partial^2 U}{\partial r^2} & \frac{\partial^2 U}{\partial \phi \partial r} & \frac{\partial^2 U}{\partial \lambda \partial r} \\ \frac{\partial^2 U}{\partial r \partial \phi} & \frac{\partial^2 U}{\partial \phi^2} & \frac{\partial^2 U}{\partial \lambda \partial \phi} \\ \frac{\partial^2 U}{\partial r \partial \lambda} & \frac{\partial^2 U}{\partial \phi \partial \lambda} & \frac{\partial^2 U}{\partial \lambda^2} \end{bmatrix} \begin{bmatrix} \frac{\partial r}{\partial x} & \frac{\partial r}{\partial y} & \frac{\partial r}{\partial z} \\ \frac{\partial \phi}{\partial x} & \frac{\partial \phi}{\partial y} & \frac{\partial \phi}{\partial z} \\ \frac{\partial \lambda}{\partial x} & \frac{\partial \lambda}{\partial y} & \frac{\partial \lambda}{\partial z} \end{bmatrix} \begin{bmatrix} \frac{dx}{dt} \\ \frac{dy}{dt} \\ \frac{dz}{dt} \end{bmatrix}$$

Annex C Derivation of the arclength-parameterized range function

The range between the satellite and a target plays a critical role in SAR processing. This section presents an arclength parameterized expression for this range function. The final approximation of the section, (C.14), yields a version of the function that only weakly depends on the expansion point used to describe the satellite orbit.

For every scatterer at point \mathbf{x} , there is an arclength value, $s_{\mathbf{x}}$, such that $\mathbf{c}_p(s_{\mathbf{x}}) - \mathbf{x}$ is perpendicular to $\mathbf{c}'_p(s_{\mathbf{x}})$. Further, \mathbf{x} can be completely determined by

$$\mathbf{x} = \mathbf{c}_p(s_{\mathbf{x}}) + r \cos \phi \mathbf{N}(s_{\mathbf{x}}) + r \sin \phi \mathbf{B}(s_{\mathbf{x}}), \quad (\text{C.1})$$

where $r = |\mathbf{c}_p(s_{\mathbf{x}}) - \mathbf{x}|$ and $r \cos \phi = [\mathbf{x} - \mathbf{c}_p(s_{\mathbf{x}})] \cdot \mathbf{N}(s_{\mathbf{x}})$.

One computes that

$$\begin{aligned} \mathbf{c}_p(s) - \mathbf{x} &= \mathbf{c}_p(s) - \mathbf{c}_p(s_{\mathbf{x}}) - r \cos \phi \mathbf{N}(s_{\mathbf{x}}) - r \sin \phi \mathbf{B}(s_{\mathbf{x}}) \\ &= (s - s_{\mathbf{x}}) \mathbf{T}_0 + \frac{(s - s_0)^2 - (s_{\mathbf{x}} - s_0)^2}{2} \kappa_0 \mathbf{N}_0 \\ &\quad + \frac{(s - s_0)^3 - (s_{\mathbf{x}} - s_0)^3}{6} [-\kappa_0^2 \mathbf{T}_0 + \kappa'_0 \mathbf{N}_0 + \kappa_0 \tau_0 \mathbf{B}_0] \\ &\quad - r \cos \phi \mathbf{N}(s_{\mathbf{x}}) - r \sin \phi \mathbf{B}(s_{\mathbf{x}}) \\ &= (a - b) \left[\mathbf{T}_0 + \frac{a + b}{2} \kappa_0 \mathbf{N}_0 + \frac{a^2 + ab + b^2}{6} [-\kappa_0^2 \mathbf{T}_0 + \kappa'_0 \mathbf{N}_0 + \kappa_0 \tau_0 \mathbf{B}_0] \right] \\ &\quad - r \cos \phi \mathbf{N}(s_{\mathbf{x}}) - r \sin \phi \mathbf{B}(s_{\mathbf{x}}) \end{aligned}, \quad (\text{C.2})$$

where

$$a = (s - s_0) \quad (\text{C.3})$$

$$b = (s_{\mathbf{x}} - s_0) \quad (\text{C.4})$$

More succinctly, one can write

$$\mathbf{c}_p(s) - \mathbf{x} = (a - b)(\alpha_T \mathbf{T}_0 + \alpha_N \mathbf{N}_0 + \alpha_B \mathbf{B}_0) - r \cos \phi \mathbf{N}(s_{\mathbf{x}}) - r \sin \phi \mathbf{B}(s_{\mathbf{x}}) \quad (\text{C.5})$$

where

$$\alpha_T = 1 - \kappa_0^2 \frac{a^2 + ab + b^2}{6} \quad (\text{C.6})$$

$$\alpha_N = \kappa_0 \frac{a + b}{2} + \kappa'_0 \frac{a^2 + ab + b^2}{6} \quad (\text{C.7})$$

$$\alpha_B = \kappa_0 \tau_0 \frac{a^2 + ab + b^2}{6} \quad (\text{C.8})$$

From the Frenet-Serret equations, (19), one can make the approximation that

$$r \cos \phi \mathbf{N}(s_x) \approx r \cos \phi \mathbf{N}_0 + (s_x - s_0) r \cos \phi (-\kappa_0 \mathbf{T}_0 + \tau_0 \mathbf{B}_0) \quad (\text{C.9})$$

$$r \sin \phi \mathbf{B}(s_x) \approx r \sin \phi \mathbf{B}_0 - (s_x - s_0) r \sin \phi \tau_0 \mathbf{N}_0 \quad (\text{C.10})$$

and since $s_x - s_0 = b$, the range expression can be written as

$$\begin{aligned} \mathbf{c}_p(s) - \mathbf{x} &= [(a - b)\alpha_T + br\kappa_0 \cos \phi] \mathbf{T}_0 \\ &\quad + [(a - b)\alpha_N - r \cos \phi + br\tau_0 \sin \phi] \mathbf{N}_0 \\ &\quad + [(a - b)\alpha_B - r \sin \phi - br\tau_0 \cos \phi] \mathbf{B}_0 \end{aligned} \quad (\text{C.11})$$

The computation of square of the above expression yields a polynomial in $(a - b) = (s - s_x)$ (after using sageMath),

$$|\mathbf{c}_p(s) - \mathbf{x}|^2 = \sum_{k=0}^5 a_k (s - s_x)^k \quad (\text{C.12})$$

with the following coefficients

$$\begin{aligned} a_0 &= b^2 \kappa_0^2 r^2 \cos^2 \phi + b^2 r^2 \tau_0^2 + r^2 \\ a_1 &= \frac{2b^2 \tau_0 r}{3} (b\kappa'_0 + 2\kappa_0) \sin \phi - \frac{2b^2 r}{3} (b\kappa_0 \tau_0^2 + b\kappa_0^3 + \kappa'_0) \cos \phi \\ a_2 &= 1 - [\kappa_0 + b\kappa'_0 + b^2(\kappa_0^3 + \kappa_0 \tau_0^2)] r \cos \phi + b^2 \kappa'_0 \tau_0 r \sin \phi \\ &\quad + \frac{b^4}{9} (\kappa_0^4 + \kappa_0^2 \tau_0^2 + \kappa'_0^2) + \frac{b^2 \kappa_0}{3} (\kappa_0 + 2b\kappa'_0) \\ a_3 &= -\frac{r}{3} (\kappa_0 \tau_0 \sin \phi + \kappa'_0 \cos \phi) + \frac{b^3}{3} (\kappa_0^4 + \kappa_0^2 \tau_0^2 + \kappa'_0^2) + \frac{4b^2}{3} \kappa_0 \kappa'_0 \\ &\quad + \frac{br}{3} [\kappa'_0 \tau_0 \sin \phi - (\kappa_0 \tau_0^2 + \kappa_0^3) \cos \phi] \\ a_4 &= -\frac{\kappa_0^2}{12} + \frac{13b^2}{36} (\kappa_0^4 + \kappa_0^2 \tau_0^2 + \kappa'_0^2) + \frac{5b\kappa_0 \kappa'_0}{6} \\ a_5 &= \frac{b}{6} (\kappa_0^4 + \kappa_0^2 \tau_0^2 + \kappa'_0^2 + \kappa \kappa'_0) \\ a_6 &= \frac{1}{36} (\kappa_0^4 + \kappa_0^2 \tau_0^2 + \kappa'_0^2) \end{aligned} \quad (\text{C.13})$$

In the region of the chosen point of expansion, s_0, b evaluates to a relatively small number, thus, one can make the approximation that

$$\begin{aligned} a_0 &= r^2 \\ a_1 &= 0 \\ a_2 &= 1 - \kappa_0 r \cos \phi \\ a_3 &= -\frac{r}{3} (\kappa_0 \tau_0 \sin \phi + \kappa'_0 \cos \phi) \\ a_4 &= -\frac{\kappa_0^2}{12} \\ a_5 &= 0 \\ a_6 &= 0 \end{aligned} \quad (\text{C.14})$$

Annex D Iteration to the stationary point

This section illustrates convergence of the procedure of (75). Recall that the requirement is to compute s from

$$x = sg(s), \quad (\text{D.1})$$

and to invert the above, we suggested that

$$\begin{aligned} s &= \frac{x}{g(s)} = \frac{x}{g\left(\frac{x}{g(s)}\right)} = \frac{x}{g\left(\frac{x}{g\left(\frac{x}{g(s)}\right)}\right)} = \dots \\ g(s) &= g\left(\frac{x}{g(s)}\right) = g\left(\frac{x}{g\left(\frac{x}{g(s)}\right)}\right) = \dots \end{aligned} \quad (\text{D.2})$$

Re-write the expression to invert as

$$\frac{x}{g(s)} - s = 0 \quad (\text{D.3})$$

and define the two functions

$$f_1(s) = s, \quad (\text{D.4})$$

$$f_2(s) = \frac{x}{g(s)}. \quad (\text{D.5})$$

The task is then to compute the point where these two functions intersect. From Figure

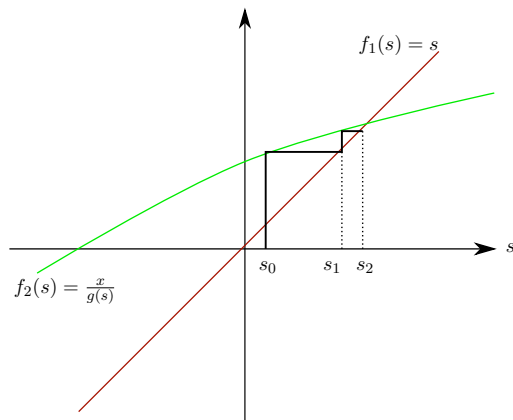


Figure D.1: Simple iterative procedure showing convergence to the stationary point

D.1, one sees that, starting from the point s_0

$$s_1 = f_2(s_0) = \frac{x}{g(s_0)}, \quad (\text{D.6})$$

and, in general

$$s_{n+1} = f_2(s_n) = \frac{x}{g(s_n)}. \quad (\text{D.7})$$

If

$$\left| \frac{df_2(s)}{ds} \right| < 1, \quad (\text{D.8})$$

then convergence is assured.

Annex E Numerical implementation of the Stoltz interpolation

This section outlines an approach to support numerical implementation of the proposed, generalized Stoltz interpolation. Because the generalized Stoltz interpolation points do not have a closed form as they do in, for instance, [18, 30], this section presents a numerical approach. There is nothing particularly insightful about the proposed algorithm; in fact, this section aims to present an approach that avoids confusion and facilitates numerical implementation.

So, to begin, recall that

$$x = -r \tan \theta_s, \quad (\text{E.1})$$

so that

$$\sin \theta_s = -\frac{x}{\sqrt{r^2 + x^2}} \quad (\text{E.2})$$

$$\cos \theta_s = \frac{r}{\sqrt{r^2 + x^2}}. \quad (\text{E.3})$$

Also recall that

$$-\frac{x}{\sqrt{r^2 + x^2}} \left[g(s) + \frac{a_3 x}{2g^2(s)} + \frac{a_4 x^2}{g^3(s)} \right] = \frac{k_s}{k_r}. \quad (\text{E.4})$$

From (80), when one makes the (Stoltz interpolation) change of variables,

$$k_{r_s} = k_r \sec \theta_s - k_s \frac{\tan \theta_s}{g(s)}, \quad (\text{E.5})$$

which leads to the relation that

$$k_r = \frac{r k_{r_s}}{\sqrt{r^2 + x^2}} - \frac{k_s x}{g(s) \sqrt{r^2 + x^2}}. \quad (\text{E.6})$$

E.1 Simplification for iterative root-finding

In the opinion of the authors, implementation of the Stoltz interpolation (into computer code) benefits from defining the following function

$$\psi(x; l, m, n) = \frac{x^l}{(r^2 + x^2)^m g^n(s)} \quad (\text{E.7})$$

The Newton iterative root finding method requires computation of the derivative of the above function, which, in turn, requires caculation of the derivative of $g(s)$ with respect to

x . Specifically,

$$\begin{aligned}\frac{dg(s)}{dx} &= \frac{dg(s)}{ds} \frac{ds}{dx} \\ &= \frac{a_3 + 2a_4 s}{2g(s)} \frac{ds}{dx} \\ &= \left(\frac{a_3}{2g(s)} + \frac{a_4 x}{g^2(s)} \right) \frac{ds}{dx}\end{aligned}\quad (\text{E.8})$$

Because $x = sg(s)$, one derives

$$\begin{aligned}1 &= \frac{ds}{dx} g(s) + s \frac{dg(s)}{ds} \frac{ds}{dx} \\ &= \frac{ds}{dx} \left[g(s) + s \frac{a_3 + 2a_4 s}{2g(s)} \right] \\ &= \frac{ds}{dx} \left[g(s) + \frac{x}{g(s)} \left(\frac{a_3}{2g(s)} + \frac{a_4 x}{g^2(s)} \right) \right]\end{aligned}\quad (\text{E.9})$$

By substituting (E.9) into (E.8), one arrives at

$$\frac{dg(s)}{dx} = \frac{a_3 g^2(s) + 2a_4 x g(s)}{2g^4(s) + a_3 x g(s) + 2a_4 x^2} \quad (\text{E.10})$$

The derivative of $\psi(x; l, m, n)$ is thus given by¹¹,

$$\begin{aligned}\frac{d\psi(x; l, m, n)}{dx} &= \psi(x; l - 1, m, n) \\ &\quad \left(l - m \frac{2x^2}{r^2 + x^2} - n \frac{a_3 x g(s) + 2a_4 x^2}{2g^4(s) + a_3 x g(s) + 2a_4 x^2} \right)\end{aligned}\quad (\text{E.11})$$

With the aforementioned definition,

$$k_r = rk_{rs}\psi(x; 0, 1/2, 0) - k_s\psi(x; 1, 1/2, 1), \quad (\text{E.12})$$

and, when this is substituted into (78), along with the relations in (E.2) and (E.3), one obtains

$$\begin{aligned}rk_{rs}\psi(x; 1, 1, -1) - k_s\psi(x; 2, 1, 0) + \frac{rk_{rs}a_3}{2}\psi(x; 2, 1, 2) \\ + \left(rk_{rs}a_4 - \frac{a_3 k_s}{2} \right)\psi(x; 3, 1, 3) - a_4 k_s\psi(x; 4, 1, 4) + k_s = 0\end{aligned}\quad (\text{E.13})$$

Equation (E.13) permits numerical computation of x given values for k_s and k_{rs} . This computed value for x can be inserted into (E.12) to provide the particular value of k_r at which the data need to be estimated (through interpolation).

¹¹ For use in a Newton numerical, iterative, root-finding procedure

Annex F MIMO configuration

This section demonstrates how subarrays of a uniform phased array antenna can be combined to yield signals of the form of (49). In the configuration described below, Transmit/Receive T/R modules form the basic element of the phased array.

As illustrated in Figure F.1, assume that every transmission, from every element, is received

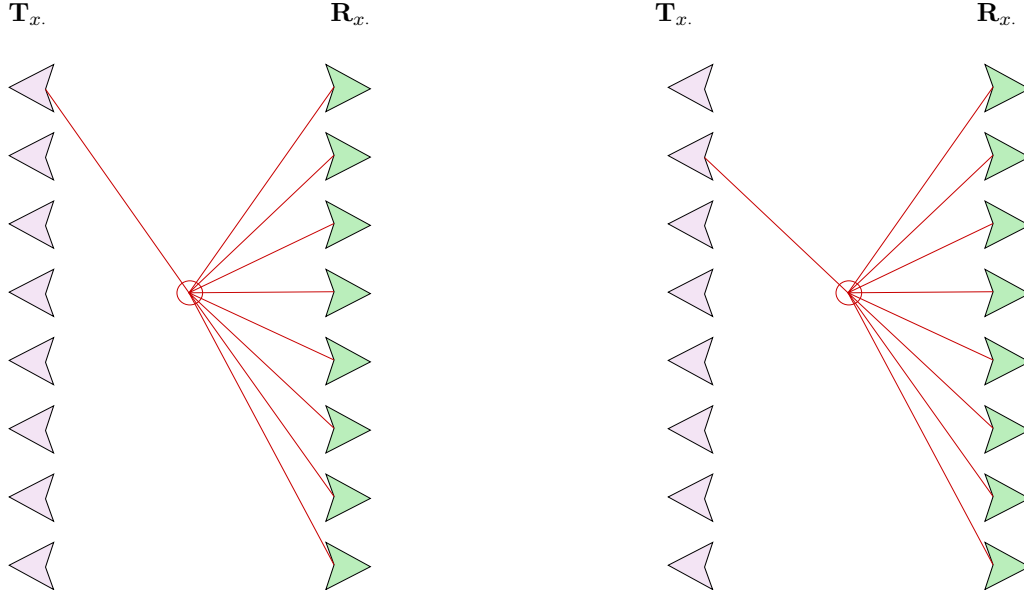


Figure F.1: Configuration of transmit and receive. Each transmitted signal is received by all receivers

and summed independently (i.e. assume superposition applies). Assume further that signals are transmitted at time τ , but with different delays on transmission (programmed delays) for each T/R module and that the echoes of these signals are received at time $\tau + 2r(s)/c$, but with different Rx delays for each T/R module (programmed delays)

Now, the time delay to irradiate a target depends on the position of the transmitter and the location of the target. In the model, we denote the target position as s_x and the position of each transmitter and receiver as $\mathbf{T}_{x_{n'}}$, $n' \in \{0, N' - 1\}$ and $\mathbf{R}_{x_{m'}}$, $m' \in \{0, M' - 1\}$, respectively. We also denote the transmitted waveform as

$$z(\tau) = p(\tau)e^{i\omega_0\tau}, \quad (\text{F.1})$$

where $p(\tau)$ is some baseband waveform. With this notation, and with transmit and receive delays given by $\delta_{T_{n'}}$ and $\delta_{R_{m'}}$, respectively, the far field delay for a transmit/receive pair is given by

$$\delta_{m'n'}(s) = \frac{2r(s, \mathbf{x})}{c} + \delta_{T_{n'}} + \delta_{R_{m'}} + \frac{\mathbf{T}_{x_{n'}} \cdot \hat{\mathbf{r}}(s, \mathbf{x})}{c} + \frac{\mathbf{R}_{x_{m'}} \cdot \hat{\mathbf{r}}(s, \mathbf{x})}{c} \quad (\text{F.2})$$

and the return signal is given by

$$z_{mn}(\tau, s) = A_{T_{n'}} A_{R_{m'}} z[\tau - \delta_{m'n'}(s)], \quad (\text{F.3})$$

where $A_{T_{n'}}$ and $A_{R_{m'}}$ denote the antenna gains for transmit and receive from channels n', m' , respectively. Through the principle of superposition, the system measured signal is given by

$$\begin{aligned} z_s(\tau, s) &= \sum_{m', n'} z_{m'n'}(\tau, s) \\ &= \sum_{m', n'} A_{T_{n'}} A_{R_{m'}} z[\tau - \delta_{m'n'}(s)]. \end{aligned} \quad (\text{F.4})$$

In the fast-time frequency domain, this signal can be written as

$$\begin{aligned} Z_s(\omega', s) &= \sum_{m', n'} A_{T_{n'}} A_{R_{m'}} Z(\omega') e^{-i\omega' \delta_{m'n'}(s)} \\ &= Z(\omega') e^{-i\omega' \frac{2r(s, \mathbf{x})}{c}} \sum_{n'} A_{T_{n'}} e^{-i\omega' [\delta_{T_{n'}} + \frac{\mathbf{T}_{x_{n'}} \cdot \hat{\mathbf{r}}(s, \mathbf{x})}{c}]} \\ &\quad \cdot \sum_{m'} A_{R_{m'}} e^{-i\omega' [\delta_{R_{m'}} + \frac{\mathbf{R}_{x_{m'}} \cdot \hat{\mathbf{r}}(s, \mathbf{x})}{c}]}, \end{aligned} \quad (\text{F.5})$$

where $\omega' = \omega + \omega_0$.

Suppose that $\mathbf{T}_{x_{n'}} = n' \mathbf{b}$ and that $\mathbf{R}_{x_{m'}} = m' \mathbf{b}$, i.e. a uniformly spaced array, and that the timing delays are chosen such that $\delta_{T_{n'}} = -n' \mathbf{b} \cdot \mathbf{u}_n / c$ and $\delta_{R_{m'}} = -m' \mathbf{b} \cdot \mathbf{u}_n / c$ for some given look vector \mathbf{u}_n . In this case, the signal becomes

$$\begin{aligned} Z_s(\omega', s) &= Z(\omega') e^{-i\omega' \frac{2r(s, \mathbf{x})}{c}} \sum_{n'} A_{T_{n'}} e^{-i\omega' \frac{n'}{c} \mathbf{b} \cdot [-\mathbf{u}_n + \hat{\mathbf{r}}(s, \mathbf{x})]} \\ &\quad \cdot \sum_{m'} A_{R_{m'}} e^{-i\omega' \frac{m'}{c} \mathbf{b} \cdot [-\mathbf{u}_n + \hat{\mathbf{r}}(s, \mathbf{x})]} \end{aligned} \quad (\text{F.6})$$

Further, suppose that the weights, $A_{T_{n'}}$ and $A_{R_{m'}}$, are such that $\exists n'_n, m'_n$ with the properties that both

$$\sum_{n'} A_{T_{n'}} e^{-i\omega' \frac{n' - n'_n}{c} \mathbf{b} \cdot [-\mathbf{u}_n + \hat{\mathbf{r}}(s, \mathbf{x})]} \quad (\text{F.7})$$

and

$$\sum_{m'} A_{R_{m'}} e^{-i\omega' \frac{m' - m'_n}{c} \mathbf{b} \cdot [-\mathbf{u}_n + \hat{\mathbf{r}}(s, \mathbf{x})]} \quad (\text{F.8})$$

are real $\forall \omega'$. As a particular example, if $A_{T_{n'}} = A_{T_x}$, a constant, for $n' \in \{n'_0, n'_0 + 1, n'_0 + 2, \dots, n'_0 + N' - 1\}$, then $n'_n = n'_0 + N'/2$. With this condition,

$$\begin{aligned} Z_s(\omega', s) &= Z(\omega') e^{-i\omega' \frac{2r(s, \mathbf{x})}{c}} e^{-i\omega' \frac{n'_n}{c} \mathbf{b} \cdot [-\mathbf{u}_n + \hat{\mathbf{r}}(s, \mathbf{x})]} e^{-i\omega' \frac{m'_n}{c} \mathbf{b} \cdot [-\mathbf{u}_n + \hat{\mathbf{r}}(s, \mathbf{x})]} \\ &\quad \sum_{n'} A_{T_{n'}} e^{-i\omega' \frac{n' - n'_n}{c} \mathbf{b} \cdot [-\mathbf{u}_n + \hat{\mathbf{r}}(s, \mathbf{x})]} \sum_{m'} A_{R_{m'}} e^{-i\omega' \frac{m' - m'_n}{c} \mathbf{b} \cdot [-\mathbf{u}_n + \hat{\mathbf{r}}(s, \mathbf{x})]} \end{aligned} \quad (\text{F.9})$$

With $\omega'/c = k_r/2$, let

$$\mathbf{p}_n(s) = \frac{n'_n \mathbf{b} + m'_n \mathbf{b}}{2}, \quad (\text{F.10})$$

and define

$$\begin{aligned} D_n[k_r, \hat{\mathbf{r}}(s, \mathbf{x})] &= \sum_{n'} A_{T_{n'}} e^{-ik_r \frac{n' - n'_n}{2} \mathbf{b} \cdot [-\mathbf{u}_n + \hat{\mathbf{r}}(s, \mathbf{x})]} \\ &\quad \sum_{m'} A_{R_{m'}} e^{-ik_r \frac{m' - m'_n}{2} \mathbf{b} \cdot [-\mathbf{u}_n + \hat{\mathbf{r}}(s, \mathbf{x})]}. \end{aligned} \quad (\text{F.11})$$

Then,

$$Z_s(k_r, s) = Z(k_r) e^{-ik_r r(s, \mathbf{x})} e^{-ik_r \mathbf{p}_n(s) \cdot \hat{\mathbf{r}}(s, \mathbf{x})} e^{ik_r \mathbf{p}_n(s) \cdot \mathbf{u}_n} D_n[k_r, \hat{\mathbf{r}}(s, \mathbf{x})] \quad (\text{F.12})$$

Finally, compute $e^{-ik_r \mathbf{p}_n(s) \cdot \mathbf{u}_n} Z_s(k_r, s)$ to obtain the expression in (57).

Annex G Antenna pattern angles

Let us examine $\hat{\mathbf{r}}(s, \mathbf{x}) \cdot \mathbf{N}(s)$ and $\hat{\mathbf{r}}(s, \mathbf{x}) \cdot \mathbf{B}(s)$ by expanding these terms around s_0, \mathbf{x}_0 . A first order expansion of the look vector yields

$$\hat{\mathbf{r}}(s, \mathbf{x}) \approx \hat{\mathbf{r}}_0 + (s - s_0) \frac{\mathbf{P}_{\mathbf{r}_0} \mathbf{T}_0}{r_0} + \frac{\mathbf{P}_{\mathbf{r}_0}(\mathbf{x} - \mathbf{x}_0)}{r_0}, \quad (\text{G.1})$$

where $\mathbf{r}_0 = \mathbf{r}(s_0, \mathbf{x}_0)$.

Since \mathbf{T}_0 is perpendicular to \mathbf{r}_0 , one immediately finds that $\mathbf{P}_{\mathbf{r}_0} \mathbf{T}_0 = \mathbf{T}_0$. Furthermore

$$\mathbf{x}_0 = \mathbf{c}(s_0) + r_0 \cos \phi_0 \mathbf{N}_0 + r_0 \sin \phi_0 \mathbf{B}_0, \quad (\text{G.2})$$

and

$$\begin{aligned} \mathbf{x} &= \mathbf{c}(s_0) + (s_{\mathbf{x}} - s_0) \mathbf{T}_0 + \frac{(s_{\mathbf{x}} - s_0)^2}{2} \kappa_0 \mathbf{N}_0 + \frac{(s_{\mathbf{x}} - s_0)^3}{6} [-\kappa_0^2 \mathbf{T}_0 + \kappa'_0 \mathbf{N}_0 + \kappa_0 \tau_0 \mathbf{B}_0] \\ &\quad + r \cos \phi \left[\mathbf{N}_0 + (s_{\mathbf{x}} - s_0) (-\kappa_0 \mathbf{T}_0 + \tau_0 \mathbf{B}_0) \right] + r \sin \phi \left[\mathbf{B}_0 + (s_{\mathbf{x}} - s_0) (-\tau_0 \mathbf{N}_0) \right] \end{aligned} \quad (\text{G.3})$$

In the above, we have used the Frenet-Serret equations of (19) to make the approximation that

$$\mathbf{N}(s) \approx \mathbf{N}_0 + (s - s_0) \left[-\kappa_0 \mathbf{T}_0 + \tau_0 \mathbf{B}_0 \right] \quad (\text{G.4})$$

$$\mathbf{B}(s) \approx \mathbf{B}_0 + (s - s_0) \left[-\tau_0 \mathbf{N}_0 \right] \quad (\text{G.5})$$

Now with

$$\hat{\mathbf{r}}_0 = \cos \phi_0 \mathbf{N}_0 + \sin \phi_0 \mathbf{B}_0 \quad (\text{G.6})$$

one can calculate that

$$\hat{\mathbf{r}}_{0\perp} = \sin \phi_0 \mathbf{N}_0 - \cos \phi_0 \mathbf{B}_0. \quad (\text{G.7})$$

By combining equations (G.2), (G.3) and (G.7), one arrives at the following expressions

$$\mathbf{P}_{\mathbf{r}_0}(\mathbf{x} - \mathbf{x}_0) = [\hat{\mathbf{r}}_{0\perp} \cdot (\mathbf{x} - \mathbf{x}_0)] \hat{\mathbf{r}}_{0\perp} \quad (\text{G.8})$$

and

$$\begin{aligned} \hat{\mathbf{r}}_{0\perp} \cdot (\mathbf{x} - \mathbf{x}_0) &\approx \frac{1}{6} (s_{\mathbf{x}} - s_0)^3 [\kappa_0 \tau_0 \cos \phi_0 - \kappa'_0 \sin \phi_0] + \frac{1}{2} \kappa (s_{\mathbf{x}} - s_0)^2 \sin \phi_0 \\ &\quad - (s_{\mathbf{x}} - s_0) r \tau_0 \cos(\phi - \phi_0) - r \sin(\phi - \phi_0) \end{aligned} \quad (\text{G.9})$$

The only term that makes a difference in the above is $r \sin(\phi - \phi_0)$, thus

$$\frac{\mathbf{P}_{\mathbf{r}_0}(\mathbf{x} - \mathbf{x}_0)}{r_0} \approx -\frac{r}{r_0} \sin(\phi - \phi_0) \hat{\mathbf{r}}_{0\perp} \quad (\text{G.10})$$

Thus, one finally arrives at

$$\begin{aligned}
\hat{\mathbf{r}}(s, \mathbf{x}) &\approx \hat{\mathbf{r}}_0 + (s - s_0) \frac{\mathbf{T}_0}{r_0} + \frac{r}{r_0} \sin(\phi - \phi_0) \hat{\mathbf{r}}_{0\perp} \\
&= \cos \phi_0 \mathbf{N}_0 + \sin \phi_0 \mathbf{B}_0 + (s - s_0) \frac{\mathbf{T}_0}{r_0} \\
&\quad + \frac{r}{r_0} \sin(\phi - \phi_0) [\sin \phi_0 \mathbf{N}_0 - \cos \phi_0 \mathbf{B}_0] \\
&= [\cos \phi_0 + \frac{r}{r_0} \sin \phi_0 \sin(\phi - \phi_0)] \mathbf{N}_0 \\
&\quad + [\sin \phi_0 - \frac{r}{r_0} \cos \phi_0 \sin(\phi - \phi_0)] \mathbf{B}_0 \\
&\quad + (s - s_0) \frac{\mathbf{T}_0}{r_0}
\end{aligned} \tag{G.11}$$

Note that in the neighbourhood of \mathbf{x}_0 , $\sin(\phi - \phi_0) \approx \phi - \phi_0$ and $\frac{r}{r_0} \approx 1$ one arrives at the approximation that

$$\hat{\mathbf{r}}(s, \mathbf{x}) \approx \cos \phi \mathbf{N}_0 + \sin \phi \mathbf{B}_0 + (s - s_0) \frac{\mathbf{T}_0}{r_0} \tag{G.12}$$

Substitution of the approximations for $\mathbf{N}(s)$ and $\mathbf{B}(s)$ yields

$$\begin{aligned}
\hat{\mathbf{r}}(s, \mathbf{x}) \cdot \mathbf{N}(s) &\approx \cos \phi_0 + \frac{r}{r_0} \sin \phi_0 \sin(\phi - \phi_0) \\
&\quad + \tau_0 (s - s_0) [\sin \phi_0 - \frac{r}{r_0} \cos \phi_0 \sin(\phi - \phi_0)] \\
&\quad - \kappa_0 \frac{(s - s_0)^2}{r_0}
\end{aligned} \tag{G.13}$$

and

$$\begin{aligned}
\hat{\mathbf{r}}(s, \mathbf{x}) \cdot \mathbf{B}(s) &\approx \sin \phi_0 - \frac{r}{r_0} \cos \phi_0 \sin(\phi - \phi_0) \\
&\quad - \tau_0 (s - s_0) [\cos \phi_0 + \frac{r}{r_0} \sin \phi_0 \sin(\phi - \phi_0)]
\end{aligned} \tag{G.14}$$

In summary, and with only the non-negligible terms retained (for the Sentinel-1 orbit examined in this document, κ_0 and τ_0 take on values of approximately 10^{-7} , 10^{-8} , respectively which means that they can be considered negligible over a scene of several hundred kilometers in s), one finds that

$$\hat{\mathbf{r}}(s_p) \cdot \mathbf{T}(s_p) = -k_s/k_r \tag{G.15}$$

$$\hat{\mathbf{r}}(s_p) \cdot \mathbf{N}(s_p) = \cos \phi_0 + \frac{r}{r_0} \sin \phi_0 \sin(\phi - \phi_0) \tag{G.16}$$

$$\hat{\mathbf{r}}(s_p) \cdot \mathbf{B}(s_p) = \sin \phi_0 - \frac{r}{r_0} \cos \phi_0 \sin(\phi - \phi_0), \tag{G.17}$$

which leads the following

$$\begin{aligned} & \alpha_{\parallel n} k_r \hat{\mathbf{r}}(s_p) \cdot \mathbf{T}(s_p) + k_r \boldsymbol{\alpha}_{\perp n} \cdot [\hat{\mathbf{r}}(s_p) \cdot \mathbf{N}(s_p), \hat{\mathbf{r}}(s_p) \cdot \mathbf{B}(s_p)] \\ &= -\alpha_{\parallel n} k_s + k_r \boldsymbol{\alpha}_{\perp n} \cdot \hat{\mathbf{r}}_0 + k_r r \frac{\boldsymbol{\alpha}_{\perp n} \cdot \hat{\mathbf{r}}_{0\perp}}{r_0} \sin(\phi - \phi_0) \end{aligned} \quad (\text{G.18})$$

Note that in the neighbourhood of r_0, ϕ_0 , (G.16) and (G.17) closely approximate the first order expansion of the cosine and sine functions; thus, in this neighbourhood, one may write

$$\hat{\mathbf{r}}(s_p) \cdot \mathbf{T}(s_p) = -k_s/k_r \quad (\text{G.19})$$

$$\hat{\mathbf{r}}(s_p) \cdot \mathbf{N}(s_p) = \cos \phi \quad (\text{G.20})$$

$$\hat{\mathbf{r}}(s_p) \cdot \mathbf{B}(s_p) = \sin \phi \quad (\text{G.21})$$

In summary, (G.15), (G.16), (G.17), (G.20), (G.21) and (63) lead to the following expression for the signal in k -space

$$\begin{aligned} \mathcal{S}S_n(k_r, k_s) &= \mathcal{P}(k_{r'}) e^{i\alpha_{\parallel n} k_s - ik_r \boldsymbol{\alpha}_{\perp n} \cdot \hat{\mathbf{r}}_0} \\ &\int \frac{g(\mathbf{x}) e^{-ik_r r \frac{\boldsymbol{\alpha}_{\perp n} \cdot \hat{\mathbf{r}}_{0\perp}}{r_0} \sin(\phi - \phi_0)} D_n[k_r, -k_s/k_r, \cos \phi, \sin \phi]}{r^2(s_p[k_r, k_s])} e^{-ik_r r (s_p[k_r, k_s])} d\mathbf{x}. \end{aligned} \quad (\text{G.22})$$

DOCUMENT CONTROL DATA

*Security markings for the title, authors, abstract and keywords must be entered when the document is sensitive

<p>1. ORIGINATOR (Name and address of the organization preparing the document. A DRDC Centre sponsoring a contractor's report, or a tasking agency, is entered in Section 8.)</p> <p>DRDC – Ottawa Research Centre 3701 Carling Avenue, Ottawa ON K1A 0Z4, Canada</p>		
<p>2a. SECURITY MARKING (Overall security marking of the document, including supplemental markings if applicable.)</p> <p>CAN UNCLASSIFIED</p>		
<p>2b. CONTROLLED GOODS NON-CONTROLLED GOODS DMC A</p>		
<p>3. TITLE (The document title and sub-title as indicated on the title page.)</p> <p>Super Resolution Synthetic Aperture Radar: Design and Signal Processing of a Multi-Beam Multi-Channel Stripmap Mode</p>		
<p>4. AUTHORS (Last name, followed by initials – ranks, titles, etc. not to be used. Use semi-colon as delimiter)</p> <p>Sikaneta, I. C.; Gierull, C. H.</p>		
<p>5. DATE OF PUBLICATION (Month and year of publication of document.)</p> <p>March 2022</p>	<p>6a. NO. OF PAGES (Total pages, including Annexes, excluding DCD, covering and verso pages.)</p> <p>86</p>	<p>6b. NO. OF REFS (Total cited in document.)</p> <p>42</p>
<p>7. DOCUMENT CATEGORY (e.g., Scientific Report, Contract Report, Scientific Letter)</p> <p>Scientific Report</p>		
<p>8. SPONSORING CENTRE (The name and address of the department project or laboratory sponsoring the research and development.)</p> <p>DRDC – Ottawa Research Centre 3701 Carling Avenue, Ottawa ON K1A 0Z4, Canada</p>		
<p>9a. PROJECT OR GRANT NO. (If appropriate, the applicable research and development project or grant number under which the document was written. Please specify whether project or grant.)</p> <p>42zz78</p>	<p>9b. CONTRACT NO. (If appropriate, the applicable contract number under which the document was written.)</p>	
<p>10a. DRDC DOCUMENT NUMBER</p> <p>DRDC-RDDC-2022-R—Will be inserted by Publication Officer</p>	<p>10b. OTHER DOCUMENT NO(s). (Any other numbers which may be assigned this document either by the originator or by the sponsor.)</p>	
<p>11a. FUTURE DISTRIBUTION WITHIN CANADA (Approval for further dissemination of the document. Security classification must also be considered.)</p> <p>Defence departments and their contractors</p>		
<p>11b. FUTURE DISTRIBUTION OUTSIDE CANADA (Approval for further dissemination of the document. Security classification must also be considered.)</p> <p>None</p>		

12. KEYWORDS, DESCRIPTORS or IDENTIFIERS (Use semi-colon as a delimiter.)

SAR; HRWS; Multi-channel; Orbit; Differential geometry; Multi-beam; Spherical harmonics; High-resolution; Phased-array; True time-delay; Spotlight

13. ABSTRACT/RÉSUMÉ (When available in the document, the French version of the abstract must be included here.)

By presenting the design, configuration and required end-to-end signal processing, this report proposes a system for improved SAR imaging. Compared to conventional Spotlight SAR, the proposed system will generate imagery with equivalent or better resolution and significantly increased area coverage. The design and configuration are based upon a phased-array antenna in combination with the appropriate hardware to enable rapid electronic beam steering and to permit digitisation of multiple receive channels. The current state of technology is mature enough to construct all components of such a system. As a specific goal, the report proposes a system capable of imaging with 10 cm resolution (azimuth and slant-range) over a ground swath of 5 km. The proposed system is simulated at X-band, but could, in principle, be operated at any band with sufficiently available bandwidth. Importantly, this mode can collect with unlimited azimuth extent, something that no other proposed system can achieve.

As the considered resolutions push the limits of known theory, the report also introduces an augmented theory that is needed to derive the signal processing algorithms. The presented approach incorporates a physical model, based upon the spherical harmonic model of the Earth's gravitational potential, into the theory of differential geometry of curves in three dimensions. From the theory, a wavenumber-based SAR processing algorithm that extends current methods is developed and presented. The proposed algorithm relies only on accurate attitude data and a single accurate state vector. The approach is therefore suitable for on-board SAR processing if sensor instruments can measure these parameters while imaging.

Ceci est le résumé en français.